Increasing the optical transparency of a living mouse brain
(And other nanotechnologies)

by

Ishan Gupta

B.Tech. Biotechnology
Indian Institute of Technology Guwahati, 2011

Submitted to the Department of Biological Engineering
in partial fulfillment of the requirements for the degree of

Doctor of Philosophy in Biological Engineering

at the
MASSACHUSETTS INSTITUTE OF TECHNOLOGY
August 2019

Signature of Author .. Signature redacted ....
Department of Biological Engineering
August 8th 2019

Signature redacted

Certified By ....
Prof. Edward S. Boyden
Professor of Biological Engineering, Brain and Cognitive Sciences, Media Arts and Sciences
Thesis Supervisor

Signature redacted

Accepted By ....
Prof. Paul Blainey
Associate Professor of Biological Engineering
Co-Chair of Graduate Program, Department of Biological Engineering

Thesis Committee Members

Prof. Darrell J. Irvine

Professor of Materials Science & Engineering, and Biological Engineering

Thesis Committee Chair

Prof. Edward S. Boyden

Professor of Biological engineering, Brain and Cognitive Sciences, Media arts and Sciences

Thesis Supervisor

Prof. Paul Blainey

Associate Professor of Biological Engineering

Committee member

Abstract

Many methods for increasing the optical transparency of non-living brain tissue have come into widespread use because of their utility in enabling better anatomical brain imaging. In the first part of this thesis, we explore whether this is also possible for living brain tissue. We report a general principle for doing so, namely the reduction of refractive index mismatch between cellular membranes and the extracellular space, using high refractive index biocompatible reagents that have high molecular weights, so that they can be used at low concentrations. We implement this via multiple reagents that satisfied these criteria, including the iodinated radiocontrast agent iodixanol, high molecular weight polyethylene glycol (PEG), high molecular weight Dextran, and PEG-ylated Silicon nanoparticles. We achieve ~2x increases in the brightness of cells expressing red fluorescent proteins in vivo in mice, as measured by conventional one-photon epifluorescence imaging, using concentrations of reagents that increased the refractive index of the extracellular space by just 0.01. Lastly, We show that Dextran does not have a statistically significant effect on neural physiology or neural network properties. We expect such strategies to not only facilitate live imaging of the brains of mice and other mammals, but open up a new class of strategies for changing the electromagnetic properties of living systems.

We conclude this thesis with two nanotechnologies that may be leveraged for making higher performance reagents for increasing the optical transparency of living brain tissue. (1) A method for the synthesis of high-yield and high-monodispersity nanoparticles of a variety of materials with tailored surface ligands, using common benchtop equipment. This method may be useful for developing nanoparticles with better biosafety, efficacy and performance. (2) A method for the delivery of hydrophobic NVNDs to neural cell membranes using PEG-ylated liposomes. These PEG-ylated liposomes may be used for delivery of hydrophyllic nanoparticles to neural soma and achieve maximal transparency.

Acknowledgements

Many people helped make this thesis possible.

I am extremely grateful to my thesis advisor - Prof. Ed Boyden, for providing mentorship, guidance, infrastructure and support to pursue this ambitious and (hopefully) important work. I also thank my thesis committee - Prof. Darrell Irvine and Prof. Paul Blainey, for their careful criticism and kind encouragement all these years.

I reserve special thanks for Giovanni Talei Franzesi, Daniel Martin-Alarcon, Kiryl Piatkevich, Ruixuan Gao, and Or Shemesh who contributed to the planning, development and execution of key themes and experiments in this thesis. I also had the pleasure of great collaborations with the Kortshagen Group at University of Minnesota, Veinot Group at University of Alberta, and So lab at MIT.

I also wish to thank David Rolnick, Zachary Barry, Nick Barry, Yongjin Park, Anya Roberts, Marianna Sofman, Nikita Obidin, Amar Ghodasara, Amelia Perry, Andrew Payne, Danielle Cosio, Charlotte Lowey, Alexandre Bisson Filho, Ana Teixeira, Lucianne Schons, Rawan Nazer, Gia Medhi, Akanksha Raina, Rinal Chheda and Prasun Bhowmik for their ongoing friendship and unwavering support.

To my parents, Sanjay and Satyabhama, and to my lil sister, Tanvi. I wish to express my deepest love, respect and gratitude for all the unconditional love and support all of these years. To my partner Ola, thank you for riding the highs and lows of graduate school with me and for always being there.

Finally, I would like to acknowledge my funding sources that made this work possible: McGovern Institute of Brain Research - MIT, National institute of health (NIH) and National Science Foundation (NSF).

Table of Contents

Chapter 1: Principles for optical clearing live brain tissue

Driven by the overarching goal of understanding how neural codes emerge from the interactions of neural circuit components, much current effort is focused on developing new fluorescent probes for high-speed physiological events such as action potentials [1-5] and synaptic transmission [6-8] in the brain. Neurons that interact in circuits can be located over extended volumes, e.g. cortical microcircuits [9-12] occupying a cubic millimeter or more of brain tissue. However, imaging at high speeds sufficient to keep up with neural activity in 3-D has not been possible over such depths. This is due to the scattering of light in brain tissue [13-17]. Traditional one-photon methods of imaging are limited to depths of perhaps just a few tens of microns, limiting the volume that can be interrogated; two-photon imaging can achieve greater depth (i.e., many hundreds of microns), at the expense of slower imaging rates due to the scanning and directed nature of multiphoton excitation [18-20], which in turn limits the overall volumes of neural circuitry accessible. Accessing a deep neural circuit of interest through endoscopic targeting [21], or surgical removal of overlying tissue [22], is possible, but again does not increase the overall volumes accessible. In recent years, much attention has been focused on advanced hardware capable of adaptive optics [23-32], which attempt to invert the light scattering process through physical or computational means, but such tools require extensive recalibration when the scattering matrix changes – as occurs over millisecond timescales during normal physiological function [33-35]– and which has to date limited deployment in biological settings.

Here, we propose to tackle the problem from the opposite direction – making the living brain, itself, more transparent. The key issue is scattering of light in brain tissue. Scattering of light in cells is due to the refractive index (RI) mismatch between organelles and free cytosol, and lipid membranes and extracellular space, which cause Mie scattering [16,17]. Lipid components of cells and tissues have higher RI than aqueous components, causing light to be scattered at such interfaces. Therefore to make the tissue itself less scattering, the RI mismatch between the tissue components, i.e. between cytosol, organelles, cell membranes, and extracellular space, needs to be reduced.

Index-matching the aqueous and lipid fractions to each other, or removing lipids entirely, has been shown by multiple groups to make tissues transparent, in fixed tissues [36-40]. These studies provide powerful evidence that balancing the RI across the aqueous and lipid components is key. This then raises the question: how best to balance the RI across aqueous and lipid components? Removing lipids is not an option in the living state, obviously, even if it is popular in preserved tissues. Accordingly, the remaining option is to index-match the aqueous and lipid fractions, either by raising the RI of aqueous components (by introducing a high RI chemical into the cytosol), or lowering the RI of lipids (by introducing a low RI chemical into the lipids). We first evaluate these possibilities through physical modelling.

Evaluation of RI-matching strategies using Mie theory and Effective medium approximations:

To first order, the effective permittivity of a mixture is the volume-weighted average of the permittivities of the constituents [41]. Given that lipid membranes have index of refraction

$n_{lipid} \sim 1.46$, and cytosol and extracellular space have lower RI, $n_{cyto} \sim 1.35$, we can evaluate the feasibility of incorporating into the lipid fraction a lower RI material. Consider the extreme case: we insert transparent vacuum-filled bubbles (n_{bubb}=1.0) in all lipid membranes. The volume fraction ϕ of such bubbles in the lipid fraction would then be calculated from equations (1) and (2).

$$\phi n_{bubb}^2 + (1-\phi)n_{lipid}^2 \approx \phi + (1-\phi)n_{lipid}^2 \approx n_{cyto}^2 \tag{1}$$

$$\phi \approx \frac{n_{lipid}^2 - n_{cyto}^2}{n_{lipid}^2 - 1.0} = 0.27 \tag{2}$$

This means that 30% of all membrane volume would be filled with such vacuum bubbles for index matching – which is likely to be impractical. Not to mention, that any addition to neural membranes is likely to affect neural function and communication significantly. Accordingly, we focus our attention on molecules that can raise the RI of the cytosol and extracellular space.

We can use a similar derivation to characterize the required properties of the alternative strategy, i.e. increasing the RI of the aqueous compartments, cytosol and extracellular space, and show it is a conceptually viable approach. For simplicity, let us assume that the extinction coefficients of the aqueous fraction and the lipids are effectively zero (κ_{cyto}, $\kappa_{lipid} \approx 0$) but the chemical reagent extinction coefficient $\kappa_{reagent}$ is nonzero at the relevant wavelength λ. Mie theory describes the scattering properties of a simple suspension of scattering spheres as (3) [42-44],

$$\frac{1}{L_s} \propto \frac{\pi r^2 \rho_s}{(1-g)}\left(\frac{2\pi r}{\lambda}\right)^a \left(\frac{n_p}{n_m} - 1\right)^b \tag{3}$$

where L_s is the characteristic length scale for scattering or scattering length, g is the anisotropy of scattering, r is the radius of scattering spheres, ρ_s the volume density of the scattering spheres, "λ" the wavelength of the incident light, n_p is RI of the scattering spheres, n_m is the RI of the surrounding medium, and a and b are empirically determined coefficients. For tissue, since most of the scattering is caused by lipid bound intracellular organelles, this expression may be reduced to (4) [42-44],

$$L_{so} \propto \left(\frac{n_{lipid}}{n_{cyto}} - 1\right)^{-2.09} \tag{4}$$

where L_{so} is the baseline scattering length, n_{lipid} is the RI of lipid, and n_{cyto} is the RI of the aqueous fraction. We know that $n_{lipid} \approx 1.46$ and $n_{cyto} \approx 1.35$ [42,43] for most biological tissue. By the introduction of particles with RI $n_{reagent}$ with a fill fraction ϕ in the aqueous fraction, the new scattering length L_s^{eff} can be estimated from equations (5) and (6),

$$\phi n_{reagent}^2 + (1-\phi)n_{cyto}^2 \approx n_{eff}^2 \tag{5}$$

$$\frac{L_s^{eff}}{L_{s0}} = \left(\frac{\frac{n_{lipid}}{n_{cyto}} - 1}{\frac{n_{lipid}}{n_{eff}} - 1}\right)^{2.09} \tag{6}$$

where n_{eff} is the net RI of the aqueous fraction with nanoparticles, taken as a representative live tissue optical clearing agent. At this point, it is useful to note that for most microscopy the optical access (or imaging depth) in tissue depends directly on the scattering length [42]. This is a consequence of the dependence of fraction of light that remains non-scattered I/I_o with distance travelled by light d through a media with scattering length L_s (7).

$$\frac{I}{I_o} = e^{-\frac{d}{L_s}} \tag{7}$$

Using the formalisms above it is thus possible to estimate the effect of addition of various materials at various fill fractions on the scattering properties of tissue. Then, so as to eliminate scattering through index matching, we want to choose the volume fraction ϕ of the aqueous fraction that is made of chemical reagent, such that, to first order (8), or (9).

$$\phi n_{reagent}^2 + (1-\phi) n_{cyto}^2 \approx n_{lipid}^2 \tag{8}$$

$$\phi \approx \frac{n_{lipid}^2 - n_{cyto}^2}{n_{part}^2 - n_{cyto}^2} \tag{9}$$

More precisely, we can use the Hashin-Shtrikman lower bound on the permittivity of a binary dielectric mixture to determine the maximum necessary nanoparticle volume fraction (10) [45], and hence (11).

$$n_{lipid}^2 \geq n_{cyto}^2 + \frac{\phi}{\frac{1}{n_{reagent}^2 - n_{cyto}^2} + \frac{1-\phi}{3n_{cyto}^2}} \tag{10}$$

$$\phi_{HSmax} = \frac{\frac{1}{n_{reagent}^2 - n_{cyto}^2} + \frac{1}{3n_{cyto}^2}}{\frac{1}{n_{lipid}^2 - n_{cyto}^2} + \frac{1}{3n_{cyto}^2}} \tag{11}$$

To avoid making the final tissue opaque via absorption increasing, we must calculate the particle-aqueous fraction composite material extinction coefficient, as (12). The extinction depth is then given by (13).

$$\kappa_{meta} \approx \phi \kappa_{reagent} \frac{n_{part}}{n_{lipid}} \tag{12}$$

$$L = \frac{\lambda}{4\pi \kappa_{meta}} \tag{13}$$

Are there any materials that would be suitable? As shown in Fig. 1, a variety of small molecules, polymers and inorganic nanoparticles could potentially increase scattering length (and, hence, imaging depth) at realistic volume fill levels ~1-10%.

As expected, Inorganic materials offer the highest degree of index matching for a given volume percent (e.g. at only 1% volume fraction, Ge nanoparticles afford perfect index matching). We find that for many materials, e.g. diamond ($n = 2.43$) or diamondoids (like adamantane), silicon carbide ($n = 2.67$), zirconium dioxide ($n = 2.225$), volume fractions of $\phi < 10\%$ would yield perfect index matching, with no net absorption ($L \sim \infty$). Other materials, like titanium dioxide ($n = 2.59$) will absorb in the green, but not in the red ($L \sim \infty$), and can be useful as well. Further, for semiconductors such as Silicon ($n = 3.9$), Germanium ($n = 5.67$) and Cadmium Telluride ($n=3.12$) (Fig. 1b), quantum confinement at particle size less than excitonic Bohr radius leads to reduced absorption while retaining high refractive indices [46-48]. Finally, small molecules like iodixanol ($n = 1.66$), and polymers such as polyethylene glycol ($n = 1.66$), and even some reagents commonly used in biology and medicine, like for example DMSO (n = 1.479) might also meaningfully reduce RI homogeneities and alleviate light scattering.

Effect of increasing RI of all aqueous components on light scattering in brain tissue

Next, we tested the effectiveness of small changes in RI mismatch on light scattering in brain tissue. For this, we used reagents that are known to permeate freely through cell membranes (see table 1) and sequester largely in the aqueous components of tissue. Each reagent was deployed at volume fill levels estimated from (5) to lead to $n_{cyto} \sim 1.36$.

We imaged 15μm-diameter fluorescent (crimson, i.e. 645 nm emission) beads through acute mouse somatosensory cortex brain slices (300 μm thick) placed in an imaging chamber filled with artificial cerebrospinal fluid (aCSF). We then removed the slices from the imaging chamber and placed them in an incubation chamber, where they were incubated for an hour in aCSF with the candidate agents added to it. After the incubation was complete we removed the slices from the incubation chamber, washed them once with regular aCSF, and then placed them in the imaging chamber, filled with regular aCSF. We then imaged the beads through the slice again.

We found that of the reagents tested (see table 1), 10% DMSO (n = 1.3458 in water, estimated from (5) to lead to $n_{cyto} = 1.363$ [49]) in artificial cerebrospinal fluid solution, a concentration used in many neuroscience experiments for bulk loading of calcium indicators in vivo [50,51], obtained a significant increase in imaging capabilities (Fig. 2) without affecting the tissue morphology and size. No such effect has been previously reported because DMSO is likely cleared in vivo before imaging begins (half an hour to hours after dye injection).

Unfortunately, DMSO is not a suitable clearing agent, due to its adverse effects on neural function [52]. It ,however, does show the effectiveness of reagents which only slightly alter overall RI of the aqueous compartments.

Table 1. Cell membrane permeable reagents tested for decreasing light scattering *ex vivo*.

Reagent	**Concentration (for n_{cyto}=1.36)**	**Slice Transparency**	**Slice Morphology and Size**
DimethylSulfoxide	10% v/v	✓	✓
Ethylene Glycol	10% v/v	✓	×
Propylene Glycol	10% v/v	×	×
Urea	8% w/v	×	×

Effect of increasing RI of extracellular space on light scattering in brain tissue

We next hypothesized that reducing the RI mismatch between the extracellular space (n ~1.33 for cerebrospinal fluid [53]) and cellular membranes (n ~1.4628) [53,54] only could also reduce light scattering significantly, and help increase the optical transparency of the living brain.

We reasoned that biocompatible, high refractive index, high molecular weight molecules would be good candidates to test this hypothesis. A high molecular weight would mean that the osmolarity would not need to be changed very much for a given amount of refractive index matching, important for preserving normal brain physiology since osmolarity is an important factor for neuronal operation [55,56].

Because of its excellent in vivo safety profile [57], we focused our initial testing on the s radiocontrast agent iodixanol, which is commonly used in humans during coronary angiography. Importantly, Iodixanol has also been used to make immersion media for correcting spherical aberration in cell cultures, planarians, zebrafish, and human cerebral organoids [58].

Employing aCSF augmented with 6% w/v or 40 mM iodixanol (iodixanol-aCSF), with a refractive index of 1.34, approximately ~0.01 higher than regular aCSF (n = 1.33), we achieved an average increase of 124.4% (20th percentile 71.4%, median 127.6%, mean 124.4%, 80th percentile 200.4%, Cohen's d 0.6460, n = 7 slices from 3 mice) in the intensity (above background) of beads seen through the slice compared to before incubation in iodixanol-aCSF (see Fig. 3C for intensity changes after 1hr incubation either in regular aCSF or iodixanol-aCSF). The distributions of intensities for the beads imaged before vs. after adding iodixanol were significantly different ($p = 4.3646*10^{-6}$, two-sample Kolmogorov-Smirnov test, n = 244 beads for the cleared condition, 90 beads for baseline, from 7 slices obtained from 3 mice). To control for the duration over which slices were incubated in vitro, we compared bead intensities following incubation for the same period of time in iodixanol-aCSF vs. regular aCSF, and observed a significant improvement in the imaging for the former case, vs. the latter case (p = 0.0016, two-sample Kolmogorov-Smirnov test, n = 7 slices from 3 mice for iodixanol-aCSF, n = 5 slices from 2 mice for regular aCSF).

While iodixanol is routinely used intravascularly at high concentration (60%) in clinical settings, its effects on neuronal properties, and at lower concentrations (e.g. 6%), have not been described. Given that intact neural physiology is key to insuring the meaningfulness of neural imaging, we performed whole-cell patch clamp assessment of neuronal properties in primary mouse hippocampal neuronal cultures incubated with Tyrode's solution containing 6% iodixanol (iodixanol-Tyrode), corresponding to a refractive index change of 0.01 compared to standard Tyrode's solution (n ~1.33). See Fig. 3D for traces recorded in response to current injection (-100 to 250 pA in 50 pA steps) in a representative control neuron, Fig. 3E for those of a representative cell incubated in iodixanol-Tyrode. We assessed resting membrane potential (Fig. 3F), input resistance (Fig. 3G), membrane capacitance (Fig. 3H), membrane time constant (Fig. 3I), spike threshold (Fig. 3J), and spike width (Fig. 3K), and compared them to those of cells recorded in regular Tyrode's solution. No significant differences were found for any of the parameters analyzed ($p > 0.05$, n = 17 control cells from one culture, n = 16 cells incubated in Iodixanol-Tyrode from the same culture, two-sample Kolmogorov-Smirnov test).

Next, we wanted to test whether treatment with Iodixanol-aCSF would benefit imaging with a neural activity indicator, since we envision most applications of this technology to involve functional imaging of neural activity. An ex vivo preparation allowed us to test this easily, without potential complications due to insufficient delivery of the clearing agent in vivo. Therefore, we used acute brain slices (300 µm) of the mouse primary somatosensory cortex (S1) expressing a genetically encoded far-red voltage indicator Archon1-eGFP [3,5] as a testbed. First, we imaged areas within the slices while superfusing them with regular artificial cerebrospinal fluid (aCSF). We then superfused them for one hour with iodixanol-aCSF, and imaged the same regions again. Finally, we imaged the voltage dynamics of individual neurons, while still superfusing the slices with iodixanol-aCSF.

See Fig. 4A for a representative example of a neuron imaged in the green (475/28 nm excitation, emission 535/22 band pass filter) channel before (left) vs. after (right) superfusion with iodixanol-aCSF, Fig. 4B for the same neuron imaged in the far red (excitation 637 nm, emission 664 long pass filter) channel before vs. after superfusion with iodixanol-aCSF. The images were taken with the same illumination and exposure conditions and without adjusting relative brightness or contrast.

Superfusion with 6% Iodixanol enhanced the signal from both eGFP (20th percentile 14.4%, median 60.3%, mean 83.8%, 80th percentile 131.2%, percent increase in background-subtracted intensity after superfusion with iodixanol-aCSF compared to baseline, on a per-cell basis, $p = 1.2569*10^{-5}$, two-sided Wilcoxon signed rank test, Cohen's $d = 0.5801$, $n = 37$ neurons from 11 sites from 9 slices obtained from 4 mice; Fig. 4C) and Archon (20th percentile 37.3%, median 110.2%, mean 136.6%, 80th percentile 221.7%, background-subtracted intensity after superfusion with iodixanol-aCSF compared to baseline, on a per-cell basis, $p = 1.8650*10^{-7}$, two-sided Wilcoxon signed rank test, Cohen's $d = 1.2445$, $n = 37$ neurons from 11 sites from 9 slices obtained from 4 mice; Fig. 4D).

In many cases superfusion with iodixanol-aCSF revealed eGFP- and Archon-expressing neurons that were previously indistinguishable from background, as detected by eye by an individual blinded to the condition of the image. The neurons were located at variable depths throughout the slices. The increase in the number of neurons that could be discerned was significant for both eGFP (Fig. 4E $p = 0.0156$, two-sided Wilcoxon signed rank test, $n = 11$ sites from 9 slices obtained from 4 mice) and Archon (Fig. 4F; $p = 0.0039$, two-sided Wilcoxon signed rank test, $n = 11$ sites from 9 slices obtained from 4 mice).

We were able to image trains of action potentials from the newly revealed Archon-eGFP expressing neurons by application of 0.1-1 mM 4-Aminopyridine (4-AP) (see Fig. 4G for a representative trace). The application of 4-AP was necessary because neural activity in acute brain slices is negligible otherwise. Note that we imaged neural activity exclusively after incubation, in order to minimize photo-bleaching of Archon and also to avoid excitotoxicity that would be caused by 4-AP administration.

Having demonstrated enhanced transparency in acute live brain slices, we next explored whether this would be possible in the living mouse brain *in vivo*. We chose to employ static labels instead of activity indicators because they allow a simpler and more reliable comparison between baseline and after treatment conditions, free from variation due to changing levels of neural activity. We therefore expressed the far-red fluorescent protein iRFP682 [59], which has a similar spectrum to Archon, but is much brighter, making it possible to image larger areas of tissue rapidly at a lower magnification. Note that conventional one-photon cortical imaging requires sparse expression of fluorescent proteins in order to distinguish individual cells (from the surrounding neuropil), and benefits from having a large enough field of view to provide sufficient numbers of neurons for meaningful analysis.

Mice were prepared to sparsely express iRFP682 either pan-neuronally or selectively in parvalbumin-positive interneurons via AAV delivery in the primary somatosensory cortex (S1). First, we imaged the cortex under normal lactated Ringer's solution. The cortical surface was then superfused with iodixanol-HEPES-aCSF or with an osmotically-matched (40 mM sucrose added to regular aCSF) sucrose-HEPES-aCSF solution for one hour. To compensate for any evaporation, the fluid was replaced every twenty minutes for one hour. At the end of the hour the fluid was replaced with lactated Ringer's solution, and we imaged again at the same location. Representative optical slices taken at progressively greater depths pre- (top) vs. post- (bottom) iodixanol superfusion are shown in Fig. 5A through Fig. 5C, highlighting the increased brightness of cells, and the greater number of cells visible, after iodixanol treatment, particularly deeper into the tissue.

The sparsity of labeled neurons, which as noted above greatly facilitates in vivo one photon imaging, as well as the curvature of the brain, and the difficulty in determining the exact surface of the brain, made an accurate assessment of the imaging depth difficult. Alternative metrics can however be employed to estimate the efficacy of in vivo optical clearing. A simple metric is just the brightness of cells imaged before and after clearing. This is a conservative estimate because it excludes cells that become visible only with optical clearing (as in Fig. 4E, 4F), and includes cells from all depths, including very superficial ones, which are not expected to benefit as much from optical clearing as do deeper cells. We observed a significant increase in background-subtracted intensity after iodixanol treatment (20th percentile 32.8%, median 82.6%, mean 105.7%, 80th percentile 158.2%, $p = 2.5736*10^{-43}$, two-sided Wilcoxon signed rank test, Cohen's d 0.9180, n = 297 cells from 9 mice), which was not observed when we superfused the brain with aCSF that had been osmolarity-matched to the clearing solution with sucrose (20th percentile -21.9%, median -5.9%, mean -3.6, 80th percentile 10.9%, p = 0.0024, two-sided Wilcoxon signed rank test, n = 204 cells from 2 mice). The distributions of intensity changes from baseline following superfusion (Fig. 5D) with the sucrose-based control (blue) and iodixanol-based solution (orange) were significantly different ($p = 3.4495*10^{-61}$, two-sample Kolmogorov-Smirnov test).

We also counted the number of cells in the cleared tissue compared to baseline (Fig. 5E), and observed an increase of 85.9% in cell count (20th percentile 22.3%, median 42.2%, mean 85.9%, 80th percentile 107%, p = 0.0039, two-sided Wilcoxon signed-rank test, Cohen's d 1.2469, n = 237 cells before clearing, n = 368 cells post-clearing, from 9 mice). At least part of the reason for the variability in the observed effect might simply be labeling density: in the cases where little increase in the number of cells is observed it might be that there were in fact very few additional labeled cells available to come into view. Consistent with this hypothesis, it's the animals with the lowest number of pre-clearing cells that show the least improvement.

Generality of the principle - polymers and nanoparticles

Our patch clamping results indicate that the addition of 6% iodixanol to a standard physiological solution does not alter several key properties related to neural physiology (Fig. 1F-1K). Unfortunately, it is known that 40 mM increase in osmolality affects synaptic communication and by extension neural excitability [55,56]. Additionally, we suspect that high osmolarity may pose long-term negative outcomes, and it would be advantageous to employ reagents that, for a given target change in refractive index, require lower osmolarity increases. Corollary, such agents can also be employed at higher concentrations to obtain a higher refractive index change, and hence better imaging quality, while maintaining a target osmolarity change.

A simple strategy is to employ a compound with comparable refractive index but higher molecular weight. Polyethylene glycol (PEG) is a biocompatible polymer that has seen wide use in biological and bioengineering applications [60-64], and that comes in a variety of molecular weights. Using higher molecular weight PEG would yield a lower concentration change (for a given target change in refractive index), at the cost of slower diffusion into the tissue. We tested PEG10,000 (i.e., with 10 kDa molecular weight) at a concentration of 60 mg/ml in aCSF (PEG-aCSF), which had the same refractive index as iodixanol-aCSF (~1.34), but an increase in concentration of only 6 mM, compared to the 40 mM increase seen for iodixanol-aCSF. 6 mM is similar to, or less than, the baseline variability in CSF osmolarity [65-67]. Fig. 6A and Fig. 6B show a representative slice before and after optical clearing with PEG-aCSF using the bead assay. We observed (see Fig. 6E) on average a 521.4% increase in background-subtracted intensity of the beads imaged through the tissue sections (20th percentile 297.9%, median 429.2%, mean 521.4%, 80th percentile 818.7%, Cohen's d 2.2816, n = 82, 124 beads for baseline and after treatment with PEG, respectively, from 4 slices, obtained from 3 mice). The change was significant ($p = 4.4210*10^{-41}$, two-sample Kolmogorov-Smirnov test), and significantly different from the changes observed with 1hr incubation in regular aCSF ($p = 0.0069$, two-sample Kolmogorov-Smirnov test).

While small molecule reagents represent a simple strategy to raise the refractive index of the extracellular space, their relatively low refractive index limits the degree of refractive index matching that can be achieved without excessively altering the osmolarity of the aCSF. For example, assuming a refractive index for lipid membranes of ~1.46 and of ~1.33 for extracellular fluid, for a total difference of 0.13, it would take 260 mM iodixanol (compared to a conventional aCSF osmolarity of ~310 mM) to reduce that mismatch by half. Semiconductor nanoparticles offer a promising alternative, because of the much higher refractive index (Si: $n = 3.97$, Ge: $n = 5.69$) compared to both iodixanol ($n = 1.39$ for a 40% solution in water) and PEG ($n = 1.66$), and thus the much lower osmotic load. Semiconductors, such as silicon, have been shown to be highly biocompatible [68-79], and surface functionalization can be employed to tailor nanoparticles-cells interactions. For example, PEGylation has been shown to reduce protein absorption and cellular uptake [60].

We developed silicon nanoparticles functionalized with PEG1500 (i.e., 1.5 kD molecular weight PEG), both to reduce nanoparticle interactions with proteins and cells [60], and to improve the stability of the nanoparticles in physiological buffers [80]. Obtaining a refractive index change of 0.01 would only require 0.23 mM of Si NPs, a practically negligible amount. As a proof of principle demonstration of this concept we tested Si NPs in acute brain slices, repeating the bead assay employed earlier (see Fig. 6C and Fig. 6D for a representative slice before and after incubation with Si NP-aCSF). Incubation of the slices in aCSF with a concentration of Si NPs yielding a refractive index change of 0.01 led to a 300.7% increase in background-subtracted bead intensity imaged through the tissue sections (see Fig. 6E, 20th percentile 111%, median 171.9%, mean 300.7%, 80th percentile 580.7%, Cohen's d 0.6176, n = 40, 69 beads for baseline and after optical clearing, respectively, from 3 slices, obtained from 2 mice). The change was significant ($p = 5.2458*10^{-8}$, two-sample Kolmogorov-Smirnov test), and significantly different from the changes observed with 1hr incubation in regular aCSF ($p = 0.0145$, two-sample Kolmogorov-Smirnov test).

Discussion

In this chapter we introduce and elucidate the principles that may be used for alleviating the scattering of light, and consequently increasing the transparency, of the living mouse brain.

We show that reducing the refractive index mismatch between lipid membranes and aqueous components by a small amount (~0.01) is sufficient to achieve a measurable change in brain tissue transparency. We tested a multitude of small polar cell membrane permeable reagents [82-84] for this and found that Ethylene glycol and Dimethyl Sulfoxide are able to achieve this. Unfortunately, Ethylene glycol is known to have high systemic toxicity [85-88] and DMSO is known to alter neural physiology [52].

We next show that reducing the refractive index mismatch between cellular membranes and the extracellular space only by a small amount (~0.01) is also sufficient to achieve a measurable and significant change in brain tissue transparency. We demonstrate this versatile approach in brain tissue with the iodinated radiocontrast agent Iodixanol. While iodixanol treatment does not alter key neurophysiological properties significantly, it is expected to affect neural communication due to its high osmolarity [55,56].

It is possible to circumvent this by using very high molecular weight molecules, or macromolecules, which could be added at very low concentrations to achieve a desired refractive index change. We demonstrate this with Polyethylene glycol and PEG-ylated silicon nanoparticles. We discuss the design and deployment of this class of reagents further in the next chapter.

Materials and Methods:

All procedures involving animals were in accordance with the US National Institutes of Health Guide for the Care and Use of Laboratory Animals and approved by the Massachusetts Institute of Technology (MIT) Committee on Animal Care.

Refractive index measurements. All refractive indeces were measured with a Reichert 1310488M Abbe Refractometer (Cole-Parmer).

Slice preparation for bead assays. C57BL/6 mice were deeply anesthetized with a ketamine/xylazine cocktail, then transcardially perfused with ice-cold solution containing, in mM, 252 sucrose, 3 KCl, 1.25 $NaH_2PO_4*2H_2O$, 2 $MgSO_4$, 2 $CaCl_2*2H_2O$, 10 glucose, and 24 $NaHCO_3$, and saturated with 95% oxygen and 5% carbon dioxide. The brain was then extracted and slices 200 (for Si nanoparticle testing) or 250 (for PEG testing) µm thick were cut on a vibratome (Leica Biosystems). The slices were then allowed to recover for at least 30' in an interface holding chamber (Harvard Apparatus), in aCSF containing, in mM, 126 NaCl, 3 KCl, 1.25 $NaH_2PO_4*2H_2O$, 2 $MgSO_4$, 2 $CaCl_2*2H_2O$, 10 glucose, and 24 $NaHCO_3$, and saturated with 95% oxygen and 5% carbon dioxide. Optical clearing solutions were similar to recording aCSF, with the addition of either 100 µl/ml DMSO, 100 µl/ml Ethylene Glycol, 100 µl/ml Propylene Glycol, 60 mg/ml iodixanol, 60 mg/ml PEG 10KDa or a sufficient concentration of Si NPs to obtain a refractive index increment of ~ 0.01. All chemicals, other than the Si NPs, were obtained from Sigma-Aldrich.

Bead assay. Acute brain slices, prepared as described above, were placed in a sealed imaging chamber (VWR) filled with plain aCSF. An array of red (emission, 645 nm) fluorescent 15 µm polystyrene beads (Invitrogen) was then imaged through the slice on an inverted epifluorescence microscope. The slices were then transferred to an incubation chamber containing the clearing solution (e.g. PEG-containing aCSF), which was constantly bubbled with 95% oxygen, 5% carbon dioxide. After one hour the slices were removed from the incubation chamber, rinsed once with plain aCSF, then placed in the sealed imaging chamber, filled with plain aCSF. We then imaged the beads through the slice again, using the same exposure and light intensity settings as before clearing. Data was analyzed using Fiji42–44.

In vitro whole-cell patch clamping. Whole-cell patch-clamp recordings were made using an Axopatch 200B amplifier, a Digidata 1440 digitizer, and a PC running pClamp10.4 (Molecular Devices). For current clamp recordings, neurons were patched at 18-21 days in vitro (DIV) to allow for sodium channel maturation. Neurons were bathed in room-temperature Tyrode's solution containing, in mM, 129 NaCl, 2 KCl, 3 $CaCl_2$, 1 $MgCl_2$, 25 HEPES, 30 glucose, 0.01 NBQX, 0.01 GABAzine and pH adjusted to 7.3 with NaOH or in Tyrode's solution supplemented with either 60mg/ml iodixanol (Iodixanol-Tyrode). Neurons were bathed in Tyrode's solution or iodixanol-Tyrode for at least 15 minutes prior to whole-cell patch clamping. Borosilicate glass pipettes (Warner Instruments) with an outer diameter of 1.2 mm and a wall thickness of 0.255 mm were pulled to a resistance of 5–9 MΩ with a P-97 Flaming/Brown micropipette puller (Sutter Instruments) and filled with a solution containing, in mM, 150 K-gluconate, 8 NaCl, 0.1 $CaCl_2$, 0.6 $MgCl_2$, 1 EGTA, 10 HEPES, 4 Mg-ATP, 0.4 Na-GTP, with pH adjusted to 7.3 with KOH, and osmolarity adjusted to 298 mOsm with sucrose. We used cells with access resistance 5-30 MΩ and holding current within ±50 pA (at −65 mV, in voltage clamp). Access resistance was monitored throughout recording. Data were analyzed using Clampfit (Molecular Devices) and custom MATLAB scripts (MathWorks).

Primary neuron culture. Hippocampal neurons were prepared from postnatal day 0 or 1 Swiss Webster (Taconic) mice as previously described [81] but with the following modifications: dissected hippocampal tissue was digested with 50 units of papain (Worthington Biochem) for 8 min, and the digestion was stopped with ovomucoid trypsin inhibitor (Worthington Biochem). Cells were plated at a density of 16,000–40,000 per glass coverslip coated with Matrigel (BD Biosciences). Neurons were seeded in 90 or 100ul Plating Medium containing MEM(Life Technologies), glucose (33mM, Sigma), transferrin(0.01%, Sigma), HEPES (10mM, Sigma), GlutaGRO (2mM, Corning), Insulin (0.13%, Millipore), B27 supplement (2%, Gibco), heat inactivated fetal bovine serum (7.5%, Corning). After cell adhesion, additional Plating Medium was added. AraC (0.002mM, Sigma) was added when glia density was 50-70%. Neurons were grown at 37C degree and 5% CO2 in a humidified atmosphere.

Virus injection. In order to express iRFP682 [59] in a sparse subset of neurons we injected a mixture of dilute (1:500) AAV2/8-CAG-Cre and AAV2/8-FLEX-iRFP682 in C57BL/6 mice. Under sterile conditions, a small craniotomy was performed, and the viruses were injected at a site -1.5 mm posterior to bregma and 1.5 mm lateral from bregma at a depth of 0.15-0.2 mm. We then allowed at least 4 weeks for the protein to be expressed.

In vivo imaging. On the day of the experiment, with the animal under isoflurane anesthesia (1-2% in O_2), a metal headplate was secured to the skull using dental cement. A craniotomy was then performed at the site of the viral injection, followed by a durotomy. The animal, still kept under isoflurane anesthesia, was then transferred to the custom-built one-photon microscope. For iRFP imaging we used 625nm excitation, with a 664 long pass emission filter (Thorlabs). The headplate holder was secured on a platform mounted on a 3-axis stage, which could be controlled through Micromanager to acquire image stacks. After a baseline stack was taken, with the brain covered with lactated Ringer's solution, the solution of interest (sucrose-HEPES-aCSF control or iodixanol-HEPES-aCSF) was superfused onto the brain. Every 20 minutes, for one hour, it was removed and replaced with fresh solution, to minimize the effects of evaporation. At the end of the hour the solution was removed, the surface rinsed once with lactated Ringer's solution, then fresh lactated Ringer's solution was applied and a new image stack was taken. The composition of the HEPES-aCSF was, in mM: 135 NaCl, 5 KCl, 5 HEPES, 1.8 $CaCl_2*2H_2O$, 1 $MgCl_2*6H_2O$. Iodixanol-HEPES-aCSF contained, in addition, 60 mg/ml iodixanol, whereas sucrose-HEPES-aCSF contained, instead of iodixanol, 40 mM sucrose, as an osmotically matched control.

In vivo imaging data analysis. We first performed background subtraction on the raw image stacks using Fiji42–44, using a 20 pixel radius. That gave a better estimate of the difference in signal intensity between background and cells compared to measuring the raw intensities, but didn't completely eliminate the background, which in some cases had intensities on the order of up to 80% of the signal from the fainter cells. To account for that we measured the mean intensities of 5 patches of the image devoid of neurons but near neurons, at different focal planes, averaged them, and subtracted that value from the intensity values measured at the neurons. As an intensity measure for the neurons we took the peak mean intensity measured for the entire cell across the z-stack. This allowed us to have a good estimate of the change in fluorescence between the cells and the background. Repeating the procedure for estimating background multiple times using different selections gave values within < 10% of each other. All analysis was performed blind to condition.

Reagents and materials for SiNP synthesis and functionalization. Hydrogen silsesquioxane (HSQ, trade name Fox-17) was purchased from Dow Corning and the solvent was removed to yield a white solid that was used directly. Hydrofluoric acid (48–50%) was purchased from Fisher Scientific and used as received. Methyl-10-undecenoate (96%), was purchased from Sigma-Aldrich and used as received. Allyloxy (polyethylene oxide) (35-50 EO, 1500 – 2000 g/mol) was purchased from Gelest Incorporation and heated at 50 °C under Schlenk line vacuum at 0.2 Torr for 48 hours to remove the moisture. All solvents were reagent grade and used as received. Toluene was collected from a Pure-Solv purification system immediately prior to use. All other solvents were reagent grade and Milli-Q water was used throughout the experiment. Amicon Ultra-15 Centrifugal Filter Unit (30K MWCO) was purchased from Sigma Aldrich. Hydrophilic nylon filters (0.20 μm) were purchased from Fischer Scientific.

Synthesis of hydride-terminated silicon nanocrystals (H-SiNCs). H-SiNCs were prepared using a well-established literature procedure46. Briefly, SiNC/SiO_2 composite obtained from reductive thermal processing of HSQ at 1100^o C was etched using ethanolic HF. Following extraction from HF into toluene, the H-SiNCs were isolated by centrifugation at 3000 rpm. The orange/yellow solid redispersed in toluene and activated molecular sieves S4 (4 Å) were added. The suspension was mixed thoroughly using a glass pipet to remove residual moisture and then transferred to another test tube and isolated by centrifugation at 3000 rpm for 5 min (2×).

Thermal hydrosilylation of H-SiNCs with mixed ligands. H-SiNCs were dispersed in 8 mL (ca. 34 mmol) of methyl 10-undecenoate and transferred to a dry Schlenk flask equipped with a magnetic stirrer bar and charged with argon. Subsequently, 3 g (ca. 2.3 mmol) allyloxy (polyethylene oxide) was added. The mixture was subjected to three freeze–pump–thaw cycles using an Ar charged double manifold Schlenk line. After warming to room temperature, the Schlenk flask was transferred to a silicone oil bath pre-heated to 180 °C and stirred for 24 h under Ar. The reaction mixture became transparent within 30 min. After that, the nanocrystals were washed by solvent/antisolvent method. In the first five cycles, chloroform/hexane were used and then ethanol/hexane were used to wash these NCs five times at 5000 RPM.

Figures:

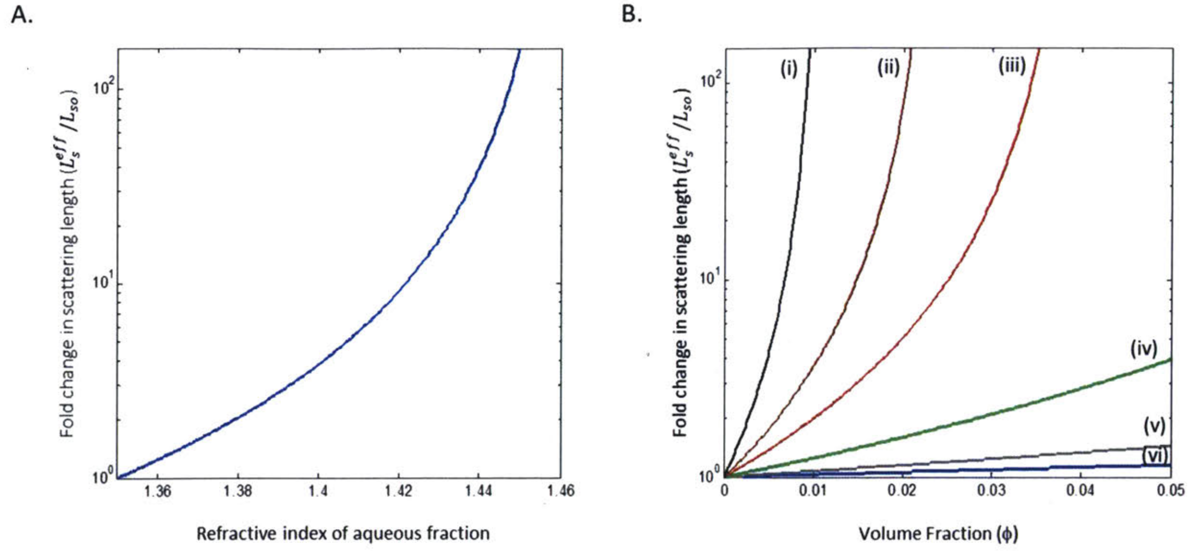

Figure 1. Modeled change in brain scattering length, as a function of aqueous refractive index or volume fraction. (A) Fold change in scattering length as a function of the refractive index of the aqueous fraction, modelled using equations (5) and (6). (B) Change in normalized scattering length as a function of the volume fraction of (i) Germanium (n=5.6), (ii) Silicon (n=3.9), (iii) Cadmium telluride (n=3.12), (iv) Zirconium dioxide (n=2.225), (v) Polyethylene Glycol (n=1.67), and (vi) DMSO (n = 1.479), modeled using equations (5) and (6).

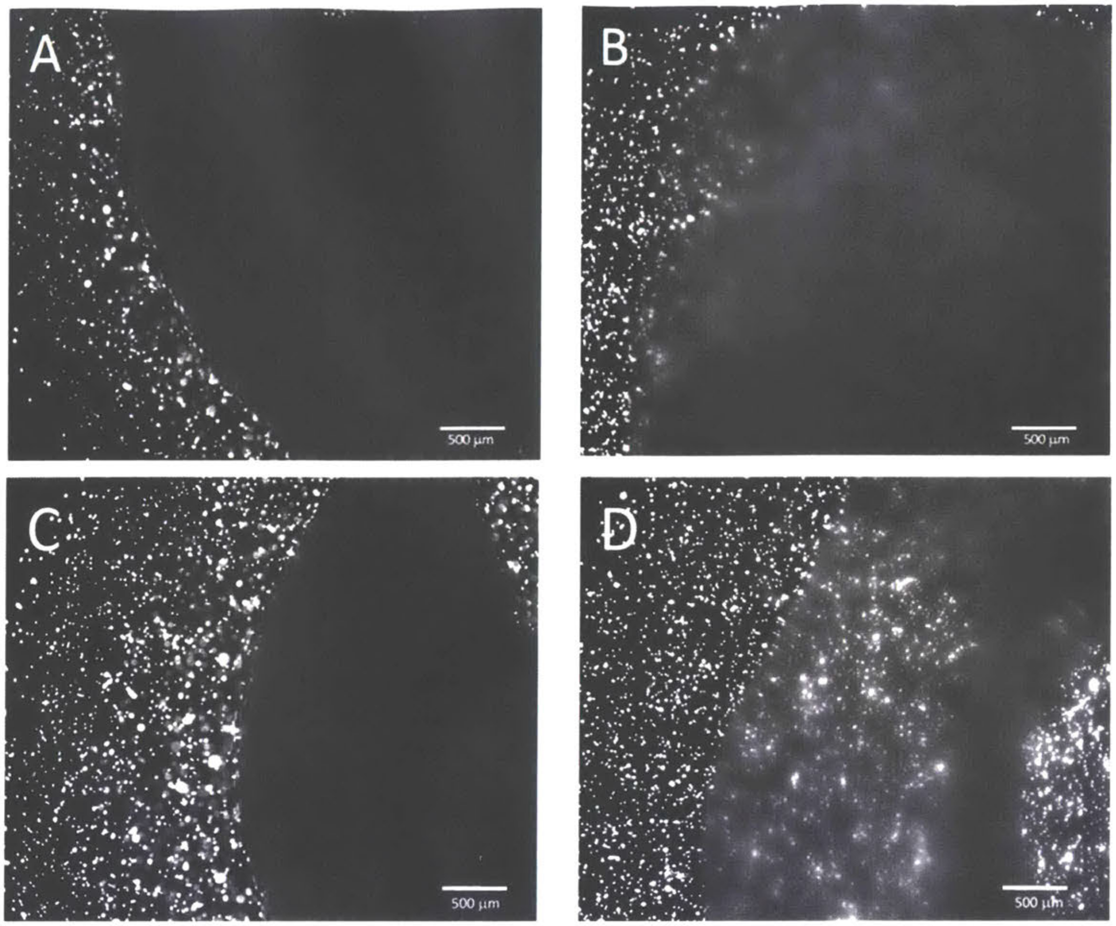

Figure 2. Effect of cell membrane permeable reagents on slice transmittance. (A) Acute 300 µm-thick mouse cortical slice (right), prior to incubation with 10% DMSO in aCSF. Bright speckles are fluorescent beads (emitting 645 nm light, size, 15 µm). (B) A brain slice, but after 60 min incubation with a 10% DMSO in aCSF. (C) Acute 300 µm-thick mouse cortical slice (right), prior to incubation with 10% Ethylene Glycol in aCSF. (D) A brain slice, but after 60 min incubation with a 10% Ethylene Glycol in aCSF. Slices were placed in a 500mm-deep chamber, and imaged from the bottom; on top (i.e., behind the slice in these images) was placed a target slide with the deposited fluorescent beads.

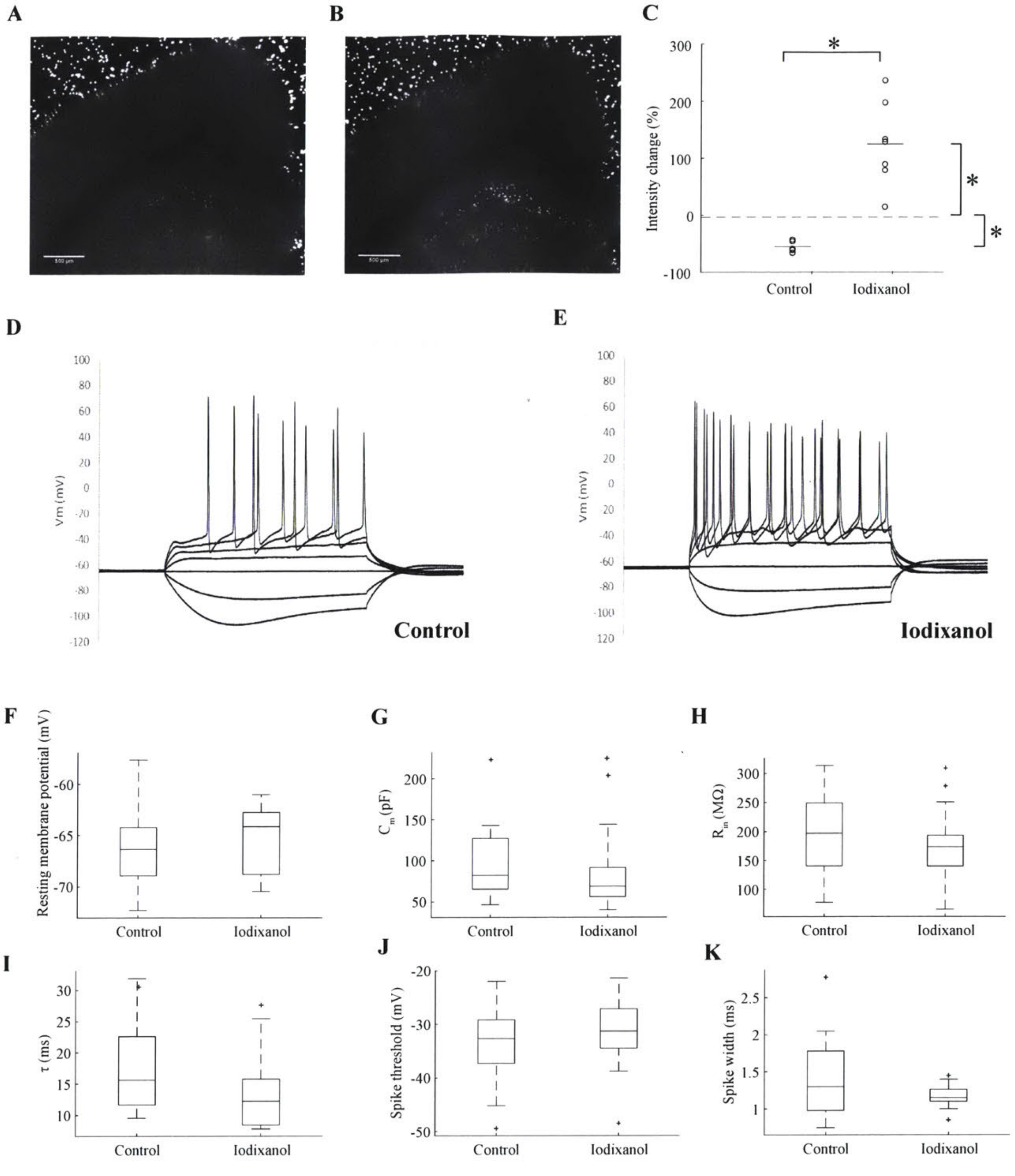

Figure 3. Effect of iodixanol-aCSF on slice transmittance and neural properties. Array of 15µm-diameter far-red beads imaged through a 250µm acute brain slice. (A) Baseline. (B) After 1hr incubation in iodixanol-aCSF, with a refractive index 0.01 greater than plain aCSF. (C) Change in intensity above background in the signal recorded from the beads imaged through the tissue section, for regular aCSF and iodixanol-aCSF. Each circle represents a slice, line segments indicate means, dashed lines indicate 0 (no change). The change from baseline in the distribution of bead background-subtracted intensities after 1hr incubation in plain aCSF (20th percentile -64.3414%,

median -60.1863%, mean -55.8561%, 80th percentile -45,2058% , p = 0.0201, two-sample Kolmogorov-Smirnov test, n = 51 beads before, 46 after incubation, from 5 slices from 2 mice) and in iodixanol-aCSF (20th percentile 71.3561%, median 127.6292%, mean 124.3961%, 80th percentile 200.3645%, p = 4.3646*10-6, two-sample Kolmogorov-Smirnov test, n = 244 beads for the cleared condition, 90 beads for baseline, from 7 slices obtained from 3 mice,) were significant, and significantly different from each other (p = 0.0016, two-sample Kolmogorov-Smirnov test, n = 7 slices from 3 mice for iodixanol-aCSF, n = 5 slices from 2 mice for plain aCSF). Electrophysiological properties for control cells (n = 15, from three cultures) and cells incubated in iodixanol-Tyrode's solution with a refractive index 0.01 greater than plain Tyrode's solution (n = 14 from two cultures). (D) Resting membrane potential (p = 0.80993, two-sample Kolmogorov-Smirnov test). (E) Membrane capacitance (p = 0.68089, two-sample Kolmogorov-Smirnov test). (F) Input resistance (p = 0.5606 two-sample Kolmogorov-Smirnov test). (G) Membrane time constant (p = 0.29588 two-sample Kolmogorov-Smirnov test). (H) Spike threshold (p = 0.19992, two-sample Kolmogorov-Smirnov test). (I) Spike width (p = 0.18856, two-sample Kolmogorov-Smirnov test).

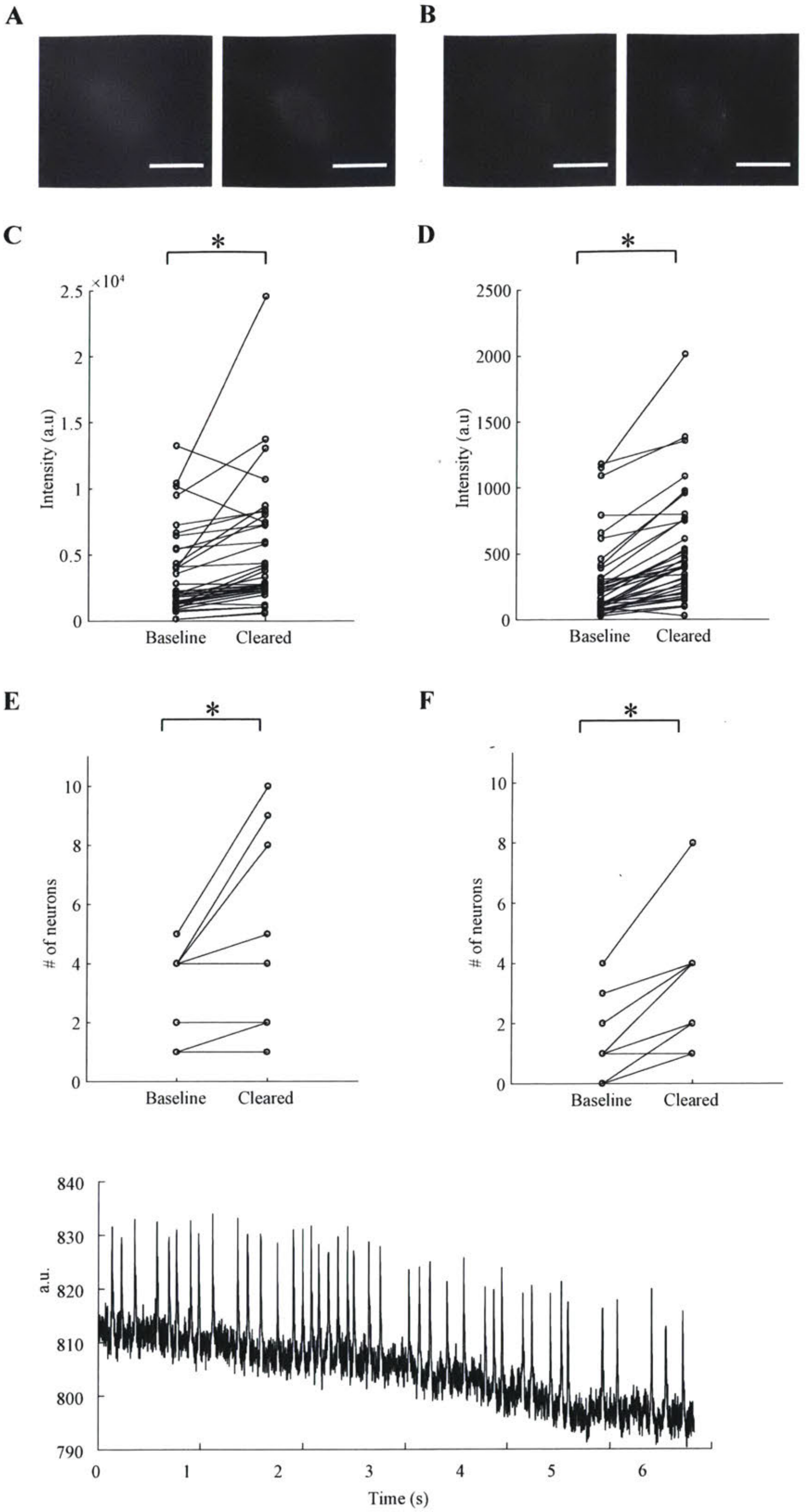

Figure 4. Optical clearing is compatible with the use of the model far-red voltage sensor Archon and enhances the signal from both green and far-red fluorophores. (A) The same neuron imaged in the green channel (475/28nm excitation, emission 535/22nm band-pass filter) before (left) and

after (right) optical clearing. Scale bars are 10μm (B) as in (A), for the far-red channel (627nm excitation, emission 664nm long pass filter). Each pair of before and after images were acquired with the same settings and have been stretched identically for display. Scale bars are 10μm (C) Fluorescence intensity, after subtracting background, of cells expressing both GFP and Archon, imaged in the green (475/28nm excitation, emission 535/22nm band-pass filter) channel before and after 1hr superfusion of the slices with iodixanol-aCSF with a refractive index 0.01 greater than plain aCSF ($p = 1.2569*10^{-5}$, two-sided Wilcoxon signed rank test, n = 28 neurons from 8 slices, obtained from 4 mice (D) as in (C), for the far-red (627nm excitation, emission 664nm long pass filter) channel ($p = 1.8650*10^{-7}$, two-sided Wilcoxon signed rank test, n = 28 neurons from 8 slices, obtained from 4 mice (E) Number of neurons visible in each slice before and after optical clearing, when imaging in the green channel (p = 0.0625, two-sided Wilcoxon signed rank test, 8 slices, obtained from 4 mice). (F) As in (E), for the far-red channel (p = 0.0313, two-sided Wilcoxon signed rank test, 8 slices, obtained from 4 mice). (G) Representative trace recorded from a neuron expressing the voltage sensor Archon, after 1hr superfusion with iodixanol-aCSF, while iodixanol-aCSF was still being superperfused.

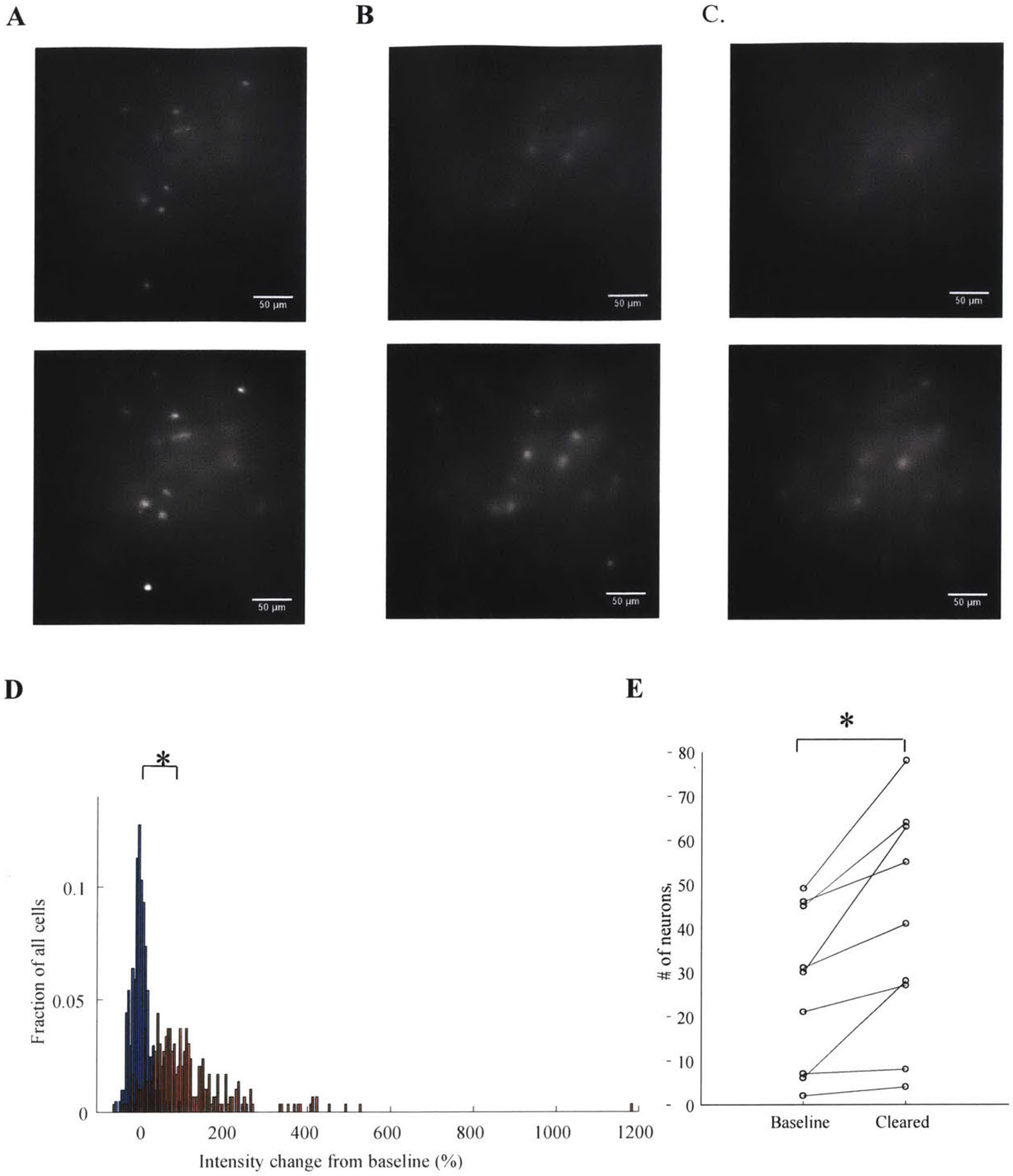

Figure 5. In vivo optical clearing through cortical superfusion with iodixanol-HEPES-aCSF, with a refractive index 0.01 greater than that of regular HEPES-aCSF. (A) through (C) Corresponding optical slices taken from progressively greater depths within the brain, before (top) and after (bottom) 1hr superfusion with iodixanol-HEPES-aCSF. (D) Histogram showing the percentage change from baseline in intensity above background of the signal recorded for each given cell, for 1hr superfusion with sucrose-HEPES-aCSF (blue, osmotically-matched control) and iodixanol-HEPES-aCSF (red, optical clearing agent). The two distributions are significantly different (p =

$3.4495*10^{-61}$, two-sample Kolmogorov-Smirnov test). (E) Number of cells visible in the background-subtracted maximum-intensity projections, before and after optical clearing ($p = 0.0039$, two-sided Wilcoxon signed-rank test, $n = 237$ cells before clearing, $n = 368$ cells post-clearing, from 9 mice)

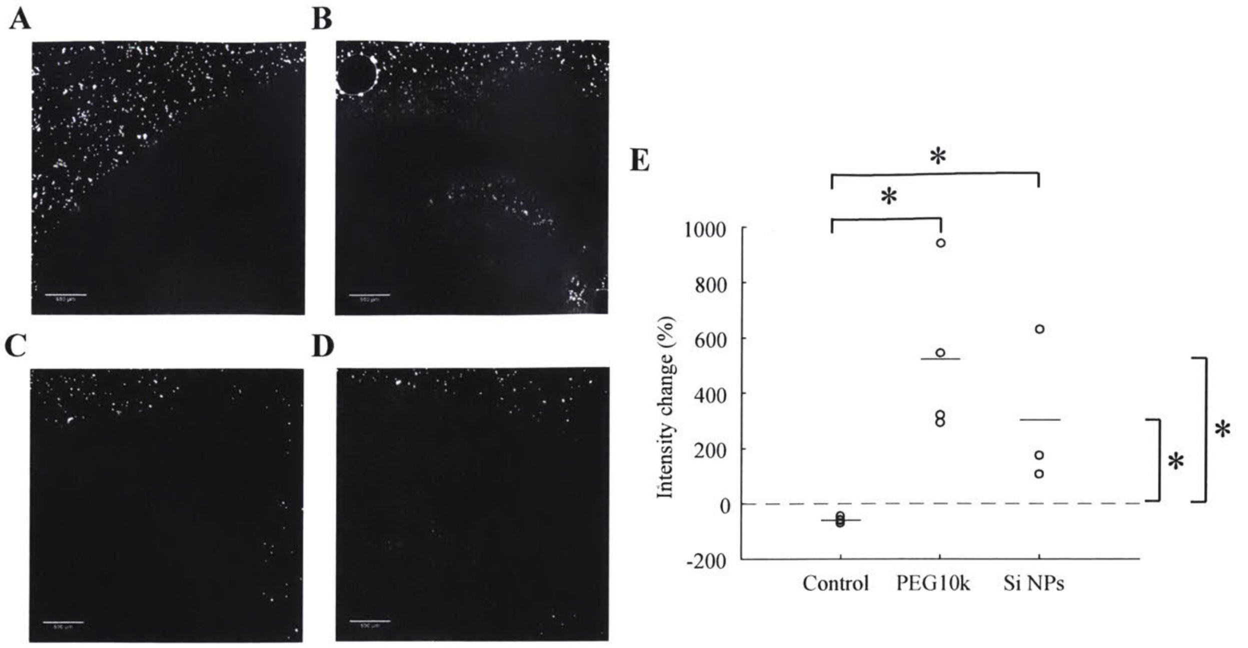

Figure 6. Effect of PEG and PEG-ylated silicon nanoparticles on slice transmittance. (A) Array of 15 µm far red (emission 645 nm) polystyrene beads imaged though a 250µm-thick acute brain slice. (B) Same slice and setup as in (A), after 1hr incubation in PEG-aCSF. (C) Array of 15 µm far red (emission 645 nm) polystyrene beads imaged through a 200 µm-thick acute brain slice. (D) Same slice as (C), after incubation for 1hr in Si NPs-aCSF. (E) Changes in intensity above background for beads imaged after 1hr incubation with a given reagent compared to baseline. Each circle represents a slice, line segments indicate means, dashed lines indicate 0 (no change). Control aCSF (20th percentile -64.3414%, median -60.1863%, mean -55.8561%, 80th percentile -45,2058% , p = 0.0201, two-sample Kolmogorov-Smirnov test, n = 51 beads before, 46 after incubation, from 5 slices from 2 mice), PEG-aCSF ((20th percentile 297.9418 %, median 429.2093%, mean 521.4226%, 80th percentile 818.6741%, $p = 4.4210*10^{-41}$, two-sample Kolmogorov-Smirnov test, n = 82, 124 beads for baseline and after optical clearing, respectively, from 4 slices, obtained from 3 mice), and Si NPs-aCSF (20th percentile 110.9638%, median 171.9474%, mean 300.7460%, 80th percentile 580.6873%, $p = 5.2458*10^{-8}$, two-sample Kolmogorov-Smirnov test, n = 40, 69 beads for baseline and after optical clearing, respectively, from 3 slices, obtained from 2 mice). The changes for incubation in PEG-aCSF and Si NPs-aCSF were significantly different from the changes observed with incubation in control aCSF (p = 0.0069, p = 0.0145, two-sample Kolmogorov-Smirnov test, respectively, n = 5 slices from 2 mice for control aCSF, n = 4 slices from 3 mice for PEG-aCSF, n = 3 slices from 2 mice for Si NP-aCSF).

References

1. Chen, T.-W. *et al.* Ultrasensitive fluorescent proteins for imaging neuronal activity. *Nature* **499**, 295–300 (2013).
2. Gong, Y. *et al.* High-speed recording of neural spikes in awake mice and flies with a fluorescent voltage sensor. *Science* **350**, 1361–1366 (2015).
3. Piatkevich, K. D. *et al.* A robotic multidimensional directed evolution approach applied to fluorescent voltage reporters. *Nature Chemical Biology* **14**, 352–360 (2018).
4. Abdelfattah, A. S. *et al.* Bright and photostable chemigenetic indicators for extended in vivo voltage imaging. doi:10.1101/436840
5. Piatkevich, K. D. *et al.* Population imaging of neural activity in awake behaving mice in multiple brain regions. doi:10.1101/616094
6. Marvin, J. S. *et al.* An optimized fluorescent probe for visualizing glutamate neurotransmission. *Nature Methods* **10**, 162–170 (2013).
7. Helassa, N. *et al.* Ultrafast glutamate sensors resolve high-frequency release at Schaffer collateral synapses. *Proc. Natl. Acad. Sci. U. S. A.* **115**, 5594–5599 (2018).
8. Martineau, M. *et al.* Semisynthetic fluorescent pH sensors for imaging exocytosis and endocytosis. *Nat. Commun.* **8**, 1412 (2017).
9. Mountcastle, V. The columnar organization of the neocortex. *Brain* **120**, 701–722 (1997).
10. Hubel, D. H. & Wiesel, T. N. Receptive fields, binocular interaction and functional architecture in the cat's visual cortex. *The Journal of Physiology* **160**, 106–154 (1962).
11. Douglas, R. J., Martin, K. A. C. & Whitteridge, D. A Canonical Microcircuit for Neocortex. *Neural Computation* **1**, 480–488 (1989).
12. Douglas, R. J. & Martin, K. A. C. NEURONAL CIRCUITS OF THE NEOCORTEX. *Annual Review of Neuroscience* **27**, 419–451 (2004).
13. Badon, A., Claude Boccara, A., Lerosey, G., Fink, M. & Aubry, A. Multiple scattering limit in optical microscopy. *Optics Express* **25**, 28914 (2017).
14. Wilt, B. A. *et al.* Advances in Light Microscopy for Neuroscience. *Annu. Rev. Neurosci.* **32**, 435 (2009).
15. Oheim, M., Beaurepaire, E., Chaigneau, E., Mertz, J. & Charpak, S. Two-photon microscopy in brain tissue: parameters influencing the imaging depth. *J. Neurosci. Methods* **111**, 29–37 (2001).
16. Johnsen, S. & Widder, E. A. The Physical Basis of Transparency in Biological Tissue: Ultrastructure and the Minimization of Light Scattering. *Journal of Theoretical Biology* **199**, 181–198 (1999).
17. Jacques, S. L. Optical properties of biological tissues: a review. *Physics in Medicine and Biology* **58**, R37–R61 (2013).
18. Ji, N., Freeman, J. & Smith, S. L. Technologies for imaging neural activity in large volumes. *Nat. Neurosci.* **19**, 1154–1164 (2016).
19. Helmchen, F. Two-Photon Functional Imaging of Neuronal Activity. *In Vivo Optical Imaging of Brain Function, Second Edition* 37–58 (2009). doi:10.1201/9781420076851.ch2
20. Reddy, D. & Saggau, P. Fast Three-Dimensional Random Access Multi-Photon Microscopy for Functional Recording of Neuronal Activity. *Confocal, Multiphoton, and Nonlinear Microscopic Imaging III* (2007). doi:10.1364/ecbo.2007.6630_45

21. Flusberg, B. A. *et al.* High-speed, miniaturized fluorescence microscopy in freely moving mice. *Nat. Methods* **5**, 935–938 (2008).
22. Dombeck, D. A., Harvey, C. D., Tian, L., Looger, L. L. & Tank, D. W. Functional imaging of hippocampal place cells at cellular resolution during virtual navigation. *Nat. Neurosci.* **13**, 1433–1440 (2010).
23. Si, K., Fiolka, R. & Cui, M. Fluorescence imaging beyond the ballistic regime by ultrasound pulse guided digital phase conjugation. *Nat. Photonics* **6**, 657–661 (2012).
24. McDowell, E. J. *et al.* Turbidity suppression from the ballistic to the diffusive regime in biological tissues using optical phase conjugation. *J. Biomed. Opt.* **15**, 025004 (2010).
25. Wang, Y. M., Judkewitz, B., Dimarzio, C. A. & Yang, C. Deep-tissue focal fluorescence imaging with digitally time-reversed ultrasound-encoded light. *Nat. Commun.* **3**, 928 (2012).
26. Yaqoob, Z., Psaltis, D., Feld, M. S. & Yang, C. OPTICAL PHASE CONJUGATION FOR TURBIDITY SUPPRESSION IN BIOLOGICAL SAMPLES. *Nat. Photonics* **2**, 110–115 (2008).
27. Cui, M. & Yang, C. Implementation of a digital optical phase conjugation system and its application to study the robustness of turbidity suppression by phase conjugation. *Optics Express* **18**, 3444 (2010).
28. Hsieh, C.-L., Pu, Y., Grange, R. & Psaltis, D. Digital phase conjugation of second harmonic radiation emitted by nanoparticles in turbid media. *Opt. Express* **18**, 12283–12290 (2010).
29. Cui, M. A high speed wavefront determination method based on spatial frequency modulations for focusing light through random scattering media. *Opt. Express* **19**, 2989–2995 (2011).
30. McCabe, D. J. *et al.* Spatio-temporal focusing of an ultrafast pulse through a multiply scattering medium. *Nat. Commun.* **2**, 447 (2011).
31. Wang, L. V. & Hu, S. Photoacoustic tomography: in vivo imaging from organelles to organs. *Science* **335**, 1458–1462 (2012).
32. Yang, X., Pu, Y. & Psaltis, D. Imaging blood cells through scattering biological tissue using speckle scanning microscopy. *Opt. Express* **22**, 3405–3413 (2014).
33. Draijer, M., Hondebrink, E., van Leeuwen, T. & Steenbergen, W. Review of laser speckle contrast techniques for visualizing tissue perfusion. *Lasers Med. Sci.* **24**, 639–651 (2009).
34. Hajjarian, Z., Xi, J., Jaffer, F. A., Tearney, G. J. & Nadkarni, S. K. Intravascular laser speckle imaging catheter for the mechanical evaluation of the arterial wall. *J. Biomed. Opt.* **16**, 026005 (2011).
35. Lev, A. & Sfez, B. In vivo demonstration of the ultrasound-modulated light technique. *J. Opt. Soc. Am. A Opt. Image Sci. Vis.* **20**, 2347–2354 (2003).
36. Hama, H. *et al.* Scale: a chemical approach for fluorescence imaging and reconstruction of transparent mouse brain. *Nat. Neurosci.* **14**, 1481–1488 (2011).
37. Chung, K. *et al.* Structural and molecular interrogation of intact biological systems. *Nature* **497**, 332–337 (2013).
38. Dodt, H.-U. *et al.* Ultramicroscopy: three-dimensional visualization of neuronal networks in the whole mouse brain. *Nat. Methods* **4**, 331–336 (2007).
39. Chen, F., Tillberg, P. W. & Boyden, E. S. Expansion microscopy. *Science* **347**, 543–548 (2015).
40. Yu, T. & Zhu, D. Clarity and Immunofluorescence on Mouse Brain Tissue. *Curr. Protoc. Neurosci.* **83**, e46 (2018).

41. Reis, J. C. R., Iglesias, T. P., Douhéret, G. & Davis, M. I. The permittivity of thermodynamically ideal liquid mixtures and the excess relative permittivity of binary dielectrics. *Phys. Chem. Chem. Phys.* **11**, 3977–3986 (2009).
42. Sdobnov, A. Y. *et al.* Recent progress in tissue optical clearing for spectroscopic application. *Spectrochim. Acta A Mol. Biomol. Spectrosc.* **197**, 216–229 (2018).
43. Graaff, R. *et al.* Reduced light-scattering properties for mixtures of spherical particles: a simple approximation derived from Mie calculations. *Appl. Opt.* **31**, 1370–1376 (1992).
44. Al-Juboori, S. I. *et al.* Light scattering properties vary across different regions of the adult mouse brain. *PLoS One* **8**, e67626 (2013).
45. Blanchard, C., Portí, J. A., Morente, J. A., Salinas, A. & Navarro, E. A. Determination of the effective permittivity of dielectric mixtures with the transmission line matrix method. *Journal of Applied Physics* **102**, 064101 (2007).
46. Capretti, A., Lesage, A. & Gregorkiewicz, T. Integrating Quantum Dots and Dielectric Mie Resonators: A Hierarchical Metamaterial Inheriting the Best of Both. *ACS Photonics* **4**, 2187–2196 (2017).
47. Yu, F., Zhang, L. & Guo, K. Exciton effects on the refractive index and optical absorption in wurtzite quantum wells via a fractional-dimensional space approach. *Superlattices and Microstructures* **50**, 128–138 (2011).
48. Algarni, H., Bouarissa, N., Ajmal Khan, M., Al-Hagan, O. A. & Alhuwaymel, T. F. Optical constants and exciton properties of ZnxCd1-xS. *Optik* **193**, 163022 (2019).
49. LeBel, R. G. & Goring, D. A. I. Density, Viscosity, Refractive Index, and Hygroscopicity of Mixtures of Water and Dimethyl Sulfoxide. *Journal of Chemical & Engineering Data* **7**, 100–101 (1962).
50. Garaschuk, O., Milos, R.-I. & Konnerth, A. Targeted bulk-loading of fluorescent indicators for two-photon brain imaging in vivo. *Nat. Protoc.* **1**, 380–386 (2006).
51. Stosiek, C., Garaschuk, O., Holthoff, K. & Konnerth, A. In vivo two-photon calcium imaging of neuronal networks. *Proceedings of the National Academy of Sciences* **100**, 7319–7324 (2003).
52. Tamagnini, F., Scullion, S., Brown, J. T. & Randall, A. D. Low concentrations of the solvent dimethyl sulphoxide alter intrinsic excitability properties of cortical and hippocampal pyramidal cells. *PLoS One* **9**, e92557 (2014).
53. Levinson, A. THE REFRACTOMETRIC AND VISCOSIMETRIC INDEXES OF CEREBROSPINAL FLUID. *Archives of Internal Medicine* **37**, 144 (1926).
54. Meyer, R. A. Light scattering from biological cells: dependence of backscatter radiation on membrane thickness and refractive index. *Appl. Opt.* **18**, 585–588 (1979).
55. Ballyk, B. A., Quackenbush, S. J. & Andrew, R. D. Osmotic effects on the CA1 neuronal population in hippocampal slices with special reference to glucose. *Journal of Neurophysiology* **65**, 1055–1066 (1991).
56. Saly, V. & Andrew, R. D. CA3 neuron excitation and epileptiform discharge are sensitive to osmolality. *Journal of Neurophysiology* **69**, 2200–2208 (1993).
57. Häussler, M. D. Safety and patient comfort with iodixanol: A postmarketing surveillance study in 9515 patients undergoing diagnostic CT examinations. *Acta Radiologica* **51**, 924–933 (2010).
58. Boothe, T. *et al.* A tunable refractive index matching medium for live imaging cells, tissues and model organisms. *Elife* **6**, (2017).

59. Shcherbakova, D. M. & Verkhusha, V. V. Near-infrared fluorescent proteins for multicolor in vivo imaging. *Nat. Methods* **10**, 751–754 (2013).
60. Pelaz, B. *et al.* Surface Functionalization of Nanoparticles with Polyethylene Glycol: Effects on Protein Adsorption and Cellular Uptake. *ACS Nano* **9**, 6996–7008 (2015).
61. Zhang, M., Li, X. H., Gong, Y. D., Zhao, N. M. & Zhang, X. F. Properties and biocompatibility of chitosan films modified by blending with PEG. *Biomaterials* **23**, 2641–2648 (2002).
62. Wang, Q., Dong, Z., Du, Y. & Kennedy, J. F. Controlled release of ciprofloxacin hydrochloride from chitosan/polyethylene glycol blend films. *Carbohydrate Polymers* **69**, 336–343 (2007).
63. Alcantar, N. A., Aydil, E. S. & Israelachvili, J. N. Polyethylene glycol-coated biocompatible surfaces. *J. Biomed. Mater. Res.* **51**, 343–351 (2000).
64. Zalipsky, S. Functionalized Poly(ethylene glycols) for Preparation of Biologically Relevant Conjugates. *Bioconjugate Chemistry* **6**, 150–165 (1995).
65. Donato, T., Shapira, Y., Artru, A. & Powers, K. Effect of mannitol on cerebrospinal fluid dynamics and brain tissue edema. *Anesth. Analg.* **78**, 58–66 (1994).
66. Polderman, K. H., van de Kraats, G., Dixon, J. M., Vandertop, W. P. & Girbes, A. R. J. Increases in spinal fluid osmolarity induced by mannitol. *Crit. Care Med.* **31**, 584–590 (2003).
67. Arieff, A. I., Kleeman, C. R., Keushkerian, A. & Bagdoyan, H. Brain tissue osmolality: method of determination and variations in hyper- and hypo-osmolar states. *J. Lab. Clin. Med.* **79**, 334–343 (1972).
68. Park, J.-H. *et al.* Biodegradable luminescent porous silicon nanoparticles for in vivo applications. *Nat. Mater.* **8**, 331–336 (2009).
69. Bimbo, L. M. *et al.* Biocompatibility of thermally hydrocarbonized porous silicon nanoparticles and their biodistribution in rats. *ACS Nano* **4**, 3023–3032 (2010).
70. Ruizendaal, L. *et al.* Synthesis and cytotoxicity of silicon nanoparticles with covalently attached organic monolayers. *Nanotoxicology* **3**, 339–347 (2009).
71. Wang, Q. *et al.* Uptake and toxicity studies of poly-acrylic acid functionalized silicon nanoparticles in cultured mammalian cells. *Adv. Healthc. Mater.* **1**, 189–198 (2012).
72. Ivanov, S. *et al.* In Vivo Toxicity of Intravenously Administered Silica and Silicon Nanoparticles. *Materials* **5**, 1873–1889 (2012).
73. Tanaka, T. *et al.* In vivo evaluation of safety of nanoporous silicon carriers following single and multiple dose intravenous administrations in mice. *Int. J. Pharm.* **402**, 190–197 (2010).
74. Kang, S.-K. *et al.* Dissolution chemistry and biocompatibility of silicon- and germanium-based semiconductors for transient electronics. *ACS Appl. Mater. Interfaces* **7**, 9297–9305 (2015).
75. Erogbogbo, F. *et al.* Biocompatible luminescent silicon quantum dots for imaging of cancer cells. *ACS Nano* **2**, 873–878 (2008).
76. Erogbogbo, F. *et al.* Biocompatible magnetofluorescent probes: luminescent silicon quantum dots coupled with superparamagnetic iron(III) oxide. *ACS Nano* **4**, 5131–5138 (2010).
77. Bayliss, S. C., Buckberry, L. D., Fletcher, I. & Tobin, M. J. The culture of neurons on silicon. *Sensors and Actuators A: Physical* **74**, 139–142 (1999).
78. Hwang, S.-W. *et al.* Dissolution chemistry and biocompatibility of single-crystalline silicon nanomembranes and associated materials for transient electronics. *ACS Nano* **8**, 5843–5851 (2014).
79. Karatutlu, A. *et al.* Synthesis and structure of free-standing germanium quantum dots and their application in live cell imaging. *RSC Advances* **5**, 20566–20573 (2015).

80. Mei, B. C., Susumu, K., Medintz, I. L. & Mattoussi, H. Polyethylene glycol-based bidentate ligands to enhance quantum dot and gold nanoparticle stability in biological media. *Nat. Protoc.* **4**, 412–423 (2009).
81. Klapoetke, N. C. *et al.* Independent optical excitation of distinct neural populations. *Nat. Methods* **11**, 338–346 (2014).
82. Peterlin, P., Arrigler, V., Diamant, H. & Haleva, E. Permeability of Phospholipid Membrane for Small Polar Molecules Determined from Osmotic Swelling of Giant Phospholipid Vesicles. *Advances in Planar Lipid Bilayers and Liposomes Volume 16* 301–335 (2012). doi:10.1016/b978-0-12-396534-9.00010-6
83. Lee, B. W. *et al.* Structural effects of small molecules on phospholipid bilayers investigated by molecular simulations. *Fluid Phase Equilibria* **228-229**, 135–140 (2005).
84. Uzman, A. Molecular Cell Biology (4th edition) Harvey Lodish, Arnold Berk, S. Lawrence Zipursky, Paul Matsudaira, David Baltimore and James Darnell; Freeman & Co., New York, NY, 2000, 1084 pp., list price $102.25, ISBN 0-7167-3136-3. *Biochemistry and Molecular Biology Education* **29**, 126–128 (2001).
85. Jacobsen, D., Ovrebø, S., Ostborg, J. & Sejersted, O. M. Glycolate causes the acidosis in ethylene glycol poisoning and is effectively removed by hemodialysis. *Acta Med. Scand.* **216**, 409–416 (1984).
86. Lim, J., Mearns, A. & Gresham, C. Ethylene glycol poisoning: mind the gap. *N. Z. Med. J.* **132**, 74–78 (2019).
87. Tuero, G. et al. Value of glycolic acid analysis in ethylene glycol poisoning: A clinical case report and systematic review of the literature. *Forensic Sci. Int.* **290**, e9–e14 (2018).
88. Vale, J. A. & Meredith, T. J. Ethylene Glycol Poisoning. *Poisoning Diagnosis and Treatment* 131–134 (1981). doi:10.1007/978-94-011-6763-5_20

Chapter 2: Optical clearing a living mouse brain using Macromolecules

Dehydrating tissues [1,2], hyperhydrating tissues [3,4], removing lipids from tissues [5], physically expanding tissues to dilute their components [6], and refractive index matching tissues in aqueous solution [7] are all strategies that have been used to increase the optical transparency of non-living brain specimens. Of these strategies, only the last option could, in principle, be adapted to the living brain, since the other approaches would not be compatible with normal neural survival and physiology. We accordingly decided to focus on the possibility of reducing the refractive index mismatch between the cell membrane (n ~1.469) and the extracellular space (n ~1.33 for cerebrospinal fluid [8]) by adding a high refractive index, biocompatible molecule to the extracellular space. Since neurons are sensitive to changes in extracellular solution osmolarity [9–15], we sought to use very high molecular weight molecules, which could be added at low concentrations to achieve a desired refractive index change. In particular, the natural variation in the osmolarity of cerebrospinal fluid and interstitial fluid is around 10 milliosmolar [16–18], so we sought to identify and design biocompatible molecules that would be able to increase the refractive index of the extracellular space by a target amount, 0.01, at final concentrations of <10 mM.

Optical Clearing using Polyethylene glycol (PEG)

We first considered PEG, a highly biocompatible polymer that is used in a wide variety of biological and medical applications [19–23], and which is available in a variety of molecular weights. Using PEG of as high a molecular weight as possible would enable very low concentrations to be used, for a given desired increase in refractive index, but perhaps at the expense of slower diffusion into brain tissue. We chose to use PEG of 10 kilodalton (kDa) molecular weight ("PEG10k"), since it would only require a concentration of 60 mg/ml, or 6 mM, to achieve an extracellular space refractive index increase of 0.01. To evaluate candidate live clearing molecules, we imaged 15μm-diameter (i.e., approximately neural cell body sized) red fluorescent (i.e. 645 nm emission) beads through mouse somatosensory cortex acute brain slices (250 μm thick) placed in an imaging chamber filled with artificial cerebrospinal fluid (aCSF) (Fig. 1A). We used red emitting beads since green emitting ones were not visible at all through such brain slices. We incubated slices for 1 hour in aCSF containing 60 mg/mL PEG10k, then washed them with regular aCSF, and imaged the beads through the slice again, in regular aCSF (Fig. 1B). This process increased the intensity of the signal from the beads (after background subtraction) by an average of +521% (Fig. 1C; 20th percentile +297.9%, median +429.2%, mean +521.4%, 80th percentile +818.7%, Cohen's d 2.2816, n = 82, 124 beads for pre- vs. post-optical clearing, respectively, from 4 slices, obtained from 3 mice). This change was significant (p = 4.4210*10-41, two-sample Kolmogorov-Smirnov test), and significantly different from the minor changes (p = 0.0201, two-sample Kolmogorov-Smirnov test, n = 51 beads before, 46 after incubation, from 5 slices from 2 mice) observed with 1 hour incubation in regular aCSF (p = 0.0069, two-sample Kolmogorov-Smirnov test, n = 4 slices from 3 mice for PEG-containing aCSF vs. n = 5 slices from 2 mice for regular aCSF).

We next explored in vivo optical clearing of the live mouse brain with PEG10k. We sparsely expressed the red fluorescent protein iRFP682 [24] via adeno-associated virus (AAV) in the mouse primary somatosensory cortex (S1), and then under anesthesia we imaged the cortical surface under normal lactated Ringer's solution. We then superfused onto the cortical surface, for 1 hour, aCSF containing either 6 mM PEG10k, or 6 mM sucrose as a control, washing the surface with lactated Ringer's solution at the end. Representative optical slices taken via one-photon epifluorescent imaging at progressively greater depths pre- (top) vs. post- (bottom) PEG-containing aCSF superfusion are shown in Fig. 2A-2C. Cells appear brighter, and in greater numbers, after optical clearing. Quantitatively, the intensity of cells (after background subtraction) increased by an average of +130% after optical clearing vs. beforehand (Fig. 2D, orange; 20th percentile +38.8%, median +94.1%, mean +130.4%, 80th percentile +196.8%, $p = 2.1086*10^{-65}$, two-sided Wilcoxon signed rank test, Cohen's d 0.9319, n = 401 cells from 6 mice), which was not observed when we superfused the brain with aCSF with sucrose (Fig. 2D, blue; n = 122 cells from 2 mice); the effects of adding PEG10k vs. sucrose were highly significantly different ($p = 5.4920*10^{-61}$, two-sample Kolmogorov-Smirnov test). As another measure of in vivo clearing, we counted the number of cells visible in the cleared tissue compared to baseline, and observed an increase of +61.5% in cell count (Fig. 2E; 20th percentile +37%, median +51.3%, mean +61.5%, 80th percentile +98.8%, p = 0.0313, two-sided Wilcoxon signed-rank test, Cohen's d 2.0910, n = 458 cells before clearing, n = 729 cells post-clearing, from 6 mice), whereas this was not seen when aCSF containing 6 mM sucrose was used (Fig. 2F; p = 0.500, two-sided Wilcoxon signed-rank test, n =159 neurons before incubation, n = 87 neurons after, from 2 mice).

We chose PEG10k, as noted above, to minimize the concentration needed to achieve a 0.01 refractive index change. We next sought to determine whether that small concentration altered normal neurophysiology. We performed whole-cell patch clamp recording of cultured primary mouse hippocampal neurons pre-incubated for 15 minutes in Tyrode's solution supplemented with 60 mg/ml PEG10k and recorded neurons while in the same solution (incubated for up to one hour), comparing to recordings of cells from the same culture kept in regular Tyrode's solution. The resultant traces (e.g., in response to current injections of -100 to 250 pA in 50 pA steps) were similar, with no differences in resting membrane potential (Fig. 3A), input resistance (Fig. 3B), membrane capacitance (Fig. 3C), membrane time constant (Fig. 3D), spike threshold (Fig. 3E), or spike width (Fig. 3F), between the PEG10k vs. control cases (p = 0.42523, 0.91103, 0.49581, 0.42523, 0.72794, and 0.61022 respectively, two-sample Kolmogorov-Smirnov test, n = 15 neurons from one culture incubated in PEG-containing Tyrode's solution, n = 17 neurons from the same culture incubated in control Tyrode's solution).

Finally, we tested the effect of treatment with PEG10k on the network properties of neurons. For this, we expressed the fluorescent calcium sensor GCamp6f [25] in cultured primary hippocampal neurons using adeno-associated virus (AAV). We first recorded neural activity for 5 min, incubated with culture media (control) or culture media containing 60mg/ml PEG10k for 1hr, and then recorded neural activity again for 5 min. Representative raster plots of the activity of neurons in culture before and after PEG10k treatment can be found in Fig. 4A and 4B respectively. Pairwise synchronization matrices [26] calculated from these plots can be found in Fig. 4C and 4D. Global Synchronization of neural activity increased after 1 hour treatment with PEG10K, in contrast to a decrease in global synchronization observed in control cultures (Fig. 4E, p = 0.014233, 2-tailed heteroscedastic T-test, n=3 cultures incubated with PEG10k, n=5 control cultures).

The increase in network synchronization precludes PEG10k from applications in functional neural imaging. To circumvent this, we considered Dextran, another biocompatible polymer available in a range of molecular weights, that is also used in a wide variety of biological and medical applications [27-30].

Optical Clearing using Dextran

We chose to use Dextran of 40 kilodalton (kDa) molecular weight ("Dextran40k"), since it would only require a concentration of 70 mg/ml, or 1.75 mM, to achieve an extracellular space refractive index increase of 0.01. As before, we imaged 15μm-diameter (i.e., approximately neural cell body sized) red fluorescent (i.e. 645 nm emission) beads through mouse somatosensory cortex acute brain slices (250 μm thick) placed in an imaging chamber filled with artificial cerebrospinal fluid (aCSF) (Fig. 5A). We incubated slices for 1 hour in aCSF containing 70 mg/mL Dextran40k, then washed them with regular aCSF, and imaged the beads through the slice again, in regular aCSF (Fig. 5B). This process increased the intensity of the signal from the beads (after background subtraction) by an average of +477.9% (Fig. 5C; 20th percentile +281.5%, median +406.7%, mean +477.9%, 80th percentile +783.5%, Cohen's d 2.2816, n =67, 63 beads for pre- vs. treatment, respectively, from 5 slices, obtained from 3 mice). This change was significant ($p = 1.239*10^{-20}$, two-sample Kolmogorov-Smirnov test), and significantly different from the minor changes (p = 0.0201, two-sample Kolmogorov-Smirnov test, n = 51 beads before, 46 after incubation, from 5 slices from 2 mice) observed with 1 hour incubation in regular aCSF (p = 0.0038, two-sample Kolmogorov-Smirnov test, n = 5 slices from 4 mice for Dextran40k-containing aCSF vs. n = 5 slices from 2 mice for regular aCSF).

We next sought to determine whether 1.75mM Dextran40k altered normal neurophysiology. We performed whole-cell patch clamp recording of cultured primary mouse hippocampal neurons pre-incubated for 1 hour in culture media supplemented with 70 mg/ml Dextran40k and recorded neurons while immersed in Tyrode's solution supplemented with 70 mg/ml Dextran40k (incubated for up to one hour), comparing to recordings of cells from the same culture kept in regular Tyrode's solution. The resultant traces (e.g., in response to current injections of -100 to 250 pA in 50 pA steps) were similar, with no differences in resting membrane potential (Fig. 6A), input resistance (Fig. 6B), membrane capacitance (Fig. 6C), membrane time constant (Fig. 6D), spike threshold (Fig. 6E), or spike width (Fig. 6F), between the Dextran40k vs. control cases (p = 0.990348179, 0.1719, 0.14644, 0.89535, 0.54258, and 0.82249 respectively, two-sample Kolmogorov-Smirnov test, n = 47 neurons from two cultures incubated in Dextran40K-containing Tyrode's solution, n = 42 neurons from the same two cultures incubated in control Tyrode's solution).

We also tested the effect of treatment with Dextran40k on the network properties of neurons. We expressed the fluorescent calcium sensor GCamp6f in cultured primary hippocampal neurons using adeno-associated virus (AAV). We first recorded neural activity for 10 min, incubated with culture media (control) or culture media containing 70mg/ml Dextran40k, and then recorded neural activity again for 10 min. Representative raster plots of the activity of neurons in culture before and after Dextran40k treatment can be found in Fig. 7A and 7B respectively. Pairwise synchronization matrices calculated from these plots can be found in Fig. 7C and 7D. Like the control cultures, global synchronization of neural activity was found to decrease In cultures treated with Dextran40k for 1 hour (Fig. 7E, p = 0.637151, 2-tailed heteroscedastic T-test, n=5 cultures incubated with Dextran40k, n=5 control cultures).

We next explored in vivo optical clearing of the live mouse brain with Dextran40k. For this, we imaged the cortical surface of anaesthetized transgenic Pvalb-tdTomato reporter mice [31] under normal lactated Ringer's solution. We then superfused onto the cortical surface, for 1 hour, aCSF containing either 1.75 mM Dextran40k, or 1.75 mM sucrose as a control, washing the surface with lactated Ringer's solution at the end. Representative optical slices taken via one-photon epifluorescent imaging at progressively greater depths pre- (top) vs. post- (bottom) Dextran-containing aCSF superfusion are shown in Fig. 8A-8C. Cells appear brighter, and in greater numbers, after optical clearing. Quantitatively, the intensity of cells (after background subtraction) increased by an average of +118.1% after optical clearing vs. beforehand (Fig. 5D, orange; 20th percentile +48.1%, median +111.1%, mean +118.1%, 80th percentile +186.9%, $p = 5.697*10^{-18}$, two-sided Wilcoxon signed rank test, Cohen's d 0.6217, n = 100 cells from 2 mice), which was not observed when we superfused the brain with aCSF with sucrose (Fig. 8D, blue; n = 122 cells from 2 mice); the effects of adding Dextran40k vs. sucrose were highly significantly different ($p = 5.4920*10^{-61}$, two-sample Kolmogorov-Smirnov test). Importantly the increase in cellular intensity increased with depth (Fig. 8E).

Optical Clearing using Silicon nanoparticles

While polymers represent a simple strategy for raising the refractive index of extracellular space, their relatively low refractive index limits the degree of refractive index matching that can be achieved without affecting neural physiology and communication. Neural physiology and communication is known to be affected by the increase in osmolality [9-15], viscosity [32-35] and macromolecular crowding [36,37] caused by higher polymer concentrations.

Semiconductor nanoparticles offer a promising alternative, because of the much higher refractive index (Si: $n = 3.97$, Ge: $n = 5.69$) compared to polymers (Dextran: $n \sim 1.42$, PEG: $n \sim 1.66$), and thus the much lower concentration needed for the same level of refractive index matching (See Chapter 1, Fig. 1). Semiconductors, such as silicon, have been shown to be highly biocompatible [38-49], and surface functionalization can be employed to tailor nanoparticles-cells interactions. For example, PEGylation has been shown to reduce protein absorption and cellular uptake [19,50].

We first tested the uptake of these PEGylated Si nanoparticles (PEG-SiNPs) by neurons. For this, we incubated cultured primary hippocampal neurons with culture media supplemented with 4 mg/ml, or 0.16 mM, PEG-SiNPs for 1 hour. This concentration of PEG-SiNPs was sufficient to increase the refractive index of culture media by 0.01. Neurons were then washed thrice with Tyrode's solution and then imaged in Tyrode's solution. Note that, PEG-SiNPs have characteristic photoluminescence [51] and could be detected directly by fluorescence microscopy. We observed that PEG-SiNPs did not adsorb onto neural cell membranes and were not internalized by neurons (see Fig. 9). This suggests that PEG-SiNPs would likely remain sequestered and consequently increase the refractive index of the extracellular space in brain tissue.

We then administered these PEG- SiNPs to acute brain slices, repeating the test employed earlier, and found increased transparency when we compared pre- vs. post-incubation images (Figs. 10A,

Fig. 10B). We observed a +301% increase in intensity of the signal from the beads (background subtracted) imaged through the tissue sections (Fig. 10C; 20th percentile +111%, median +171.9%, mean +300.7%, 80th percentile +580.7%, Cohen's d 0.6176, n = 40, 69 beads for baseline and after optical clearing, respectively, from 3 slices, obtained from 2 mice). This change was significant ($p = 5.2458*10^{-8}$, two-sample Kolmogorov-Smirnov test), and significantly different from the changes observed with 1hr incubation in regular aCSF (p = 0.0145, two-sample Kolmogorov-Smirnov test, n = 3 slices from 2 mice for Si NP-aCSF, n = 5 slices from 2 mice for regular aCSF).

In contrast to the PEG10k and Dextran40k, some neurophysiological parameters were changed (see Fig. 11) when primary hippocampal neurons were bathed in Tyrode's solution supplemented with PEG-SiNPs. We found that the resting membrane potential (Fig. 11A), input resistance (Fig. 11B), and spike width (Fig. 11F) changed significantly, while membrane capacitance (Fig. 11C), membrane time constant (Fig. 11D), and spike threshold (Fig. 11E) did not (p = 0.043702, 0.0010977, 0.00095703, 0.073285, 0.94283, 0.080183 respectively, two-sample Kolmogorov-Smirnov test, n = 68 control neurons from 7 cultures, n = 30 neurons from 3 cultures incubated and patched in Tyrode's solution containing 0.16 mM PEG-SiNPs).

This suggests that while the principle of optical clearing of live tissues generalizes across multiple high refractive index materials, further engineering may be required for specific reagents to be sufficiently biocompatible, given the delicate nature of neurons.

Discussion

Although robust tissues such as skin [52-54] and bone [55,56] have been made more optically transparent while alive by strong chemical treatments, the harsh methods employed would not support the delicate physiology that must be operational for normal brain function. We here demonstrated that Dextran 40k was able to improve the transparency of the living mouse brain without discernable changes in neural electrophysiological and network properties. Going forward, the use of even higher molecular weight reagents might be helpful; any slower diffusion might be compensated for by convection-enhanced delivery or other methods [57-60].

Nanoparticles-based clearing agents appear particularly promising in this regard, since the high refractive index of semiconductors allows, in principle, perfect refractive index matching, and hence complete transparency, at a small volume fill fraction (e.g. <1% (v/v) for Ge nanoparticles). While nanoparticles have been used for decades in biological and biomedical applications, e.g. as fluorescent tags, sensors, drug carriers, etc., this is the first demonstration, to our knowledge, of their use to engineer the optical properties of living organisms. We demonstrate a decrease in optical scattering of live brain tissue with PEG-ylated silicon nanoparticles. However, further engineering will be necessary for these silicon nanoparticles to be sufficiently biocompatible, given the delicate nature of neurons.

In order to achieve maximal transparency it will be necessary to also deliver the agent intracellularly, to refractive index match organelles' membranes and the cytosol, where the majority of scattering is expected to occur in living tissue [61,62]. A number of strategies could be employed, such as delivery of such chemicals by fusogenic liposomes [63], appropriate surface functionalization of the nanoparticles [64,65], or use of nonpolar molecules that can diffuse through the cellular membrane [66-68]. If genetically encoded, expression of a gene or set of genes would be sufficient. Since the clearing agent would be present within the cell, rather than being confined to the extracellular space, it will be particularly important to fully characterize the safety of the reagents and any effect they might have on native physiology. Of course, we cannot rule out that some of the effect observed might already be due to these molecules entering the cytosol of brain cells, and refractive index matching the cytosol to the membranes of organelles and the plasma membrane.

We anticipate that this work will not only represent a starting point for ever more efficacious clearing agents that might approach the theoretical limits, allowing imaging deep into the tissue for a variety of biomedical applications, but will more generally spur the development of biological/nanotechnology hybrid systems with desirable optical properties.

In the following two chapters, we report two tools that may be leveraged towards this. (1) In the next chapter, we describe a method for the synthesis of high-yield and high-monodispersity nanoparticles of a variety of materials with tailored surface ligands, using common benchtop equipment. This method will be useful for developing nanoparticles with better biosafety, efficacy and performance. (2) In the final chapter of this thesis, we describe a method for the delivery of hydrophobic NVNDs to neural cell membranes using PEG-ylated liposomes. These PEG-ylated liposomes may be used for delivery of hydrophyllic nanoparticles to neural soma and achieve maximal transparency.

Materials and Methods

All procedures involving animals were in accordance with the US National Institutes of Health Guide for the Care and Use of Laboratory Animals and approved by the Massachusetts Institute of Technology (MIT) Committee on Animal Care.

Refractive index measurements. All refractive indeces were measured with a Reichert 1310488M Abbe Refractometer (Cole-Parmer).

Slice preparation for bead assays. C57BL/6 mice were deeply anesthetized with a ketamine/xylazine cocktail, then transcardially perfused with ice-cold solution containing, in mM, 252 sucrose, 3 KCl, 1.25 NaH_2PO_4*$2H_2O$, 2 $MgSO_4$, 2 $CaCl_2$*$2H_2O$, 10 glucose, and 24 $NaHCO_3$, and saturated with 95% oxygen and 5% carbon dioxide. The brain was then extracted and slices 200 (for Si nanoparticle testing) or 250 (for PEG and Dextran testing) µm thick were cut on a vibratome (Leica Biosystems). The slices were then allowed to recover for at least 30' in an interface holding chamber (Harvard Apparatus), in aCSF containing, in mM, 126 NaCl, 3 KCl, 1.25 NaH_2PO_4*$2H_2O$, 2 $MgSO_4$, 2 CaCl2*$2H_2O$, 10 glucose, and 24 $NaHCO_3$, and saturated with 95% oxygen and 5% carbon dioxide. Optical clearing solutions were similar to recording aCSF, with the addition of either 60 mg/ml PEG10KDa, 70mg/ml Dextran40KDa or 4mg/ml PEG-SiNPs. All chemicals, other than the PEG-SiNPs, were obtained from Sigma-Aldrich.

Bead assay. Acute brain slices, prepared as described above, were placed in a sealed imaging chamber (VWR) filled with plain aCSF. An array of red (emission, 645 nm) fluorescent 15 µm polystyrene beads (Invitrogen) was then imaged through the slice on an inverted epifluorescence microscope. The slices were then transferred to an incubation chamber containing the clearing solution (e.g. PEG-containing aCSF), which was constantly bubbled with 95% oxygen, 5% carbon dioxide. After one hour the slices were removed from the incubation chamber, rinsed once with plain aCSF, then placed in the sealed imaging chamber, filled with plain aCSF. We then imaged the beads through the slice again, using the same exposure and light intensity settings as before clearing. Data was analyzed using Fiji [69,70].

In vitro whole-cell patch clamping. Whole-cell patch-clamp recordings were made using an Axopatch 200B amplifier, a Digidata 1440 digitizer, and a PC running pClamp10.4 (Molecular Devices). For current clamp recordings, neurons were patched at 18-21 days in vitro (DIV) to allow for sodium channel maturation. Neurons were bathed in room-temperature Tyrode's solution containing, in mM, 129 NaCl, 2 KCl, 3 $CaCl_2$, 1 $MgCl_2$, 25 HEPES, 30 glucose, 0.01 NBQX, 0.01 GABAzine and pH adjusted to 7.3 with NaOH or in Tyrode's solution supplemented with 60mg/ml PEG 10KDa (PEG-Tyrode), 70mg/ml Dextran 40KDa (Dextran-Tyrode) or 4mg/ml PEG-SiNP (SiNP-Tyrode). Neurons were bathed in these solutions for at least 15 minutes prior to whole-cell patch clamping. Borosilicate glass pipettes (Warner Instruments) with an outer diameter of 1.2 mm and a wall thickness of 0.255 mm were pulled to a resistance of 5–9 MΩ with a P-97 Flaming/Brown micropipette puller (Sutter Instruments) and filled with a solution containing, in mM, 150 K-gluconate, 8 NaCl, 0.1 $CaCl_2$, 0.6 $MgCl_2$, 1 EGTA, 10 HEPES, 4 Mg-ATP, 0.4 Na-GTP, with pH adjusted to 7.3 with KOH, and osmolarity adjusted to 298 mOsm with sucrose. We used cells with access resistance 5-30 MΩ and holding current within ±50 pA (at −65 mV, in voltage clamp). Access resistance was monitored throughout recording. Data were analyzed using Clampfit (Molecular Devices) and custom MATLAB scripts (MathWorks).

Primary neuron culture. Hippocampal neurons were prepared from postnatal day 0 or 1 Swiss Webster (Taconic) mice as previously described [71] but with the following modifications: dissected hippocampal tissue was digested with 50 units of papain (Worthington Biochem) for 8 min, and the digestion was stopped with ovomucoid trypsin inhibitor (Worthington Biochem). Cells were plated at a density of 16,000–40,000 per glass coverslip coated with Matrigel (BD Biosciences). Neurons were seeded in 90 or 100ul Plating Medium containing MEM(Life Technologies), glucose (33mM, Sigma), transferrin(0.01%, Sigma), HEPES (10mM, Sigma), GlutaGRO (2mM, Corning), Insulin (0.13%, Millipore), B27 supplement (2%, Gibco), heat inactivated fetal bovine serum (7.5%, Corning). After cell adhesion, additional Plating Medium was added. AraC (0.002mM, Sigma) was added when glia density was 50-70%. Neurons were grown at 37°C degree and 5% CO2 in a humidified atmosphere.

Virus injection. In order to express iRFP682 [24] in a sparse subset of neurons we injected a mixture of dilute (1:500) AAV2/8-CAG-Cre and AAV2/8-FLEX-iRFP682 in C57BL/6 mice. Under sterile conditions, a small craniotomy was performed, and the viruses were injected at a site -1.5 mm posterior to bregma and 1.5 mm lateral from bregma at a depth of 0.15-0.2 mm. We then allowed at least 4 weeks for the protein to be expressed.

In vivo imaging. On the day of the experiment, with the animal under isoflurane anesthesia (1-2% in O2), a metal headplate was secured to the skull using dental cement. A craniotomy was then performed at the site of the viral injection, followed by a durotomy. The animal, still kept under isoflurane anesthesia, was then transferred to the custom-built one-photon microscope. For iRFP imaging we used 625nm excitation, with a 664 long pass emission filter (Thorlabs). The headplate holder was secured on a platform mounted on a 3-axis stage, which could be controlled through Micromanager to acquire image stacks. After a baseline stack was taken, with the brain covered with lactated Ringer's solution, the solution of interest was superfused onto the brain. It was removed and replaced with fresh solution every 20 min to minimize the effects of evaporation. At the end of the hour the solution was removed, the surface rinsed once with lactated Ringer's solution, then fresh lactated Ringer's solution was applied and a new image stack was taken. The composition of the HEPES-aCSF was, in mM: 135 NaCl, 5 KCl, 5 HEPES, 1.8 $CaCl_2*2H_2O$, 1 $MgCl_2*6H_2O$. PEG-HEPES_aCSF contained, in addition, 60 mg/ml PEG10KDa, whereas sucrose-HEPES-aCSF contained, instead of PEG10KDa, 6 mM sucrose, as an osmotically matched control.

In vivo imaging data analysis. We first performed background subtraction on the raw image stacks using Fiji [42–44], using a 20 pixel radius. That gave a better estimate of the difference in signal intensity between background and cells compared to measuring the raw intensities, but didn't completely eliminate the background, which in some cases had intensities on the order of up to 80% of the signal from the fainter cells. To account for that we measured the mean intensities of 5 patches of the image devoid of neurons but near neurons, at different focal planes, averaged them, and subtracted that value from the intensity values measured at the neurons. As an intensity measure for the neurons we took the peak mean intensity measured for the entire cell across the z-stack. This allowed us to have a good estimate of the change in fluorescence between the cells and the background. Repeating the procedure for estimating background multiple times using different selections gave values within < 10% of each other. All analysis was performed blind to condition.

Reagents and materials for SiNP synthesis and functionalization. Hydrogen silsesquioxane (HSQ, trade name Fox-17) was purchased from Dow Corning and the solvent was removed to yield a white solid that was used directly. Hydrofluoric acid (48–50%) was purchased from Fisher Scientific and used as received. Methyl-10-undecenoate (96%), was purchased from Sigma-Aldrich and used as received. Allyloxy (polyethylene oxide) (35-50 EO, 1500 – 2000 g/mol) was purchased from Gelest Incorporation and heated at 50 °C under Schlenk line vacuum at 0.2 Torr for 48 hours to remove the moisture. All solvents were reagent grade and used as received. Toluene was collected from a Pure-Solv purification system immediately prior to use. All other solvents were reagent grade and Milli-Q water was used throughout the experiment. Amicon Ultra-15 Centrifugal Filter Unit (30K MWCO) was purchased from Sigma Aldrich. Hydrophilic nylon filters (0.20 μm) were purchased from Fischer Scientific.

Synthesis of hydride-terminated silicon nanocrystals (H-SiNCs). H-SiNCs were prepared using a well-established literature procedure [72]. Briefly, SiNC/SiO_2 composite obtained from reductive thermal processing of HSQ at 1100° C was etched using ethanolic HF. Following extraction from HF into toluene, the H-SiNCs were isolated by centrifugation at 3000 rpm. The orange/yellow solid redispersed in toluene and activated molecular sieves S4 (4 Å) were added. The suspension was mixed thoroughly using a glass pipet to remove residual moisture and then transferred to another test tube and isolated by centrifugation at 3000 rpm for 5 min (2×).

Thermal hydrosilylation of H-SiNCs with mixed ligands. H-SiNCs were dispersed in 8 mL (ca. 34 mmol) of methyl 10-undecenoate and transferred to a dry Schlenk flask equipped with a magnetic stirrer bar and charged with argon. Subsequently, 3 g (ca. 2.3 mmol) allyloxy (polyethylene oxide) was added. The mixture was subjected to three freeze–pump–thaw cycles using an Ar charged double manifold Schlenk line. After warming to room temperature, the Schlenk flask was transferred to a silicone oil bath pre-heated to 180 °C and stirred for 24 h under Ar. The reaction mixture became transparent within 30 min. After that, the nanocrystals were washed by solvent/antisolvent method. In the first five cycles, chloroform/hexane were used and then ethanol/hexane were used to wash these NCs five times at 5000 RPM.

Figures:

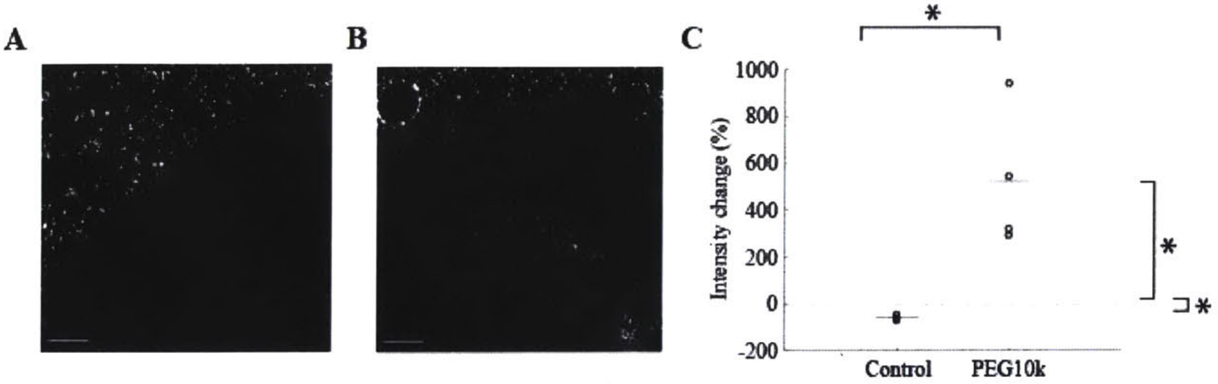

Figure 1. Optical transparency of live mouse brain slices increases after high molecular weight PEG administration. (A, B) Red fluorescent microbeads imaged through a 250 µm- thick acute brain slice before (A) vs. after (B) 1hr incubation in aCSF containing 60 mg/mL PEG of 10kD molecular weight ("PEG10k"). In both (A) and (B) scale bars are 500 µm long. (C) Change in background-subtracted intensity of the signal recorded from beads imaged through the tissue section, for regular aCSF ("Control") vs. PEG-containing aCSF ("PEG10k"). Each circle represents a slice; horizontal lines indicate means; dashed line indicates 0 (no change). * indicates $p < 0.05$ (see main text for full statistics).

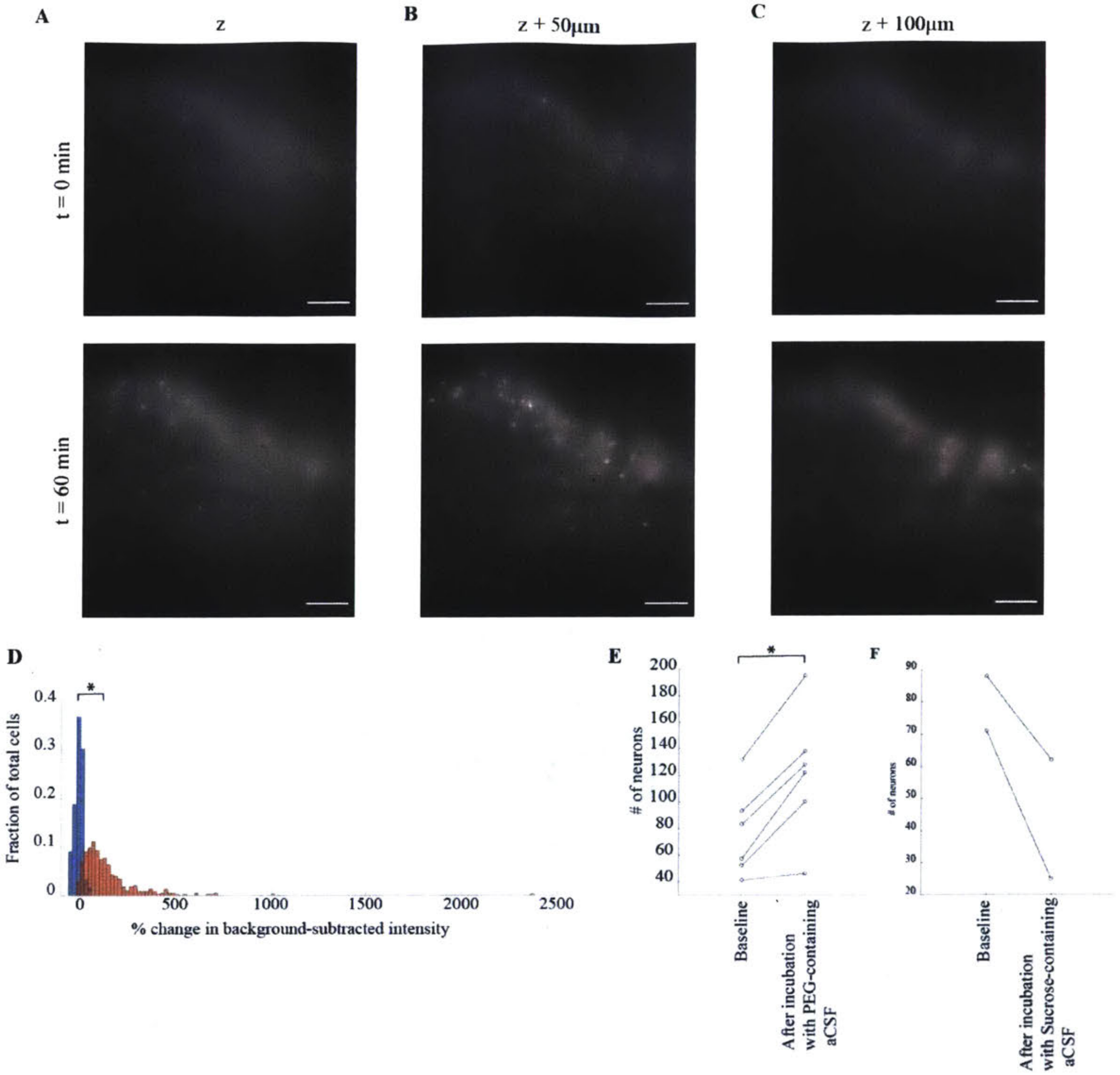

Figure 2. Increasing the optical transparency of live mouse brain via high molecular weight PEG administration. (A-C) Optical slices taken from progressively greater depths within the mouse somatosensory cortex, before (top) and after (bottom) 1 hour superfusion with PEG-containing aCSF. Scale bars are 50 μm long. (D) Histogram showing the percentage change over baseline of background-subtracted cell fluorescent intensity after 1hr superfusion with aCSF containing sucrose (blue) vs. PEG-containing aCSF (orange). *, $p<0.05$ (see main text for full statistics). (E) Number of cells visible in the background-subtracted maximum-intensity projections, before vs. after PEG-containing aCSF administration *, $p<0.05$ (see main text for full statistics). (F) As in E, but before vs. after sucrose-containing aCSF administration.

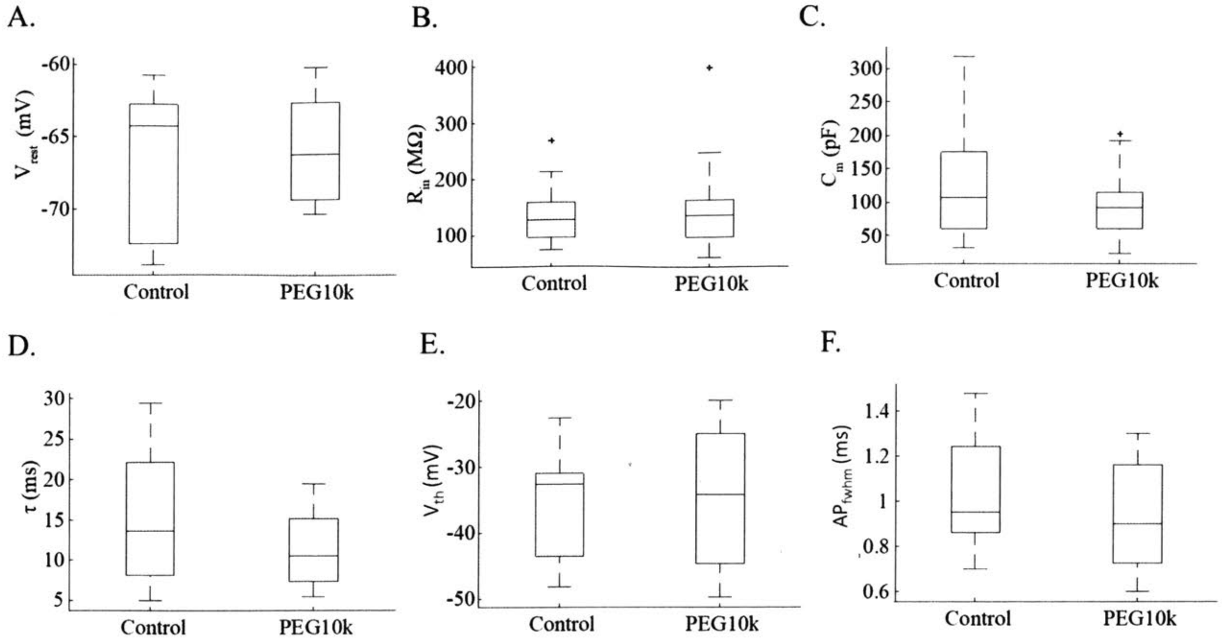

Figure3. Electrophysiological properties of control neurons and neurons incubated and recorded in Tyrode's solution containing 60mg/ml PEG10k. $p > 0.05$ for all parameters (see main text for full statistics, $n = 15$ neurons from one culture incubated in PEG-containing Tyrode's solution, $n = 17$ neurons from the same culture incubated in control Tyrode's solution). Shown are box plots: on each box, the central mark indicates the median, and the bottom and top edges of the box indicate the 25th and 75th percentiles, respectively. The whiskers extend to the most extreme data points not considered outliers, and the outliers are plotted individually using the '+' symbol. (A) Resting membrane potential. (B) Input resistance. (C) Membrane capacitance. (D) Membrane time constant. (E) Spike threshold. (F) Spike width.

s

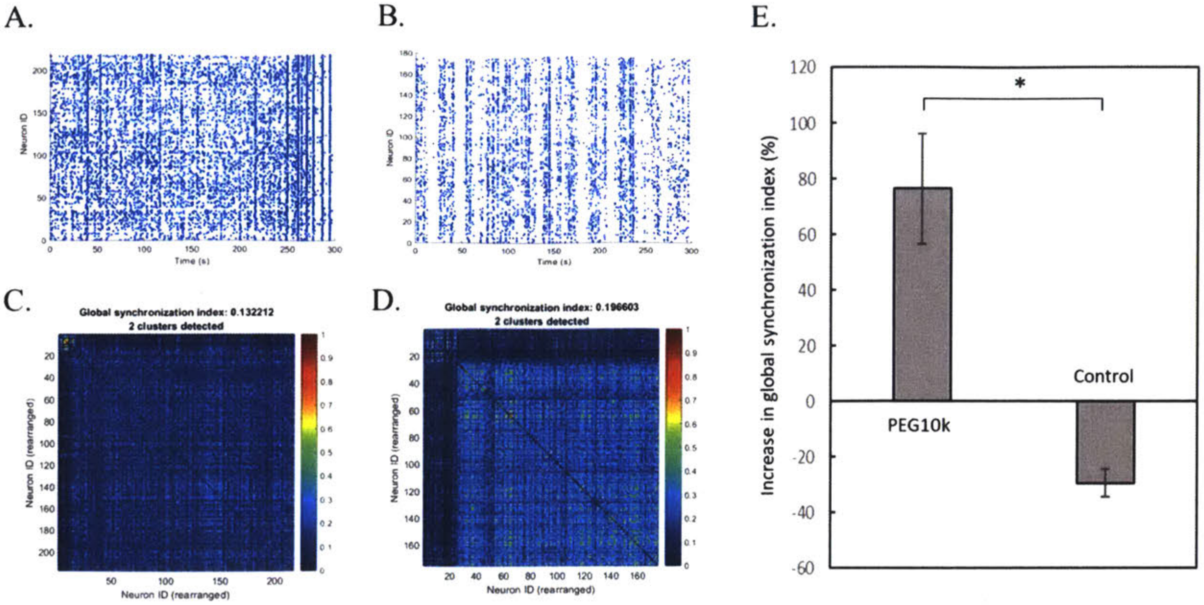

Figure 4. Network activity of cultured primary hippocampal neurons is affected by treatment with culture media containing 60mg/ml PEG10k (A, B) Spontaneous activity patterns of neurons before (A) and after (B) treatment with PEG10k show increased synchronization of neural activity. (C, D) Pairwise synchronization of individual neurons before (C) and after (D) treatment with PEG10k shows increased global synchronization of neural activity (E) Percentage Increase in global synchronization index after 1 hour incubation with PEG10k, and control * indicates $p < 0.05$ (see main text for full statistics), n=3 cultures treated with PEG10k, n=5 control cultures.

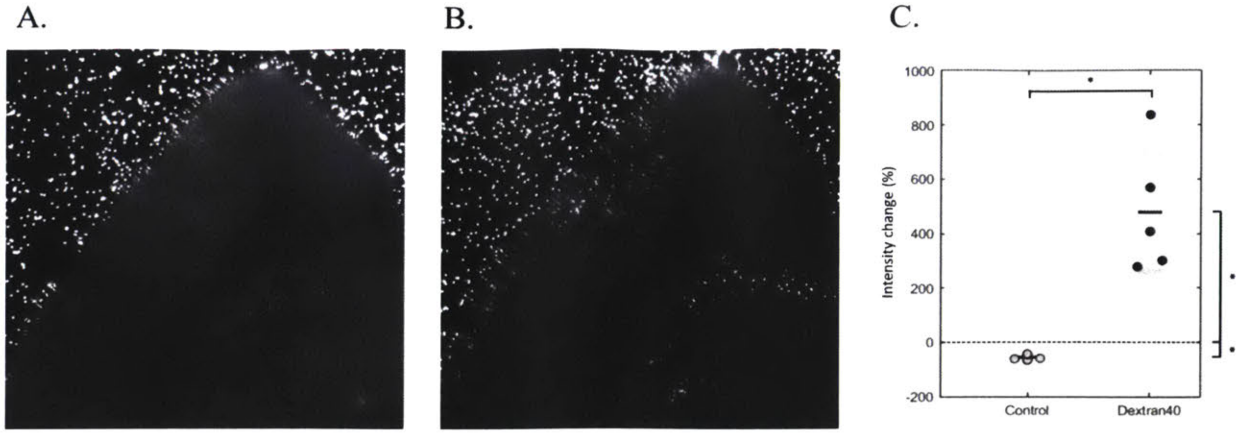

Figure 5. Optical transparency of live mouse brain slices increases after high molecular weight Dextran administration. (A, B) Red fluorescent microbeads imaged through a 250 µm- thick acute brain slice before (A) vs. after (B) 1hr incubation in aCSF containing 70 mg/mL Dextran of 40kD molecular weight ("Dextran50k"). In both (A) and (B) scale bars are 500 µm long. (C) Change in background-subtracted intensity of the signal recorded from beads imaged through the tissue section, for regular aCSF ("Control") vs. Dextran-containing aCSF ("Dextran40k"). Each circle represents a slice; horizontal lines indicate means; dashed line indicates 0 (no change). * indicates $p < 0.05$ (see main text for full statistics).

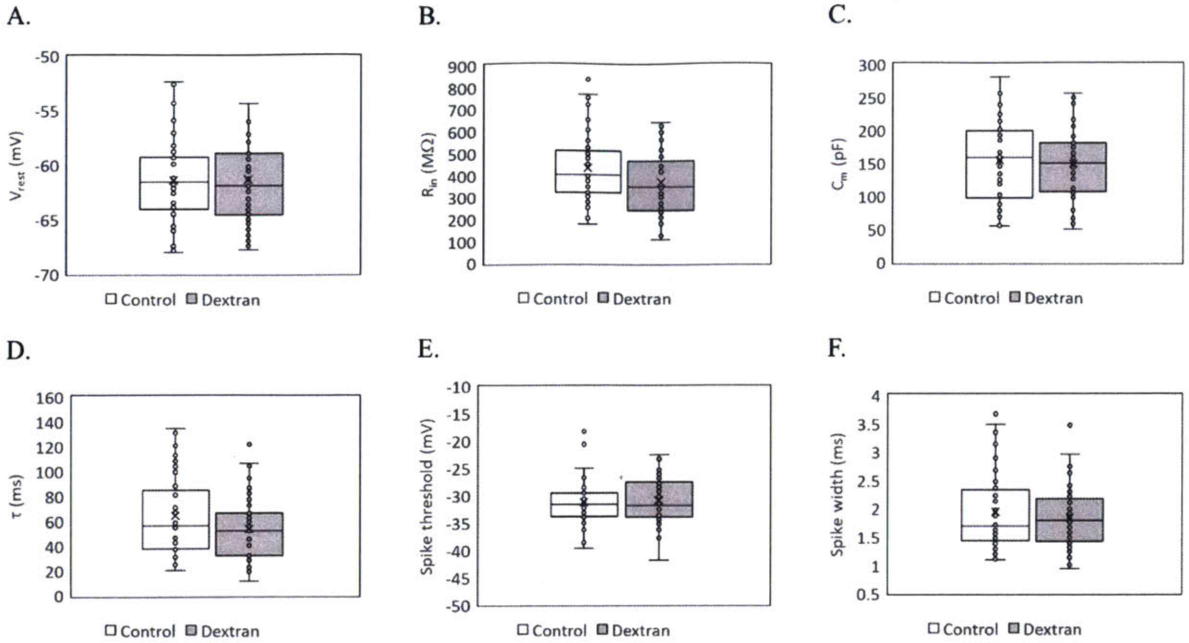

Figure 6. Electrophysiological properties of control neurons and neurons incubated in culture media containing 70mg/ml Dextran 40k, and recorded in Tyrode's solution containing 70mg/ml Dextran40k. $p > 0.05$ for all parameters (see main text for full statistics, $n = 47$ neurons from one culture incubated in Dextran-containing Tyrode's solution, $n = 42$ neurons from the same culture incubated in control Tyrode's solution). Shown are box plots: on each box, the central mark indicates the median, and the bottom and top edges of the box indicate the 25th and 75th percentiles, respectively. The whiskers extend to the most extreme data points not considered outliers, and the outliers are plotted individually using the 'o' symbol. (A) Resting membrane potential. (B) Input resistance. (C) Membrane capacitance. (D) Membrane time constant. (E) Spike threshold. (F) Spike width.

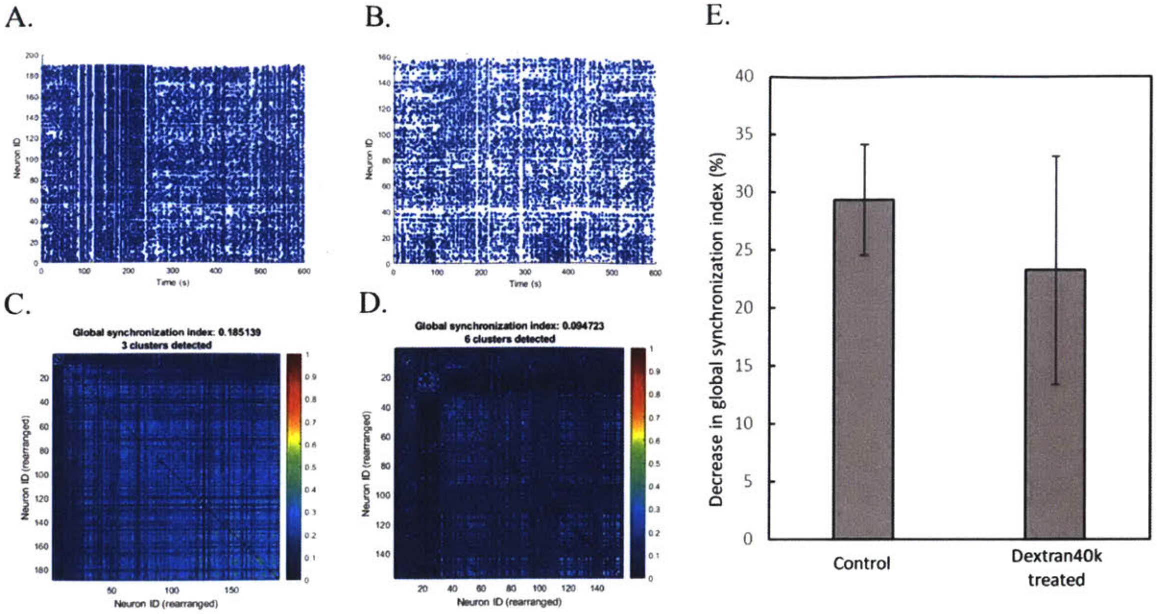

Figure 7. Network activity of cultured primary hippocampal neurons is not affected by treatment with culture media containing 70mg/ml Dextran40k (A, B) Spontaneous activity patterns of neurons before (A) and after (B) treatment with Dextran40k show decreased synchronization of neural activity. (C, D) Pairwise synchronization of individual neurons before (C) and after (D) treatment with PEG10k shows decreased global synchronization of neural activity (E) Percentage decrease in global synchronization index after 1 hour incubation with Dextran40k, and control are comparable. $p > 0.05$ (see main text for full statistics), n=5 cultures treated with Dextran40k, n=5 control cultures.

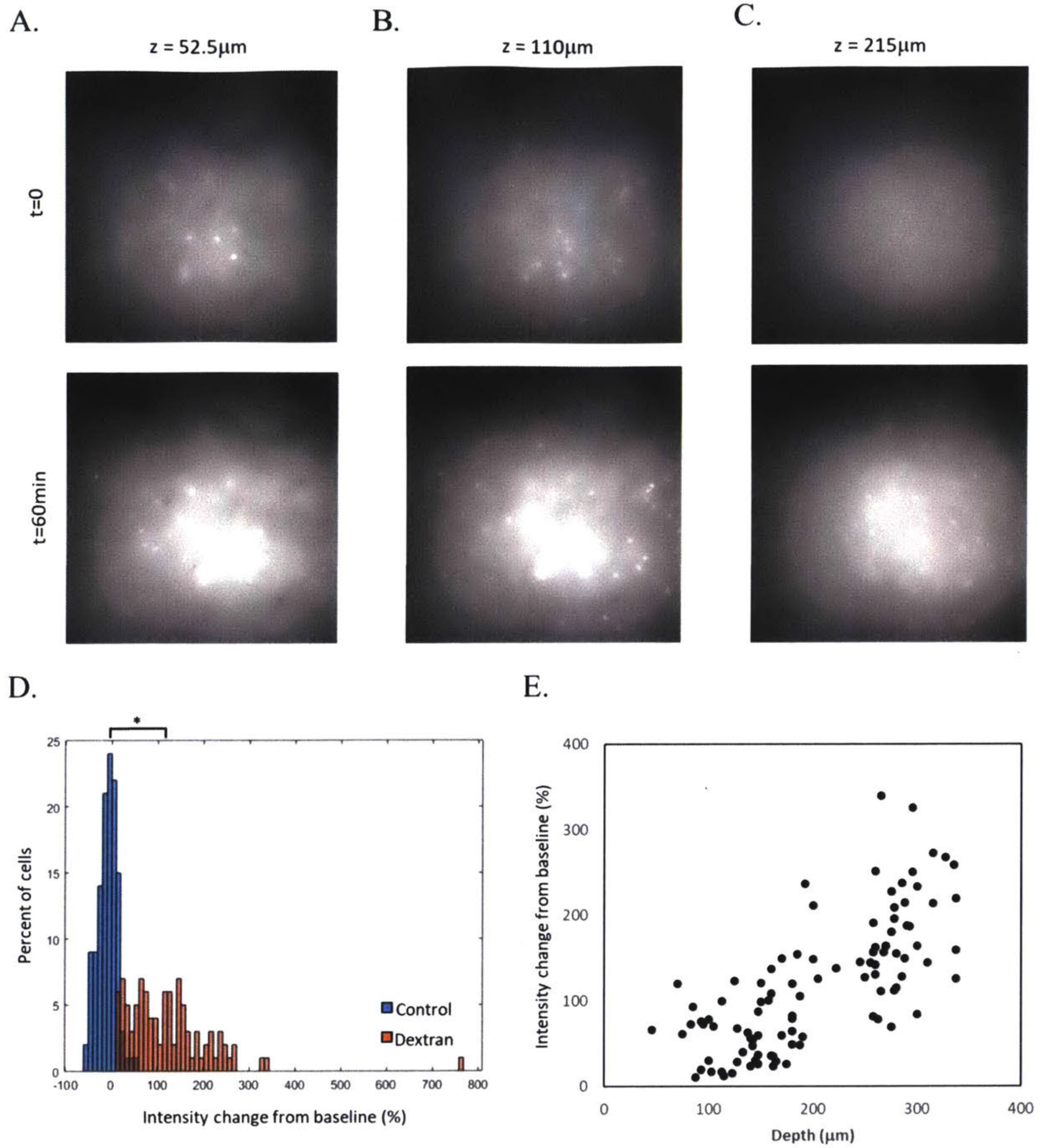

Figure 8. Increasing the optical transparency of live mouse brain via high molecular weight Dextran administration. (A-C) Optical slices taken from progressively greater depths within the mouse somatosensory cortex, before (top) and after (bottom) 1 hour superfusion with Dextran-containing aCSF. (D) Histogram showing the percentage change over baseline of background-subtracted cell fluorescent intensity after 1hr superfusion with aCSF containing sucrose (blue) vs. Dextran-containing aCSF (orange). *, $p < 0.05$ (see main text for full statistics). (E) Scatter plot showing the percentage change over baseline of background subtracted intensity at various depths after 1h superfusion with Dextran-containing aCSF.

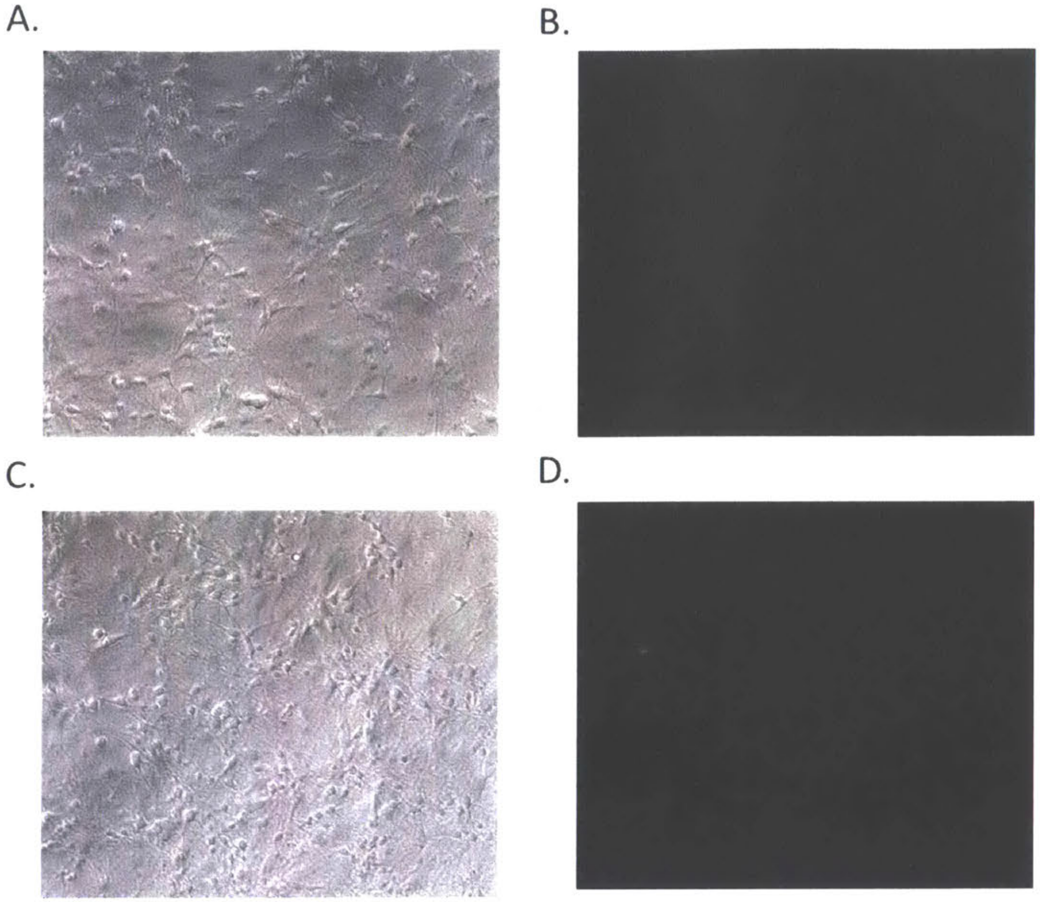

Figure 9. PEG-ylated Silicon Nanoparticles do not adsorb onto primary hippocampal neurons in culture. (A,C) brightfield images of cultured primary hippocampal neurons before (A) and after (C) incubation with PEG-ylated silicon nanoparticles. (B,D) fluorescence images (Ex 390nm, Em 560LP) of cultured primary hippocampal neurons before (B) and after (D) incubation with PEG-ylated silicon nanoparticles. Note that there is no increase in signal in the images

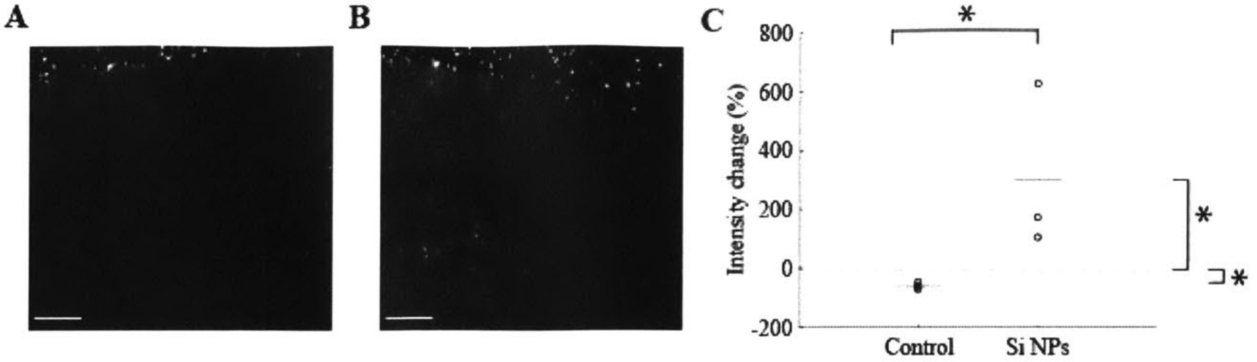

Figure 10. PEG-ylated Silicon nanoparticles can increase the transparency of mouse brain slices at low concentration. (A) 15 μm far red (emission 645 nm) polystyrene beads imaged though a 200μm-thick acute brain slice. (B) Same slice and setup as in (A), after 1hr incubation in Si nanoparticle-containing aCSF. In both (A) and (B) scale bars are 500 μm long. (C) Changes in background-subtracted intensity for beads imaged after 1hr incubation with the conventional vs. Si nanoparticle-containing aCSF. Each circle represents a slice, line segments indicate means, dashed lines indicate 0 (no change). *, $p<0.05$ (see main text for full statistics).

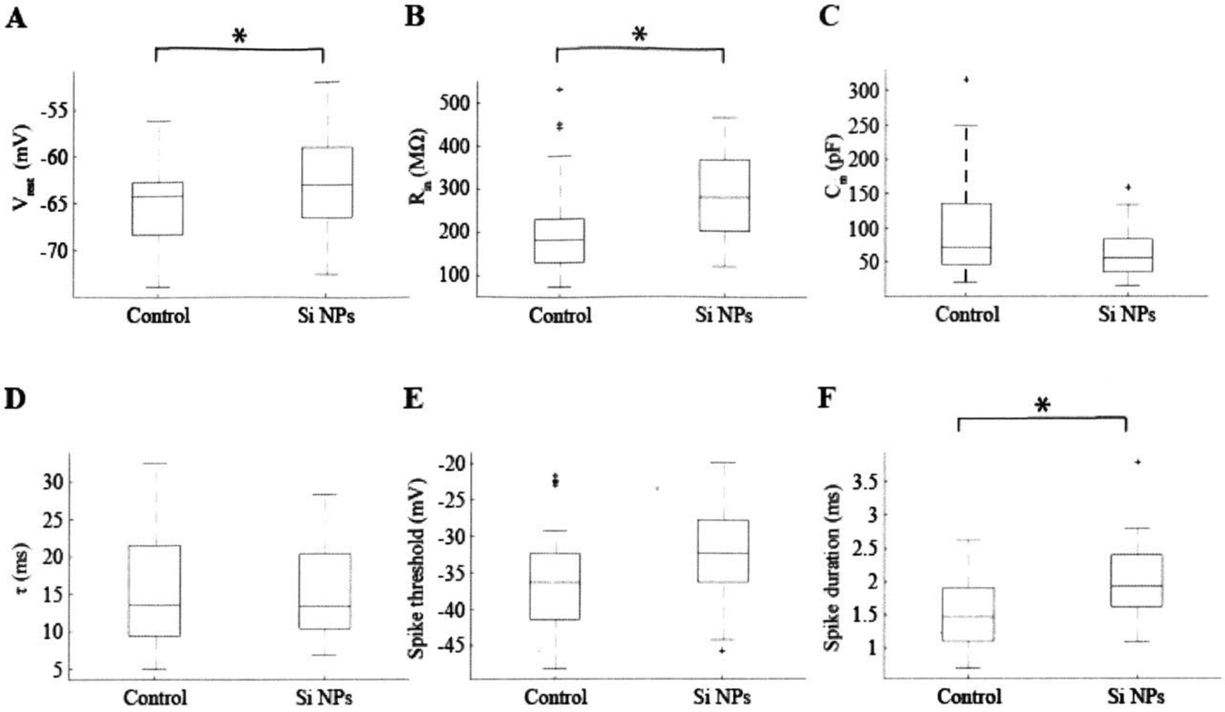

Figure 11. Effects of PEG-ylated Si nanoparticles on neuronal electrophysiological properties. Electrophysiological properties of control neurons and neurons incubated and recorded in in Tyrode's solution containing 4 mg/ml or 0.16 mM PEG-ylated Si nanoparticles inducing a refractive change of 0.01 compared to regular Tyrode's solution. Shown are box plots: on each box, the central mark indicates the median, and the bottom and top edges of the box indicate the 25th and 75th percentiles, respectively. The whiskers extend to the most extreme data points not considered outliers, and the outliers are plotted individually using the '+' symbol. (A) Resting membrane potential. (B) Input resistance. (C) Membrane capacitance. (D) Membrane time constant. (E) Spike threshold. (F) Spike width. p = 0.043702, 0.0010977, 0.073285, 0.94283, 0.080183, 0.00095703 respectively, two-sample Kolmogorov-Smirnov test, n = 68 control neurons from 7 cultures, n = 30 neurons from 3 cultures incubated and patched in Tyrode's solution containing a concentration of Si NPs inducing a refractive index change of 0.01 compared to baseline.

References

1. Renier, N. *et al.* iDISCO: a simple, rapid method to immunolabel large tissue samples for volume imaging. *Cell* 159, 896–910 (2014).
2. Ertürk, A. *et al.* Three-dimensional imaging of solvent-cleared organs using 3DISCO. *Nat. Protoc.* 7, 1983–1995 (2012).
3. Hama, H. *et al.* Scale: a chemical approach for fluorescence imaging and reconstruction of transparent mouse brain. *Nat. Neurosci.* 14, 1481–1488 (2011).
4. Susaki, E. A. *et al.* Whole-brain imaging with single-cell resolution using chemical cocktails and computational analysis. *Cell* 157, 726–739 (2014).
5. Chung, K. & Deisseroth, K. CLARITY for mapping the nervous system. *Nature Methods* 10, 508–513 (2013).
6. Chen, F., Tillberg, P. W. & Boyden, E. S. Expansion microscopy. *Science* 347, 543–548 (2015).
7. Ke, M.-T., Fujimoto, S. & Imai, T. SeeDB: a simple and morphology-preserving optical clearing agent for neuronal circuit reconstruction. *Nat. Neurosci.* 16, 1154–1161 (2013).
8. Levinson, A. THE REFRACTOMETRIC AND VISCOSIMETRIC INDEXES OF CEREBROSPINAL FLUID. *Archives of Internal Medicine* 37, 144 (1926).
9. Ballyk, B. A., Quackenbush, S. J. & Andrew, R. D. Osmotic effects on the CA1 neuronal population in hippocampal slices with special reference to glucose. *J. Neurophysiol.* 65, 1055–1066 (1991).
10. Saly, V. & Andrew, R. D. CA3 neuron excitation and epileptiform discharge are sensitive to osmolality. *J. Neurophysiol.* 69, 2200–2208 (1993).
11. Forsythe, I. D. & Westbrook, G. L. Slow excitatory postsynaptic currents mediated by N-methyl-D-aspartate receptors on cultured mouse central neurones. *J. Physiol.* 396, 515–533 (1988).
12. Huang, R. & Somjen, G. G. The effect of graded hypertonia on interstitial volume, tissue resistance and synaptic transmission in rat hippocampal tissue slices. *Brain Res.* 702, 181–187 (1995).
13. Huang, R. & Somjen, G. G. Effects of hypertonia on voltage-gated ion currents in freshly isolated hippocampal neurons, and on synaptic currents in neurons in hippocampal slices. *Brain Res.* 748, 157–167 (1997).
14. Somjen, G. G. Ion Regulation in the Brain: Implications for Pathophysiology. *The Neuroscientist* 8, 254–267 (2002).
15. Schwartzkroin, P. A., Baraban, S. C. & Hochman, D. W. Osmolarity, ionic flux, and changes in brain excitability. *Epilepsy Res.* 32, 275–285 (1998).
16. Donato, T., Shapira, Y., Artru, A. & Powers, K. Effect of mannitol on cerebrospinal fluid dynamics and brain tissue edema. *Anesth. Analg.* 78, 58–66 (1994).
17. Polderman, K. H., van de Kraats, G., Dixon, J. M., Vandertop, W. P. & Girbes, A. R. J. Increases in spinal fluid osmolarity induced by mannitol. *Crit. Care Med.* 31, 584–590 (2003).
18. Arieff, A. I., Kleeman, C. R., Keushkerian, A. & Bagdoyan, H. Brain tissue osmolality: method of determination and variations in hyper- and hypo-osmolar states. *J. Lab. Clin. Med.* 79, 334–343 (1972).
19. Pelaz, B. *et al.* Surface Functionalization of Nanoparticles with Polyethylene Glycol: Effects on Protein Adsorption and Cellular Uptake. *ACS Nano* 9, 6996–7008 (2015).

20. Zhang, M., Li, X. H., Gong, Y. D., Zhao, N. M. & Zhang, X. F. Properties and biocompatibility of chitosan films modified by blending with PEG. *Biomaterials* **23**, 2641–2648 (2002).
21. Wang, Q., Dong, Z., Du, Y. & Kennedy, J. F. Controlled release of ciprofloxacin hydrochloride from chitosan/polyethylene glycol blend films. *Carbohydrate Polymers* **69**, 336–343 (2007).
22. Alcantar, N. A., Aydil, E. S. & Israelachvili, J. N. Polyethylene glycol-coated biocompatible surfaces. *J. Biomed. Mater. Res.* **51**, 343–351 (2000).
23. Zalipsky, S. Functionalized Poly(ethylene glycols) for Preparation of Biologically Relevant Conjugates. *Bioconjugate Chemistry* **6**, 150–165 (1995).
24. Shcherbakova, D. M. & Verkhusha, V. V. Near-infrared fluorescent proteins for multicolor in vivo imaging. *Nat. Methods* **10**, 751–754 (2013).
25. Chen, T.-W. *et al.* Ultrasensitive fluorescent proteins for imaging neuronal activity. *Nature* **499**, 295–300 (2013).
26. Patel, T. P., Man, K., Firestein, B. L. & Meaney, D. F. Automated quantification of neuronal networks and single-cell calcium dynamics using calcium imaging. *J. Neurosci. Methods* **243**, 26–38 (2015).
27. Shaterabadi, Z., Nabiyouni, G. & Soleymani, M. High impact of in situ dextran coating on biocompatibility, stability and magnetic properties of iron oxide nanoparticles. *Mater. Sci. Eng. C Mater. Biol. Appl.* **75**, 947–956 (2017).
28. Cadée, J. A. *et al.* In vivo biocompatibility of dextran-based hydrogels. *J. Biomed. Mater. Res.* **50**, 397–404 (2000).
29. Constable, P. D., Gohar, H. M., Morin, D. E. & Thurmon, J. C. Use of hypertonic saline-dextran solution to resuscitate hypovolemic calves with diarrhea. *Am. J. Vet. Res.* **57**, 97–104 (1996).
30. Moscovici, M. Present and future medical applications of microbial exopolysaccharides. *Front. Microbiol.* **6**, 1012 (2015).
31. Kaiser, T., Ting, J. T., Monteiro, P. & Feng, G. Transgenic labeling of parvalbumin-expressing neurons with tdTomato. *Neuroscience* **321**, 236–245 (2016).
32. Min, M. Y., Rusakov, D. A. & Kullmann, D. M. Activation of AMPA, kainate, and metabotropic receptors at hippocampal mossy fiber synapses: role of glutamate diffusion. *Neuron* **21**, 561–570 (1998).
33. Kullmann, D. M., Min, M. Y., Asztely, F. & Rusakov, D. A. Extracellular glutamate diffusion determines the occupancy of glutamate receptors at CA1 synapses in the hippocampus. *Philos. Trans. R. Soc. Lond. B Biol. Sci.* **354**, 395–402 (1999).
34. Chalifoux, J. R. & Carter, A. G. Glutamate spillover promotes the generation of NMDA spikes. *J. Neurosci.* **31**, 16435–16446 (2011).
35. Lambe, E. K. & Aghajanian, G. K. Hallucinogen-induced UP states in the brain slice of rat prefrontal cortex: role of glutamate spillover and NR2B-NMDA receptors. *Neuropsychopharmacology* 31, 1682–1689 (2006).
36. Gupta, R., Reneaux, M. & Karmeshu. Role of Heterogeneous Macromolecular Crowding and Geometrical Irregularity at Central Excitatory Synapses in Shaping Synaptic Transmission. *PLoS One* **11**, e0167505 (2016).
37. Renner, M., Choquet, D. & Triller, A. Control of the postsynaptic membrane viscosity. *J. Neurosci.* **29**, 2926–2937 (2009).
38. Park, J.-H. *et al.* Biodegradable luminescent porous silicon nanoparticles for in vivo applications. *Nat. Mater.* **8**, 331–336 (2009).

39. Bimbo, L. M. *et al.* Biocompatibility of thermally hydrocarbonized porous silicon nanoparticles and their biodistribution in rats. *ACS Nano* 4, 3023–3032 (2010).
40. Ruizendaal, L. *et al.* Synthesis and cytotoxicity of silicon nanoparticles with covalently attached organic monolayers. *Nanotoxicology* 3, 339–347 (2009).
41. Wang, Q. *et al.* Uptake and toxicity studies of poly-acrylic acid functionalized silicon nanoparticles in cultured mammalian cells. *Adv. Healthc. Mater.* 1, 189–198 (2012).
42. Ivanov, S. *et al.* In Vivo Toxicity of Intravenously Administered Silica and Silicon Nanoparticles. *Materials* 5, 1873–1889 (2012).
43. Tanaka, T. *et al.* In vivo evaluation of safety of nanoporous silicon carriers following single and multiple dose intravenous administrations in mice. *Int. J. Pharm.* **402**, 190–197 (2010).
44. Kang, S.-K. *et al.* Dissolution chemistry and biocompatibility of silicon- and germanium-based semiconductors for transient electronics. *ACS Appl. Mater. Interfaces* 7, 9297–9305 (2015).
45. Erogbogbo, F. *et al.* Biocompatible luminescent silicon quantum dots for imaging of cancer cells. *ACS Nano* 2, 873–878 (2008).
46. Erogbogbo, F. *et al.* Biocompatible magnetofluorescent probes: luminescent silicon quantum dots coupled with superparamagnetic iron(III) oxide. *ACS Nano* 4, 5131–5138 (2010).
47. Bayliss, S. C., Buckberry, L. D., Fletcher, I. & Tobin, M. J. The culture of neurons on silicon. *Sensors and Actuators A: Physical* 74, 139–142 (1999).
48. Hwang, S.-W. *et al.* Dissolution chemistry and biocompatibility of single-crystalline silicon nanomembranes and associated materials for transient electronics. *ACS Nano* 8, 5843–5851 (2014).
49. Karatutlu, A. *et al.* Synthesis and structure of free-standing germanium quantum dots and their application in live cell imaging. *RSC Advances* 5, 20566–20573 (2015).
50. Mei, B. C., Susumu, K., Medintz, I. L. & Mattoussi, H. Polyethylene glycol-based bidentate ligands to enhance quantum dot and gold nanoparticle stability in biological media. *Nat. Protoc.* 4, 412–423 (2009).
51. Sinelnikov, R., Dasog, M., Beamish, J., Meldrum, A. & Veinot, J. G. C. Revisiting an Ongoing Debate: What Role Do Surface Groups Play in Silicon Nanocrystal Photoluminescence? *ACS Photonics* 4, 1920–1929 (2017).
52. Mao, Z., Han, Z., Wen, X., Luo, Q. & Zhu, D. Influence of glycerol with different concentrations on skin optical clearing and morphological changes in vivo. *Photonics and Optoelectronics Meetings (POEM) 2008: Fiber Optic Communication and Sensors* (2008). doi:10.1117/12.823310
53. Wen, X., Mao, Z., Han, Z., Tuchin, V. V. & Zhu, D. In vivo skin optical clearing by glycerol solutions: mechanism. *J. Biophotonics* 3, 44–52 (2010).
54. Tuchin, V. V. *et al.* Optical clearing of skin using flashlamp-induced enhancement of epidermal permeability. *Lasers in Surgery and Medicine* 38, 824–836 (2006).
55. Zhang, Y., Zhang, C., Zhong, X. & Zhu, D. Quantitative evaluation of SOCS-induced optical clearing efficiency of skull. *Quant. Imaging Med. Surg.* 5, 136–142 (2015).
56. Yang, X. *et al.* Skull Optical Clearing Solution for Enhancing Ultrasonic and Photoacoustic Imaging. *IEEE Trans. Med. Imaging* 35, 1903–1906 (2016).
57. Bobo, R. H. *et al.* Convection-enhanced delivery of macromolecules in the brain. *Proc. Natl. Acad. Sci. U. S. A.* 91, 2076–2080 (1994).

58. Faraji, A. H., Jaquins-Gerstl, A. S., Valenta, A. C. & Weber, S. G. Electrokinetic infusions into hydrogels and brain tissue: Control of direction and magnitude of solute delivery. *J. Neurosci. Methods* **311**, 76–82 (2019).
59. Hadjipanayis, C. G. *et al.* EGFRvIII antibody-conjugated iron oxide nanoparticles for magnetic resonance imaging-guided convection-enhanced delivery and targeted therapy of glioblastoma. *Cancer Res.* **70**, 6303–6312 (2010).
60. Vogelbaum, M. A. & Aghi, M. K. Convection-enhanced delivery for the treatment of glioblastoma. *Neuro-Oncology* **17**, ii3–ii8 (2015).
61. Johnsen, S. & Widder, E. A. The physical basis of transparency in biological tissue: ultrastructure and the minimization of light scattering. *J. Theor. Biol.* **199**, 181–198 (1999).
62. Jacques, S. L. Optical properties of biological tissues: a review. *Physics in Medicine and Biology* **58**, R37–R61 (2013).
63. Kunisawa, J. *et al.* Fusogenic liposome delivers encapsulated nanoparticles for cytosolic controlled gene release. *J. Control. Release* **105**, 344–353 (2005).
64. Fröhlich, E. The role of surface charge in cellular uptake and cytotoxicity of medical nanoparticles. *Int. J. Nanomedicine* **7**, 5577–5591 (2012).
65. Verma, A. & Stellacci, F. Effect of Surface Properties on Nanoparticleâ "Cell Interactions. *Small* **6**, 12–21 (2010).
66. Peterlin, P., Arrigler, V., Diamant, H. & Haleva, E. Permeability of Phospholipid Membrane for Small Polar Molecules Determined from Osmotic Swelling of Giant Phospholipid Vesicles. *Advances in Planar Lipid Bilayers and Liposomes Volume 16* 301–335 (2012). doi:10.1016/b978-0-12-396534-9.00010-6
67. Lee, B. W. *et al.* Structural effects of small molecules on phospholipid bilayers investigated by molecular simulations. *Fluid Phase Equilibria* **228-229**, 135–140 (2005).
68. Uzman, A. Molecular Cell Biology (4th edition) Harvey Lodish, Arnold Berk, S. Lawrence Zipursky, Paul Matsudaira, David Baltimore and James Darnell; Freeman & Co., New York, NY, 2000, 1084 pp., list price $102.25, ISBN 0-7167-3136-3. *Biochemistry and Molecular Biology Education* **29**, 126–128 (2001).
69. The ImageJ ecosystem: An open platform for biomedical image analysis - *Schindelin - 2015 - Molecular Reproduction and Development - Wiley Online Library*.
70. Schindelin, J. et al. Fiji: an open-source platform for biological-image analysis. *Nat. Methods* **9**, 676–682 (2012).
71. Klapoetke, N. C. et al. Independent optical excitation of distinct neural populations. *Nat. Methods* **11**, 338–346 (2014).
72. Hessel, C. M., Henderson, E. J. & Veinot, J. G. C. Hydrogen Silsesquioxane: A Molecular Precursor for Nanocrystalline Si—SiO2 Composites and Freestanding Hydride-Surface-Terminated Silicon Nanoparticles. *ChemInform* **38**, (2007)

Chapter 3: Sonofgragmentation of Ultra-thin 1D Nanomaterials.

Small (<10 nm) nanoparticles (NPs) are important because of the unique physical and chemical properties that arise due to their small size and large surface area [1–6]. A multitude of methods have been developed to produce such nanoparticles [7]. Top-down synthesis methods that rely on breaking down bulk materials into smaller fragments can be scalably deployed, but struggle with monodispersity and with yield for such small nanoparticles [8–18]; bottom-up synthesis methods can effectively assemble small molecule precursors into larger units to create small nanoparticles [19–32]. However, both methods require harsh chemicals [17,31] or specialized equipment [10,18,24,26,32] out of reach from many end users. Ideally, one could obtain extremely monodisperse nanoparticles of small size and high yield on regular benchtop equipment.

We here propose a top-down method of nanoparticle synthesis that results in high-yield and high-monodispersity nanoparticles, using only commonly available benchtop equipment. We hypothesized that nanowires of extreme aspect ratio could be ultrasonicated to generate nanoparticles. This hypothesis builds from recent studies [33–37] that show ultrasonication can be used to break down nanowires into shorter nanowires, and nanotubes into shorter nanotubes. We hypothesized that by choosing nanowires of specific aspect ratios, and then applying ultrasonication, it might be possible to perform top-down synthesis of many kinds of nanoparticle in effectively a single step.

Sonofragmentation of ultrathin Ge nanowires

We set out to test our hypothesis using ultrathin Ge nanowires (Fig. 1A). Up to date, synthesis of Ge NPs (< 10 nm) has been limited to gas-phase and liquid phase approaches that require expensive machines [38], and top-down approaches that do not yield monodisperse single crystalline nanoparticles [9,39]. Therefore, a simple and inexpensive method for top-down synthesis of Ge nanoparticles would be potentially of both scientific and commercial interest.

We first dispersed ultra-thin Ge nanowires [40] (diameters tapering from ~30 nm to ~2 nm) in DMF, and ultrasonicated the suspension with a bench-top ultrasonicator (40 kHz, 110 W). To track fragmentation of the nanowires, we imaged the ultrasonicated sample at different time points using scanning electron microscopy (SEM) (Fig. 1B top row, Fig. S1). We found that the nanowires readily fragmented into <30 nm particles within 30 minutes of ultrasonication. During the subsequent long-term ultrasonication, the particle size further decreased with increasing ultrasonication time. For instance, the majority of the nanoparticles had diameters of < 10 nm with 18 hour ultrasonication. As comparison, we carried out the same ultrasonication using a non-1D Ge substrate (100~300 nm diameter nanopowder) (Fig. 1B bottom row, Fig. S2). Contrary to the nanowires, the nanopowder did not show a clear change in particle size with increasing ultrasonication time. For instance, after 18 hours of ultrasonication, we observed a majority of ~100-300 nm particles, comparable to the size distribution of the starting material.

We analyzed the Ge NPs produced after 18 hours of nanowire ultrasonication using transmission electron microscopy (TEM). The nanoparticles were resuspended in ethanol, filtered through a 0.2 μm filter to remove large debris and aggregates, and drop-casted and dried on a copper/carbon grid (Fig. 2A). Analysis of the bright-field TEM images shows the nanoparticles had an average size of 3.58 nm and a standard deviation of 0.74 nm (n = 75 from a single TEM grid; Figure 2b), confirming generation of ultrasmall (< 10 nm) Ge NPs. We further carried out high-resolution TEM (HRTEM) imaging of the Ge NPs and found clear lattice fringes within the nanoparticle, indicating its single crystallinity (Fig. 2A). The result suggests that there is negligible amorphization effect during the long-term ultrasonication.

We further carried out dynamic laser scattering (DLS) analysis of the ultrasonicated Ge nanowire sample. Consistent with TEM analysis, we found that monodisperse (polydispersity (Pd) = 6.8%) Ge NPs of 3-5 nm diameters were generated after 18 hours of ultrasonication, with no further purification (Fig. 2C). In comparison, the Ge nanopowder substrate showed similar nanoparticle size range and distribution before (Pd = 16.2%) vs. after an ultrasonication time of 36 hrs (Pd = 19.1%) (Fig. S3). This result further suggests the advantage of using an ultra-thin 1D substrate to produce monodisperse ultrasmall nanoparticles.

To investigate optical properties of the synthesized Ge NPs, we measured the absorbance of the ultrasonicated sample using a UV-vis spectrometer (Fig. 2D, blue). We found the Ge NPs readily absorbed light with <400 nm wavelengths [41]. Next, we measured the intrinsic photoluminescence (PL) of the Ge NPs under optical excitation using a UV-vis spectrometer. The sample showed a characteristic PL peak around 410 nm wavelengths, consistent with previous reports (Fig. 2D, red) [21].

To study the surface of the synthesized Ge NPs, we performed Fourier transform infrared (FTIR) spectroscopy on the nanoparticles (Fig. 2E). The ultrasonicated Ge NPs were washed in chloroform three times and re-suspended in chloroform. The suspension was then drop-casted and air dried on the attenuated total reflectance (ATR) crystal before the FTIR measurements. The surface of the as-synthesized Ge NPs displayed both free hydroxyls (3334 cm-1) and DMFs, which are likely to be chemisorbed onto the surface through a C-O-Ge (1668 cm-1) bridge [42]. We further studied the surface of the NPs after solvent exchange and found that the DMF molecules were retained after solvent exchange to ethanol and water.

Generality of Principle - Sonofragmentation of different types of 1D substrates

To assess whether our method can be applied to different types of 1D substrates, we explored synthesis of NPs using various commercially available nanowires, including oxide and metal nanowires. We first carried out ultrasonication of TiO_2 nanowires in water (~10 nm diameter, Fig. 3A) for 24 hrs. TEM analysis shows that the average and standard deviation of the nanoparticle size were 4.63 nm and 1.28 nm, respectively, confirming generation of nanoparticles of <10 nm size (Fig. 3B, C). HRTEM images of nanoparticles showed clear lattice fringes, indicating that the nanoparticles were single crystalline (Fig. 3B). We further characterized the TiO_2 NPs in the solvent and found the nanoparticles had a monodisperse size distribution (Pd = 11%) of ~3-6 nm diameter, a range consistent with the TEM analysis (Fig. 3D).

Next we carried out ultrasonication of commercially available Ag nanowires (~20 nm diameter, Fig. 3E) in water using the same process for 24 hrs. TEM characterization of the Ag NPs showed that the average and standard deviation of the nanoparticle size were 3.46 nm and 0.75 nm, respectively and the nanoparticles were single crystalline (Fig. 3F, 3G). The nanoparticle suspension showed a monodisperse size distribution (% Pd = 15 %) with ~2-7 nm diameter (Fig. 3H).

Finally, we carried out ultrasonication of synthesized Si nanowires [43,44] (~30 nm diameter, Fig. 3I) in DMF for 24 hrs. The ultrasonication process yielded a monodisperse nanoparticle suspension. TEM analysis of the Si NPs showed that the average and standard deviation of the nanoparticle size were 10.8 nm and 2.2 nm, respectively, and the nanoparticles were single-crystalline (Fig. 3J, 3K). DLS analysis of the nanoparticle suspension showed a monodisperse size distribution (% Pd = 11.5 %) with ~10-12 nm diameter (Fig. 3I). To characterize optical properties of the synthesized Si NPs, we further measured PL of the Si NPs. The results showed the signature spectrum of ultrasmall Si NPs with the peak at around 400 nm in wavelength (Fig. S4).

Discussion

Based on previous theoretical and experimental studies of ultrasonication [33–37,45–47], we think the effects of long-term and continuous sonofragmentation on ultra-thin nanowires are two-fold: mechanical and chemical. In a previous study that used a theoretical model to calculate the tensile stress applied by a cavitation bubble, the tensile stress on a 1D nanostructure is shown to be dependent on the ratio of its diameter to its length [33,34]. The model suggests that thinner and longer nanowire and nanotube substrates can be more easily broken into fragments compared with substrates of low aspect ratio [33]. In another previous study, it had been predicted and shown for the case of carbon nanotubes, that shorter nanofragments are produced with increasing sonication times [34]. Our observation of nanoparticle generation from ultrasonication of high aspect ratio nanowires is consistent with these predictions and observations.

From a chemical point of view, the surface functionalization of the nanoparticles plays an important role in dispersing and stabilizing nanoparticles in solvents during the sonofragmentation [48,49]. FTIR analysis of the ultrasonicated Ge NPs suggests that the surfaces of nanoparticles are terminated with DMF molecules with CO groups coordinating to the surface of Ge. We suspect that these surface coordinated solvent molecules stabilize nanoparticles and prevent them from fast oxidation and decomposition. In addition, in the case of Ge NPs, the partially positive charge on the nitrogen terminal is likely to prevent the nanoparticles from aggregating in polar solvents such as DMF and ethanol and thus keep the nanoparticles dispersed in these solvents.

Our time-evolution experiment of the Ge fragments indicates a possible mechanism of nanoparticle generation during sonofragmentation. During the initial phase of the ultrasonication, the Ge nanowires rapidly fragment into <30 nm particles. This process is complete within ~30 minutes which is likely due to the high aspect ratio of the nanowire substrate. Increasing the ultrasonication time further reduces the size of these particles: with 18 hours of ultrasonication, the size range decreases to 3-5 nm.

Future investigation waits on both theoretical and experimental fronts. Additional theoretical modeling for sonofragmentation of ultra-thin inorganic substrates of different materials, diameters and lengths as well as mechanical properties might be explored. In addition, it may be of great interest to test specific substrate-solvent combinations and observe the effect of different solvents and surfactants on different substrates and on the sonofragmentation process itself.

In this report, we presented a new method of nanoparticle synthesis based on sonofragmentation of ultra-thin 1D substrates. We discovered that short-term ultrasonication of high-aspect ratio 1D substrates could rapidly generate highly-monodisperse nanoparticles, and longer-term ultrasonication could result in ultrasmall nanoparticles. We believe our method opens up a new approach, which is implementable with a bench-top ultrasonicator, to synthesize nanoparticles of high purity, crystallinity and monodispersity. Thus, our methodology democratizes small nanoparticle production, potentially opening up doors in a variety of fields that would benefit from the use of small nanoparticles for their chemical and physical properties.

Materials and Methods

Sonofragmentation: Sonofragmentation of 1D substrates were carried out using a bench-top bath ultrasonicator (40 kHz, max sonication power 110 W, Bransonic Ultrasonic Baths, Thomas Scientific). Starting materials in powder or suspended form (TiO_2 nanowires, Sigma-Aldrich; Ag nanowires, Novarials Corp.; Ge nanopowder, SkySpring Nanomaterials, Inc.) were added directly to an amber glass vial (4 ml, Sigma-Aldrich) with the solvents for the ultrasonication. Starting materials attached to a wafer substrate were first gently ultrasonicated in the solvents for 2 min and then the supernatant was transferred to another amber glass vial for the subsequent ultrasonication. The bath temperature of the ultrasonicator was not actively controlled.

Transmission Electron Microscope (TEM) and Scanning Electron Microscope (SEM) Characterizations: TEM characterization of the nanoparticles (NPs) was carried out using a JEM-2100 TEM (JEOL). The as-synthesized nanoparticles were (re)suspended in ethanol (for Ge, TiO_2 and Si NPs) or water (for Ag NPs) before being filtered through a 0.2 μm filter to remove large aggregates and debris. The suspension was then drop-casted on a carbon-copper grid (Ted Pella, Inc.), and dried in a vacuum desiccator for 20 min. The imaging was carried out at 200 keV under bright-field illumination. SEM characterization of the nanowires was carried out using an UltraPlus FE-SEM (Zeiss) with an inlens detector.

Dynamic Laser Scatterer (DLS) Characterization: DLS characterization of the nanoparticles was carried out with a dynamic light scattering instrument (DynaPro NanoStar, Wyatt Technology Corp.). About 100 μL of the sample was transferred to a disposable cuvette (Wyatt Technology Corp.) for the DLS measurement. The final histogram of nanoparticle size distribution was generated from 10 measurements for each sample.

Photoluminescence (PL) and UV-vis Absorption Characterization: PL characterization of the nanoparticles was carried out using a fluorescence spectrometer (Cary Eclipse, Agilent). About 40 ul of the sample was transferred to a quartz cuvette (Sigma-Aldrich) for the fluorescence measurement. UV-vis spectra of the nanoparticles were measured using a bench-top UV-vis spectrometer (NanoDrop 2000, ThermoFisher).

Fourier Transform Infrared (FTIR) Characterization: FTIR characterization of the Ge NPs was carried out using an FTIR spectrometer (SpectrumOne, Perkin Elmer). After 18 hours of ultrasonication in DMF, the nanoparticles were dried under vacuum and resuspended in chloroform for three times to completely remove the DMF. The nanoparticle suspension was then drop-casted onto the attenuated total reflection (ATR) crystal of the FTIR spectrometer and air-dried for 15 min before the measurement. The FTIR measurement was carried out for 3 min and the baseline was automatically corrected.

Nanowire Synthesis: Ge and Si nanowires were synthesized with vapor-liquid-solid (VLS) growth mechanism using published protocols.[40,43,44] Briefly, Ge nanowires were grown with 2 nm gold nanocatalyst for 150 min using GeH_4 (2 sccm) and H_2 (18 sccm) at total pressure of 400 torr and temperature of 270 °C. Si nanowires were grown for 60 min with 30 nm gold nanocatalyst using SiH_4 (2.5 sccm) and H_2 (60 sccm) at total pressure of 40 torr and temperature of 450 °C.

Figures:

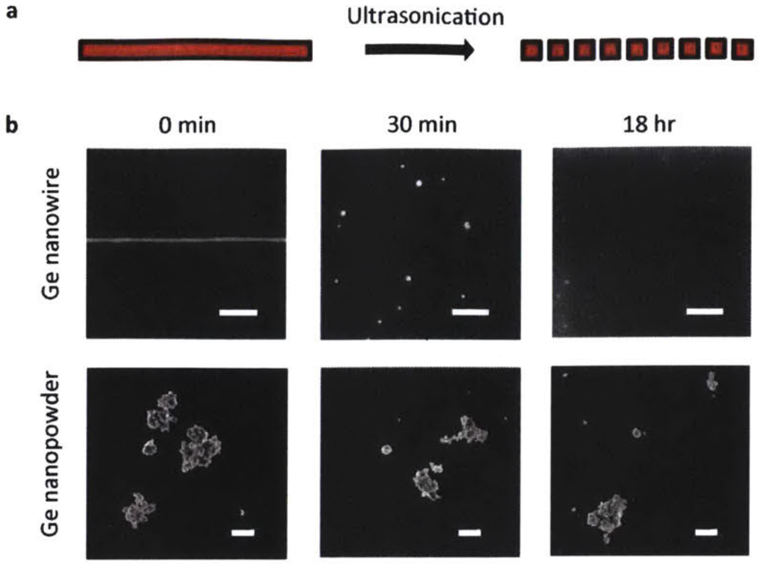

Figure 1. Synthesis of <10 nm nanoparticles via sonofragmentation. (A) Schematic of sonofragmentation of a high-aspect-ratio 1D nanostructure into nanoparticles. (B) Top row: scanning electron microscope (SEM) images of an ultrathin Ge nanowire (left) and fragments after 30 min (center) and 18 hours (right) of ultrasonication. Scale bars, 200 nm. Bottom row: SEM images of Ge nanopowder (left) and fragments after 30 min (center) and 18 hrs (right) of ultrasonication. Scale bars, 1 µm.

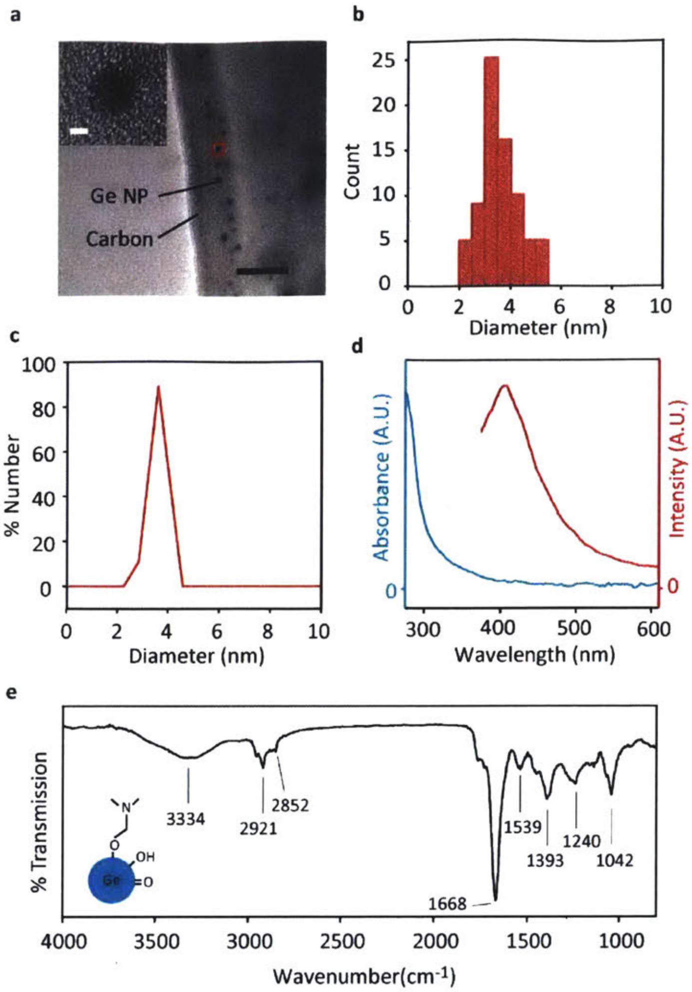

Figure 2. Sonofragmented Ge nanoparticles. (A) Transmission electron microscope (TEM) image of sonofragmented Ge nanoparticles (NPs). Scale bar, 50 nm. Inset, high-resolution TEM (HRTEM) image of a single Ge NP (red box). Scale bar, 2 nm. (B) Size distribution of the Ge NPs measured with TEM. The mean (μ) and standard deviation (σ) of the nanoparticle size, and the number of nanoparticles analyzed (n) were 3.58 nm, 0.74 nm and 75, respectively. (C) Size distribution of the Ge NPs measured with dynamic laser scattering (DLS) after 18 hour ultrasonication of Ge nanowires in DMF. (D) UV-vis absorbance spectrum of Ge NPs in DMF after 18 hour ultrasonication (blue) and photoluminescence (PL) in ethanol under 320 nm UV-illumination (red). For the PL measurement, the ultrasonication was carried out in DMF for 24 hrs and the Ge NPs were resuspended in ethanol. (E) Fourier transform infrared (FTIR) spectra of Ge NPs ultrasonicated in DMF for 24 hrs and resuspended in chloroform. Inset, schematic of possible functional groups on the Ge NP surface.

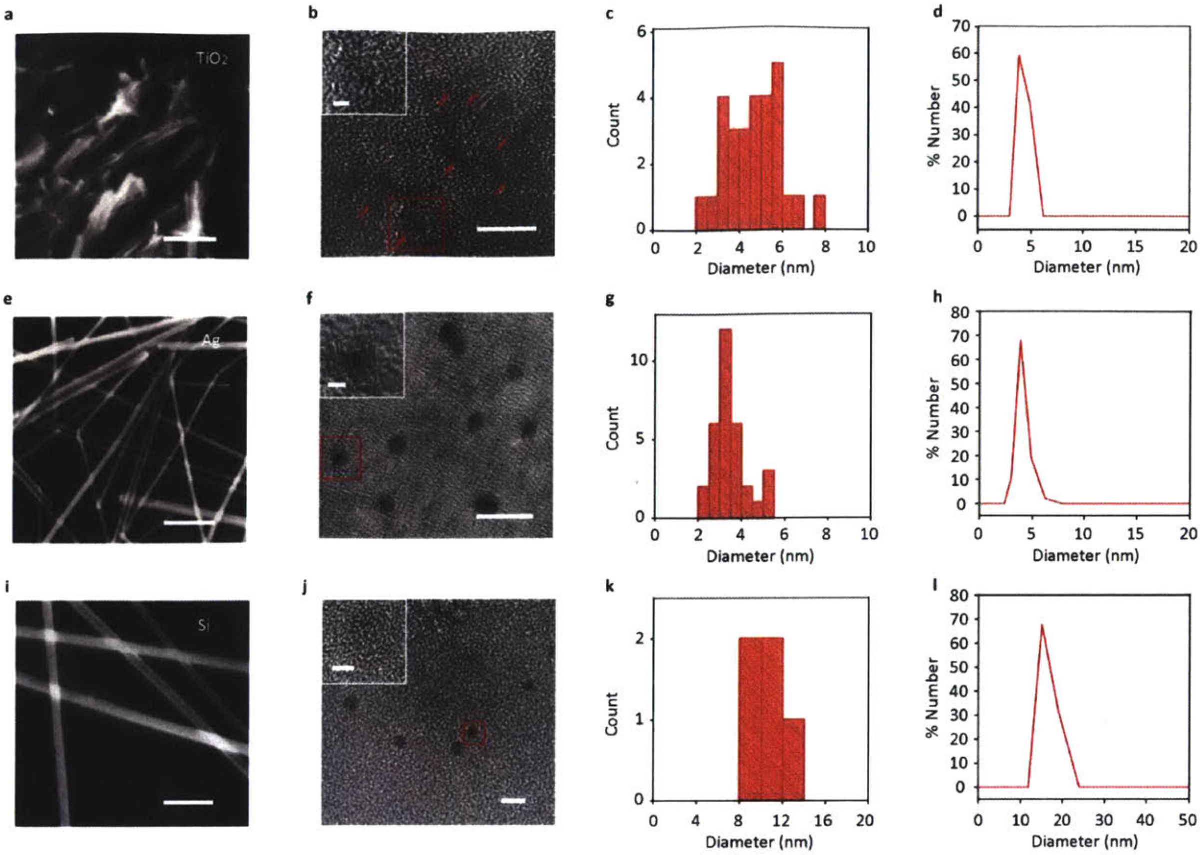

Figure 3. Sonofragmentation of ultra-thin oxide, metal and semiconductor nanowires. (A) SEM image of TiO_2 nanowires. Scale bar, 100 nm. (B) TEM image of TiO_2 NPs (red arrows) after 24 hour ultrasonication of the nanowires in water. Scale bar, 10 nm. Inset, HRTEM image of a single TiO_2 NP (red box). Scale bar, 2 nm. (C) Size distribution of the TiO_2 NPs measured with TEM (μ = 4.63 nm, σ = 1.28 nm, n = 27). (D) Size distribution of the TiO_2 NPs measured with DLS in water. (E) SEM image of Ag nanowires. Scale bar, 200 nm. (F) TEM image of the Ag NPs after 24 hour ultrasonication of the nanowires in water. Scale bar, 10 nm. Inset, HRTEM image of a single Ag NP (red box). Scale bar, 2 nm. (G) Size distribution of the Ag NPs measured with TEM (μ = 3.46 nm, σ = 0.75 nm and n = 32). (H) Size distribution of the Ag NPs measured with DLS in water. (I) SEM image of Si nanowires. Scale bar, 200 nm. (J) TEM image of the Si NPs after 24 hour ultrasonication of the nanowires in DMF. Scale bar, 20 nm. Inset, HRTEM image of a single Si NP (red box). Scale bar, 5 nm. (K) Size distribution of the Ag NPs measured with TEM (μ = 10.8 nm, σ = 2.2 nm , n = 5). (L) Size distribution of the Si NPs measured with DLS in DMF.

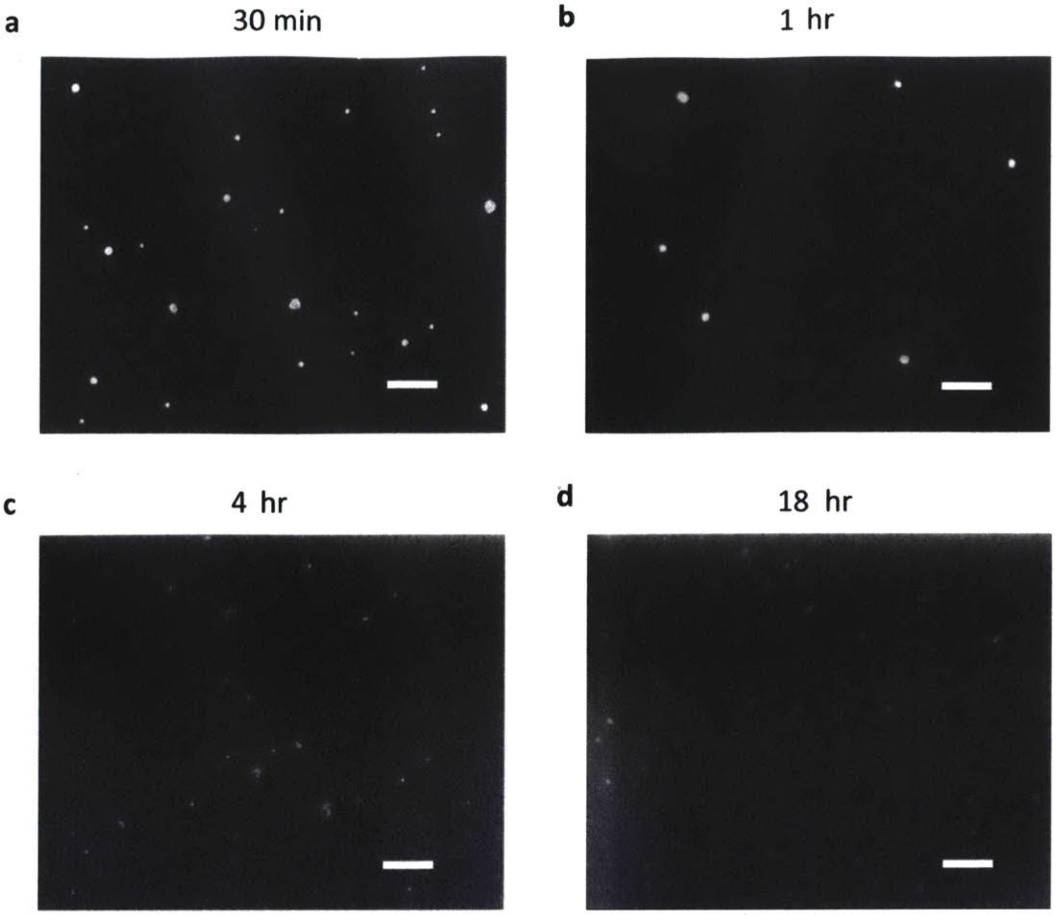

Figure S1. Scanning electron microscope (SEM) images of ultrasonicated Ge nanowires in DMF after (A) 30 min, (B) 1 hour, (C) 4 hours and (D) 18 hours of continuous ultrasonication. The samples were resuspended in ethanol before drop-casted to a Si substrate for the SEM imaging. Scale bars, 200 nm.

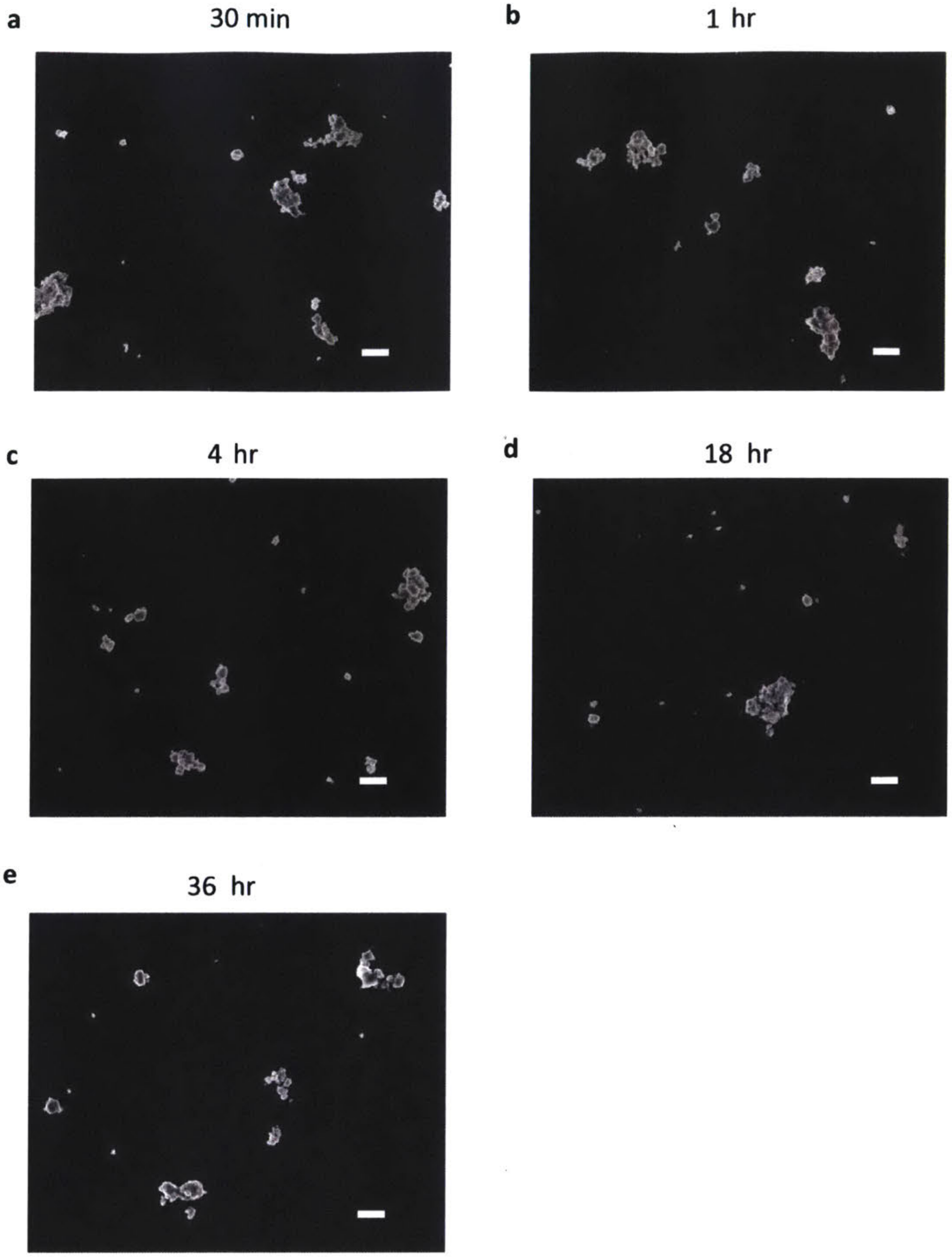

Figure S2. SEM images of ultrasonicated Ge nanopowder (~100-300 nm dimeter) in DMF after (A) 30 min, (B) 1 hour, (C) 4 hours, (D) 18 hours and (E) 36 hours of continuous ultrasonication. The samples were resuspended in ethanol before drop-casted to a Si substrate for the SEM imaging. Scale bars, 1 μm.

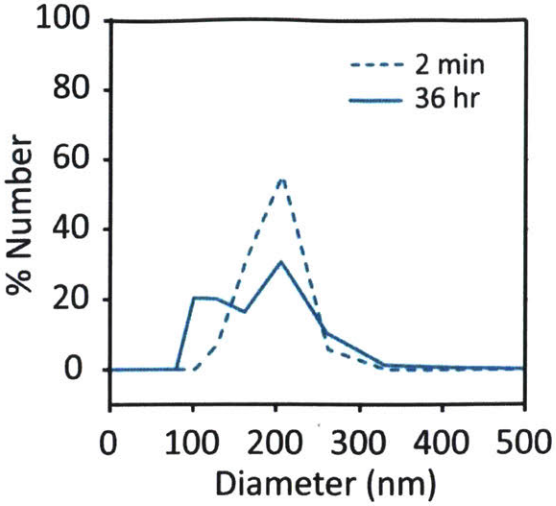

Figure S3. Size distribution of Ge NPs measured with dynamic laser scattering (DLS) after 2 min (dotted blue) and 36 hrs (solid blue) of ultrasonication of the Ge nanopowder.

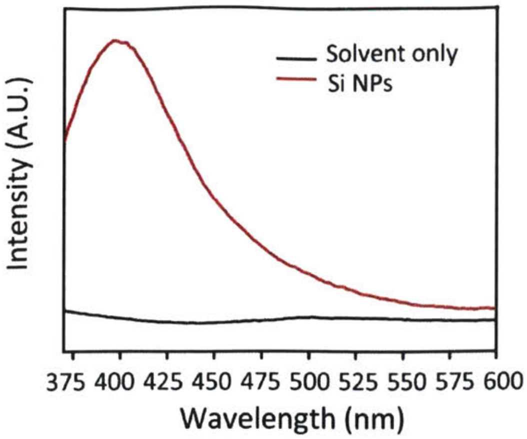

Figure S4. Photoluminescence (PL) of Si NPs in ethanol under 320 nm nm UV-illumination. Ultrasonication was carried out in DMF for 24 hrs and the solvent was exchanged to ethanol for the PL measurement.

References

1. Kim, B. H., Hackett, M. J., Park, J. & Hyeon, T. Synthesis, characterization, and application of ultrasmall nanoparticles. *Chemistry of Materials* **26**, 59–71 (2014).
2. Zarschler, K. *et al.* Ultrasmall inorganic nanoparticles: state-of-the-art and perspectives for biomedical applications. *Nanomedicine Nanotechnol. Biol. Med.* (2016). doi:10.1016/j.nano.2016.02.019
3. Ma, K., Werner-Zwanziger, U., Zwanziger, J. & Wiesner, U. Controlling growth of ultrasmall sub-10 nm fluorescent mesoporous silica nanoparticles. *Chem. Mater.* **25**, 677–691 (2013).
4. Li, Z. *et al.* Ultra-small fluorescent inorganic nanoparticles for bioimaging. *J. Mater. Chem. B* **2**, 2793 (2014).
5. Lundqvist, M. *et al.* Nanoparticle size and surface properties determine the protein corona with possible implications for biological impacts. *Proc. Natl. Acad. Sci. U. S. A.* **105**, 14265–70 (2008).
6. Albanese, A., Tang, P. S. & Chan, W. C. W. The effect of nanoparticle size, shape, and surface chemistry on biological systems. *Annu. Rev. Biomed. Eng.* **14**, 1–16 (2012).
7. Masala, O. & Seshadri, R. Synthesis Routes for Large Volumes of Nanoparticles. *Annu. Rev. Mater. Res.* **34**, 41–81 (2004).
8. Amendola, V. & Meneghetti, M. What controls the composition and the structure of nanomaterials generated by laser ablation in liquid solution? *Phys. Chem. Chem. Phys.* 3027–3046 (2012). doi:10.1039/c2cp42895d
9. Shirahata, N., Hirakawa, D., Masuda, Y. & Sakka, Y. Size-dependent color tuning of efficiently luminescent germanium nanoparticles. *Langmuir* **29**, 7401–7410 (2013).
10. Shirahata, N. *et al.* Laser-derived one-pot synthesis of silicon nanocrystals terminated with organic monolayers. *Chem. Commun. Camb. Engl.* 4684–4686 (2009). doi:10.1039/b905777c
11. Prasad Yadav, T., Manohar Yadav, R. & Pratap Singh, D. Mechanical Milling: a Top Down Approach for the Synthesis of Nanomaterials and Nanocomposites. *Nanosci. Nanotechnol.* **2**, 22–48 (2012).
12. Lam, C. *et al.* Large-scale synthesis of ultrafine Si nanoparticles by ball milling. *J. Cryst. Growth* **220**, 466–470 (2000).
13. Gaffet, E. Phase transition induced by ball milling in germanium. *Mater. Sci. Eng. A* **136**, 161–169 (1991).
14. Luna López, J. A. *et al.* Synthesis of colloidal solutions with silicon nanocrystals from porous silicon. *Nanoscale Res. Lett.* **9**, 1–11 (2014).
15. Del Cano, T. *et al.* Porous SiGe nanostructures formed by electrochemical etching of thin poly-SiGe films. *J. Electrochem. Soc.* **151**, C326–C332 (2004).
16. Kartopu, G. *et al.* Can chemically etched germanium or germanium nanocrystals emit visible photoluminescence? *Phys. Status Solidi A* **202**, 1472–1476 (2005).
17. Hwang, J. *et al.* Simple Preparation of Fluorescent Silicon Nanoparticles from Used Si Wafers. *Ind. Eng. Chem. Res.* **54**, 5982–5989 (2015).
18. Zeng, H. *et al.* Nanomaterials via laser ablation/irradiation in liquid: A review. *Advanced Functional Materials* **22**, 1333–1353 (2012).
19. Tilley, R. D. & Yamamoto, K. The microemulsion synthesis of hydrophobic and hydrophilic silicon nanocrystals. *Adv. Mater.* **18**, 2053–2056 (2006).

20. Taylor, B. R., Kauzlarich, S. M., Delgado, G. R., Lee, H. W. H. & Nanocrystals, L. E. S. Solution Synthesis and Characterization of Quantum Confined Ge Nanoparticles. *Chem. Mater* **11**, 2493–2500 (1999).
21. Wu, H. P. *et al.* Blue emission of Ge nanocrystals prepared by thermal decomposition. *Nanotechnology* **17**, 5339–5343 (2006).
22. Stoldt, C. R., Haag, M. A. & Larsen, B. A. Preparation of freestanding germanium nanocrystals by ultrasonic aerosol pyrolysis. *Appl. Phys. Lett.* **93**, (2008).
23. Erogbogbo, F. *et al.* Creating ligand-free silicon germanium alloy nanocrystal inks. *ACS Nano* **5**, 7950–7959 (2011).
24. Kortshagen, U. Nonthermal plasma synthesis of semiconductor nanocrystals. *J. Phys. Appl. Phys.* **42**, 113001 (2009).
25. Ou, H., Ou, Y., Liu, C., Berg, R. W. & Rottwitt, K. Formation and characterization of varied size germanium nanocrystals by electron microscopy, Raman spectroscopy, and photoluminescence. *Opt. Mater. Express* **1**, 643 (2011).
26. Li, S., Germanenko, I. N. & El-Shall, M. S. Nanoparticles from the Vapor Phase: Synthesis and Characterization of Si, Ge, MoO3, and WO3Nanocrystals. *J. Clust. Sci.* **10**, 533–547 (1999).
27. Das, K., Goswami, M. L. N., Dhar, A., Mathur, B. K. & Ray, S. K. Growth of Ge Islands and Nanocrystals Using RF Magnetron Sputtering and their Characterization. *Nanotechnology* **18**, 175301–1753015 (2007).
28. Chang, S. S., Choi, G. J. & Hummel, R. E. Optical properties of spark-processed Ge. *Mater. Sci. Eng. B Solid-State Mater. Adv. Technol.* **76**, 237–240 (2000).
29. Hoffman, M. & Veinot, J. G. C. Understanding the formation of elemental germanium by thermolysis of sol-gel derived organogermanium oxide polymers. *Chem. Mater.* **24**, 1283–1291 (2012).
30. Bux, S. K. *et al.* Rapid solid-state synthesis of nanostructured silicon. *Chem. Mater.* **22**, 2534–2540 (2010).
31. Henderson, E. J., Seino, M., Puzzo, D. P. & Ozin, G. A. Colloidally stable germanium nanocrystals for photonic applications. *ACS Nano* **4**, 7683–7691 (2010).
32. Gupta, A., Swihart, M. T. & Wiggers, H. Luminescent colloidal dispersion of silicon quantum dots from microwave plasma synthesis: Exploring the photoluminescence behavior across the visible spectrum. *Adv. Funct. Mater.* **19**, 696–703 (2009).
33. Huang, Y. Y., Knowles, T. P. J. & Terentjev, E. M. Strength of nanotubes, filaments, and nanowires from sonication-onduced scission. *Adv. Mater.* **21**, 3945–3948 (2009).
34. Lucas, A. *et al.* Kinetics of nanotube and microfiber scission under sonication. *J. Phys. Chem. C* **113**, 20599–20605 (2009).
35. Stegen, J. Mechanics of carbon nanotube scission under sonication. *J. Chem. Phys.* **140**, (2014).
36. Park, M., Sohn, Y., Shin, W. G., Lee, J. & Ko, S. H. Ultrasonication assisted production of silver nanowires with low aspect ratio and their optical properties. *Ultrason. Sonochem.* **22**, 35–40 (2015).
37. Chew, H. B., Moon, M.-W., Lee, K. R. & Kim, K.-S. Compressive dynamic scission of carbon nanotubes under sonication: fracture by atomic ejection. *Proc. R. Soc. Math. Phys. Eng. Sci.* **467**, 1270–1289 (2010).
38. Kim, S. *et al.* Size tailoring of aqueous germanium nanoparticle dispersions. *Nanoscale* **6**, 10156–60 (2014).

39. Liu, J., Liang, C., Tian, Z., Zhang, S. & Shao, G. Spontaneous growth and chemical reduction ability of Ge nanoparticles. *Sci. Rep.* **3**, 1741 (2013).
40. Lauhon, L. J., Gudiksen, M. S., Wang, C. L. & Lieber, C. M. Epitaxial core-shell and core-multishell nanowire heterostructures. *Nature* **420**, 57–61 (2002).
41. Carolan, D. & Doyle, H. Size Controlled Synthesis of Germanium Nanocrystals: Effect of Ge Precursor and Hydride Reducing Agent. *J. Nanomater.* **2015**, 1–9 (2015).
42. Keung, A. J., Filler, M. A. & Bent, S. F. Thermal control of amide product distributions at the Ge(100)-2x1 surface. *J. Phys. Chem. C* **111**, 411–419 (2007).
43. Cui, Y., Lauhon, L. J., Gudiksen, M. S., Wang, J. & Lieber, C. M. Diameter-controlled synthesis of single-crystal silicon nanowires. *Appl. Phys. Lett.* **78**, 2214–2216 (2001).
44. Patolsky, F., Zheng, G. & Lieber, C. M. Fabrication of silicon nanowire devices for ultrasensitive, label-free, real-time detection of biological and chemical species. *Nat. Protoc.* **1**, 1711–1724 (2006).
45. Zeiger, B. W. & Suslick, K. S. Sonofragmentation of molecular crystals. *J. Am. Chem. Soc.* **133**, 14530–14533 (2011).
46. Sander, J. R. G., Zeiger, B. W. & Suslick, K. S. Sonocrystallization and sonofragmentation. in *Ultrasonics Sonochemistry* **21**, 1908–1915 (2014).
47. Saito, T., Kuramae, R., Wohlert, J., Berglund, L. A. & Isogai, A. An ultrastrong nanofibrillar biomaterial: The strength of single cellulose nanofibrils revealed via sonication-induced fragmentation. *Biomacromolecules* **14**, 248–253 (2013).
48. Tsai, M. Y., Yu, C. Y., Wang, C. C. & Perng, T. P. Water-driven formation of luminescent Zn2GeO4 nanorods from Zn-containing Ge nanoparticles. *Cryst. Growth Des.* **8**, 2264–2269 (2008).
49. Hanrath, T. & Korgel, B. A. Chemical surface passivation of Ge nanowires. *J. Am. Chem. Soc.* **126**, 15466–15472 (2004).

CHAPTER 4: NVND delivery to neural membranes

Numerous color centers in diamond have been identified with specific optical and spin-based properties. The nitrogen vacancy (NV) color center, in particular, is photostable, and has an exceptionally long-lived spin-triplet ground state that can be efficiently interfaced to for optically detected magnetic resonance (ODMR), even under ambient conditions. The NV center has enabled a range of precision nanoscale sensing applications, including magnetic resonance detection of individual external electronic [1] and nuclear spins [2], nanoscale detection of electric fields [2,3], sub-Celsius thermometry in living cells [4], strain imaging [5,6], and pH sensing [7]. When embedded in nanocrystals, NV centers can serve as photostable and low-toxicity [8] fluorescent biomarkers, with a near-infrared emission spectrum that has low absorption in biological tissue. NVs also enable sub-diffraction optical localization and imaging [9-12], and unique ODMR signatures allow for particle tracking in live cells [13,14]. NV charge dichroism allows for detection of voltage changes across electrolytic interfaces with sub-100 mV resolution and ms-scale integration [15]. However, to translate these sensing and imaging modalities to cells, a key remaining challenge is targeted staining of cell membranes with singly dispersed NDs. Past studies have focused on cellular delivery of hydroxyl-terminated NDs (OH NVNDs) through endocytosis [16,17], but precise targeting of membranes and prevention of agglomeration have not been reported. Agglomeration of NVNDs has been shown, for example, to hamper neurite growth [18].

In this chapter, we perform targeted labeling of NVNDs to the cell membrane using hydrophobic surface termination to stabilize NDs on the lipid bilayer. We focus on staining neural membranes, which are of particular interest for neuroscience research, but anticipate that our methods should be translatable to other cell types.

The process is outlined in Fig. 1. Commercial nanodiamonds (Adámas Nanotechnologies, made via the high-pressure-high temperature (HPHT) method) were silanized, producing a hydrophobic shell. They were then encapsulated in PEG350-PE micelles, dispersed in physiological buffer, and subsequently incubated with primary neurons for a few minutes, then washed. Finally, the samples were imaged by optical or electron microscopy, as detailed below.

Hydrophobization and micelle encapsulation of NVNDs

Our study used high-pressure, high-temperature (HPHT) NDs of two size classes: 40 nm mean diameter with ~15 NVs per ND, and 100 nm mean diameter with ~500 NVs per ND. The NDs were initially terminated with ethers, esters, as well as carboxyl- and hydroxyl-groups, as detected by FTIR (Fig. S1). These NDs were hydrophilic and stable in water. Because of their hydroxyl termination [19], these hydrophilic NVNDs are here referred to as OH-NVNDs (Fig. 2A, C).

We homogenized the surface ND functional groups to hydroxyls by $LiAlH_4$ reduction [20] and produced hydrophobic surfaces by silanization [21]. In this reaction, the hydroxyl surface groups serve as anchor points for N-octyltriethoxysilane (OTES) molecules. Transmission electron microscopy (TEM) on the resulting NDs showed that silanization produced a 5nm shell (Fig. 2B, D and F) around all the NDs (Fig. 2G, H). Fourier transform infrared spectroscopy (FTIR) and energy dispersive X-ray spectroscopy (EDX) data confirmed silicon (Fig. S1, Fig. 2J) in this shell; the Si shell was absent in the OH-NVNDs (Fig. S1, Fig. 2E, I). The silanized NDs (Si-NVNDs) were stable in the organic solvents toluene or chloroform for 24-48 hours.

The next challenge was to transfer these Si-NVNDs into physiological solutions such as Tyrode solution. We addressed this problem by the use of micelles as delivery agents, as previously described for micellation of colloidal quantum dots [22]. We created micelles using PEG350 conjugated phosphoethanolamine (PEG-PE) at a 10^6:1 molar excess relative to the nanodiamonds. Bath sonication was used to disperse these micellated Si-NVNDs in Tyrode solution for further experiments.

Labeling of neurons with micellated hydrophobic NVNDs

We tested the micellated Si-NVNDs on cultured primary hippocampal neurons. We incubated neurons in Tyrode with either OH-NVNDs or micellated Si-NVNDs for 5-10 minutes, followed by washing with a 10X volume of Tyrode.

We performed optical confocal microscopy of neurons stained by each of these kinds of functionalized NVNDs (Fig. 3). We used a membrane stain (WGA-488) to show whether NVNDs were internalized into the neural cytosol or stayed on the cell membrane (with the caveat that our resolution is limited by optical diffraction). This co-labeling allowed us to estimate the fraction of NVNDs on the membrane vs. inside the cell. Immediately after incubation (0.5 h), 95+/-8% of the Si-NVNDs (Fig. 3A) and 76+/- 8% of OH-NVNDs (Fig. 3D; values are mean +/- s.e.m.; n =5 neurons from 2 cultures for Si-NVND labeled cells and 6 neurons from 2 cultures for OH-NVND labelled cells) appeared on the neural membrane. After 6 hours, these percentages dropped to 89+/-3% for Si-NVNDs (Fig. 3B) and 32+/-12% for OH-NVNDs (Fig. 3E; n = 5 neurons from 2 cultures for Si-NVND labeled cells and 9 neurons from 2 cultures for OH-NVND labelled cells), and at 12 h reached 69%+/-4 for Si-NVNDs (Fig. 3C) and 20+/-12% for OH-NVNDs (Fig. 3F; n = 6 neurons from 2 cultures for Si-NVND labeled cells and 6 neurons from 2 cultures for OH-NVND labelled cells). For both 6h and 12h following incubation, we found a significantly higher percentage of Si-NVNDs on the membrane compared to OH-NVNDs (population data in Fig. 3G), for NVNDs of 100 nm mean diameter. We obtained similar results for NVNDs of mean diameter 40 nm (Fig. S4).

To verify that the red fluorescent spots in these confocal microscopy studies indeed originated from NVNDs, we performed optically detected magnetic resonance (ODMR) and found NV resonant frequencies for both 100nm (Fig 4A-D) and 40nm (Fig. S2) Si-NVNDs delivered to neurons.

Single NVNDs contact neural cell membrane

We performed transmission electron microscopy (TEM) of neurons labeled with NVNDs. Since confocal imaging demonstrated that at 0.5h more than 90% of Si-NVNDs resided in close proximity to the membrane, following incubation we immediately fixed neurons and prepared them for electron microscopy imaging. We found that 100nm and 40nm Si-NVNDs physically touched the membrane, and appeared monodisperse (Fig. 5A, C, and E-H). In contrast, OH-NVNDs formed aggregates outside cells, and only a fraction of the nanodiamonds came in physical contact with the membrane (Fig. 5B, D, and E-H). Similarly, scanning electron microscopy (SEM) performed on non-labeled neurons (Fig. 5I) and NVND-labeled neurons revealed that Si-NVNDs labeled neural membranes in a monodisperse-appearing fashion (Fig. 5J, L). OH-NVNDs on neurons, in contrast, had a wide size distribution and formed aggregates (Fig. 5K, M). For both OH-NVNDs and Si-NVNDs, the fact that the nanodiamonds did not wash away during the fixation process suggests that nanodiamonds were bound to the cells.

NVNDs depict the morphology of neurons with single and multiphoton optical microscopy

We imaged Si-NVND labeled neurons (Fig. 6) immediately (0.5h) after staining. Widefield imaging with 532 nm excitation showed that both 100nm and 40nm Si-NVNDs labeled neurons along the cell body as well as the neurites, co-localizing with the membrane (Fig. 6, compare B with C, E with F; Fig. S4A-C). In contrast, OH-NVNDs did not label neuron membranes, and instead formed micron-scale aggregates that did not colocalize with the membrane (Fig. 6, compare H with I, K with L). We performed 2-photon imaging of Si-NVND labeled neurons (Fig. 7). We labeled neurons with 100nm NV-NDs and imaged them with an 870nm laser to excite NV^0 as described before [14]. Putative single Si-NVNDs could be easily detected along the membranes of the neuron (Fig 7B, F, J; Fig. 7D, H, L) labeling both cell bodies and neural processes, while OH-NVNDs aggregated into micron-scale aggregates outside neurons (Fig 7A, E, I; Fig. 7C, G, K).

Toxicity of micellated hydrophobic NVNDs

We assessed neural viability with 100nm-diameter Si-NVNDs and OH-NVNDs by co-staining with propidium iodide (PI) after a 12 hour incubation of cultured neurons with nanodiamonds. As seen in Fig. S3, there was no significant increase in PI-labeled cells following nanodiamond labeling, indicating that neither OH-NVNDs nor Si-NVNDs significantly increase neural death during a 12 h period.

Discussion

It has been previously shown that amphiphilic copolymer (i.e. PEG-PE) micelles insert into and release their small molecule cargo at cellular membranes [23,24]. We here found that this effect can also be used for the delivery of Si-NVNDs. We find that these Si-NVNDs are retained at the cell membrane over a period of 6-12 hours at a rate significantly greater than that of OH-NVNDs. The uptake of large molecules from lipid membranes into the cytosol primarily relies on endocytosis [23,25]. The disparate uptake rates between Si- and OH-NVNDs could have been due to many effects, including changes in local membrane fluidity caused by the size, charge and proximity of NVNDs [26-28], which affects their rates of endocytosis [29-31].

We did not observe a decrease in neural viability (Fig. S3) due to labelling with micellated Si-NVND. The toxicity of micelles is known to depend on concentration and composition. The PEG-PE micelles used in this study are known to exhibit low cytotoxicity [22,23]. Furthermore, we used very low laser powers for one-photon (532 nm) : 350 mW/mm^2, and two-photon (870 nm) : 32 mW/mm^2 imaging to minimize any phototoxicity that may occur.

We expect that the membrane delivery method described in this chapter will enable measurements of biological phenomenon at or near neural membranes. The most relevant being the optical measurement of action potentials, corresponding to membrane potential changes of ~100 mV. Based on previous findings [15], we calculated that the minimum number of NVs needed is approximately 10^3. These numbers suggest that one NVND is not enough for action potential sensing since the average number of NV centers on each of the 100 nm-diameter NVNDs is 500, and thus one would need to increase the density of NV centers per nanodiamond (see Appendix).

In conclusion, here we describe a method to deliver monodisperse nanodiamonds to the membranes of live neurons. This approach overcomes two central challenges in nanodiamond staining: targeting and monodispersity. This method should help support a range of NVND-based sensing applications, and may facilitate the delivery of further nanoparticle-based sensors that require the delivery of isolated particles to cell membranes.

Materials and Methods

FTIR. For FTIR analysis, 0.1 mg of 100 nm OH-NVNDs or Si-NVNDs was deposited on a polished KBr window (Sigma Aldrich) and were dried in an oven at 70°C overnight. The infrared absorption spectra of NDs in transmission mode were acquired using a Thermo Fisher FTIR6700 Fourier Transform Infrared (FTIR) Spectrometer. All spectra represent an average of 32 scans with a resolution of 4 cm^{-1}.

ND functionalization with silane. NVNDs were procured (Adamas Nanotechnologies, Raleigh, NC) and incubated at 70°C in vacuo overnight to remove any adsorbed water.

Hydroxylation of NVNDs to produce OH-NVNDs: NVNDs (200 mg) were added to a round bottom flask and purged with nitrogen. Anhydrous degassed tetrahydrofuran (THF, 10 ml, room temperature) was then transferred to the flask using a cannula followed by the dropwise addition of $LiAlH_4$ solution in THF (2.0M, 7ml, room temperature). The reaction was left to reflux overnight at 70°C. Excess $LiAlH_4$ was quenched by dropwise addition of HCl (6N, 10ml). The reduced nanodiamond product was collected by centrifugation (Beckman Coulter, 4000 rcf), rinsed five times with ethanol, and dried using acetone.

Silanization of OH-NVNDs to produce Si-NVNDs: OH-NVNDs (20mg) were dried in a round bottom flask at 70°C in vacuo overnight. The flask was then purged with nitrogen. Dry toluene (10ml) and N-octyltriethoxysilane (OTES, 50 μl) were then transferred to the flask by cannula. The solution was fully dispersed by sonication in an ultrasonic bath. The sample was then stirred under nitrogen atmosphere at room temperature overnight. Excess OTES was removed by five consecutive washing/centrifugation cycles with acetone. The ND pellet was then dried in vacuo at 70°C.

Micellation. 100nm Si-NVNDs (100 μl, 1mg/ml) in chloroform were mixed with 1,2-dimyristoyl-sn-glycero-3-phosphoethanolamine-N-[methoxy(polyethylene glycol)-350] (PEG-PE, from Avanti Polar LIpids; 50μl at 1mg/ml) in chloroform at room temperature. An additional 350μl of chloroform was added to raise the final volume of the mixture to 500μl. The mixture was subsequently dried at 60°C in vacuo for 2hrs. After evaporation of chloroform, the tube was placed in an 80°C water bath for 1min. 600μl of water warmed to 80°C was added to the residue, and the nanodiamond-micelle residue was then suspended by pipetting up and down several times. The suspension was left in the bath for an additional 5 minutes to allow micelle encapsulation of the nanodiamonds. Finally, empty micelles were removed from the suspension by dialysis over 24hrs using a 100kDa MWCO dialysis bag (Micro Float-a-lyzer, Spectrum labs).

Neural labeling with NVNDs. For labeling, primary hippocampal cultured neurons were used as described before [34]. First, neural growth media was replaced by 300µl Tyrode solution (consisting of, in mM, 125 NaCl, 2 KCl, 3 CaCl2, 1 MgCl2, 10 HEPES, 30 Glucose, pH 7.3 NaOH adjusted, 305 mOsm). Then, we added 30µl of solution containing either 100nm or 40nm micellated Si-NVNDs or non-micellated OH-NVNDs. Neurons were then placed in a 37°C incubator for 5-10 minutes and thoroughly washed with Tyrode four times thereafter. Since neural labeling took up to 10 minutes and the setup time for microscopy of the samples took another 10-15 minutes, we defined our initial imaging time-point as approximately 0.5h.

Propidium iodide staining. Hippocampal neurons were labeled with 100nm micellated Si-NVNDs or with 100nm OH-NVNDs for 12 hours. Neurons were co-labeled with propidium iodide (3uM) and Hoechst3342 (1 µg/ml) for 15 minutes. Neurons with compromised membranes were determined using epifluorescence microscopy (Nikon Eclipse Ti) and propidium iodide uptake using LED excitation at 560nm (Lumencore), using emission filter FITC/TXRED-2X-B-000 (Semrock). The total number of neurons was determined by Hoechst33342 uptake using excitation 405nm (Lumencore), using emission filter DAPI-11p-A-000 (Semrock)

Widefield microscopy. NDs and neurons labeled with NDs were imaged on a widefield Leica 3000B, with excitation via a 532nm 150mW CW CDRH USB Laser System (Coherent Laser group) at 80mW. The cells were imaged with a x63 Plan-Apo lens. Fluorescence was collected through a 633 nm long-pass filter (Semrock).

Confocal microscopy. All images were taken on Zeiss LSM 700 microscope with a plan apochromat 40X/1.3 oil DIC M27 objective at a 2.0X digital zoom. The scan time for images was 30.98s and the pixel dwell time was 6.30 µs. For imaging of WGA-488 labeled neurons we used a 488nm laser with a bandpass emission filter from 490-555nm. For ND imaging we used a 555nm laser with a longpass 560 emission filter.

Two photon microscopy. The 2p imaging system consisted of a Prairie Technologies Ultima IV two-photon imaging system utilizing a Spectra Physics Mai Tai HP DeepSee laser. The laser wavelength was 870nm and the objective a Zeiss 40x Plan-Apochromat DIC (UV) VIS-IR 1.0NA water immersion objective. Scanning was performed at 12 µs per pixel dwell time at a zoom of 2x.

Transmission electron microscopy. Hippocampal neurons were plated in a 35mm plastic dish, and then fixed in 2.5% glutaraldehyde/ 3% paraformaldehyde with 5% sucrose in 0.1M sodium cacodylate buffer (pH 7.4) for one hour. Neurons were then washed with 0.1 M sodium cacodylate buffer three times, then postfixed in 1% OsO4 in veronal-acetate buffer 1 hour. The cells were stained en block overnight with 0.5% uranyl acetate in veronal-acetate buffer then dehydrated with a standard graded series of ethanol (at 35%, 50%, 70%, 95%, 100% v/v) and embedded in Embed 812 resin. Cells were cut cross sectional to the dish with a Leica Ultracut UCT microtome with a Diatome diamond knife at a thickness setting of 50 nm. The sections were examined using a FEI Tecnai Spirit at 80KV.

HR TEM and EDX spectra of NDs. Imaging on a JEOL 2100 FEG microscope was done using the biggest area size of parallel illumination beam and 100µm diameter condenser aperture. The microscope was operated at 200 kV and with a magnification in the range of 20,000 to 800,000 for assessing particle size and distribution and atomic arrangement. All images were recorded on a Gatan 2kx2k UltraScan CCD camera. STEM imaging was done with a HAADF (high-angle annular dark field) detector with 0.5nm probe size and 12cm camera length. An EDX (X-MAX, 80mm2) system was used to get chemical information.

Scanning electron microscopy. For SEM imaging, neurons were cultured on a cover glass and freeze-dried. A thin-layer of Au-Pd alloy was sputter-coated on the freeze-dried neurons to avoid charging. The sputter-coated neurons were imaged using a Raith 150 scanning electron microscope operated with an acceleration voltage of 10kV, after mounting the cover glass with the neurons on a carbon planchet.

Figures:

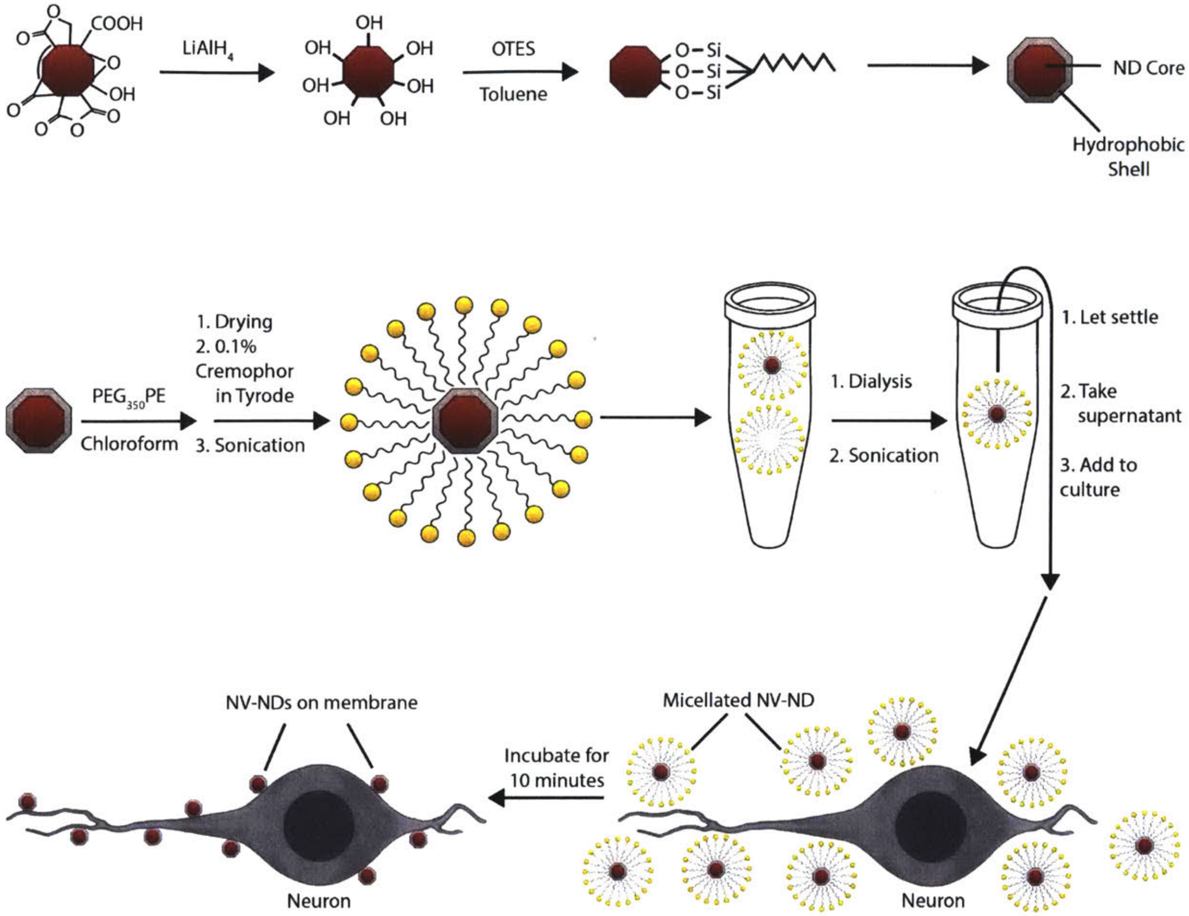

Figure 1. NVND functionalization, micellation and neural labeling strategy. OH-NVNDs exhibit multiple functional groups, including hydroxyls, ethers, esters and carboxyls. To render the OH-NVNDs hydrophobic they were first reduced using $LiAlH_4$ and then silanized using octyl triethoxy silane (OTES) bearing an eight-carbon-chain. To solubilize the hydrophobic Si-NVNDs in water, we micellated them using PEG-ylated phosphoethanolamine in Tyrode's solution. To get rid of empty micelles we dialyzed the micellated Si-NVNDs overnight. Thereafter, the micellated Si-NVND suspension was added to cultured neurons. NVNDs could be detected on neural membranes within 10 minutes.

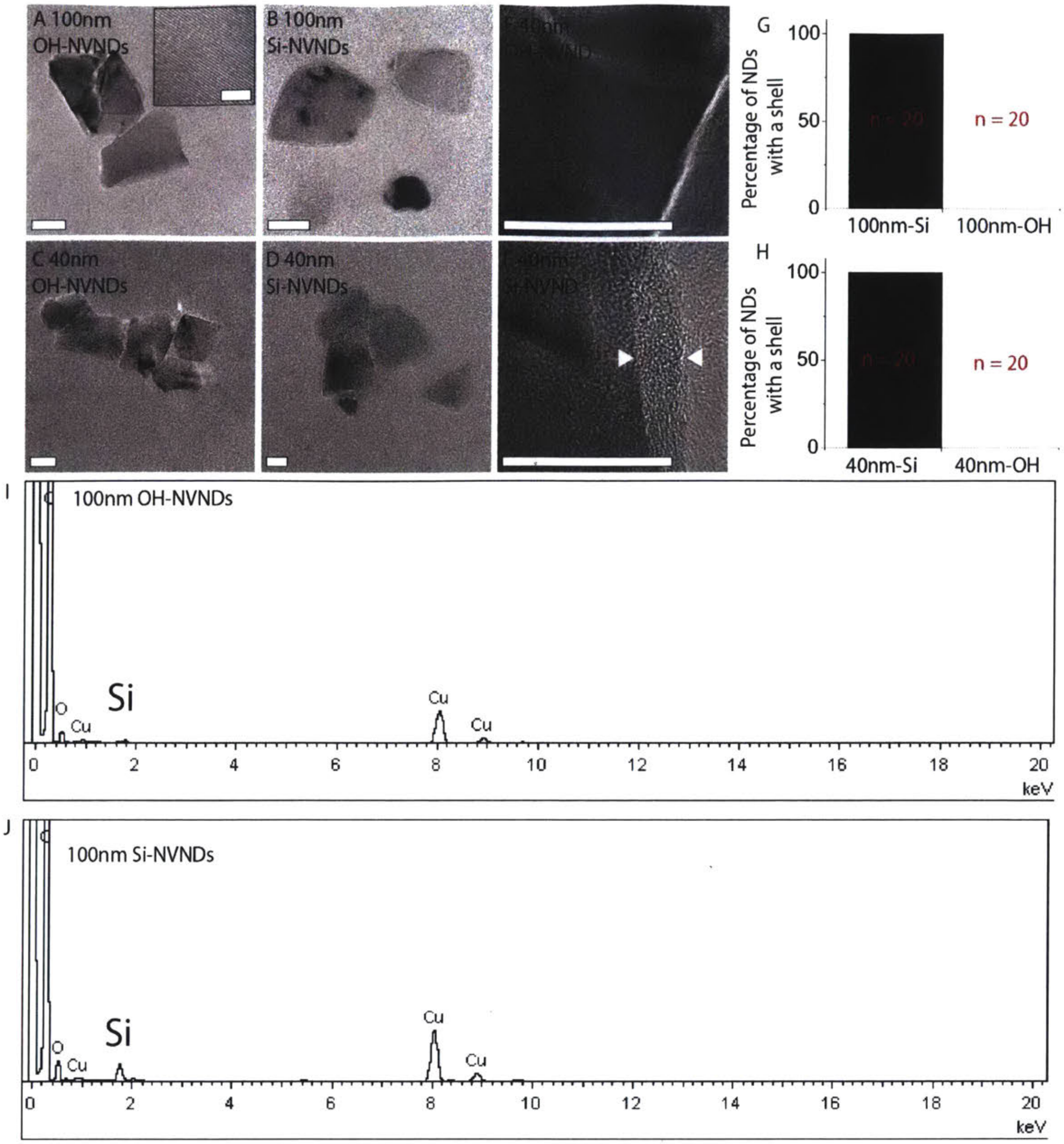

Figure 2. High resolution transmission electron microscopy (HR-TEM) and EDX spectra show effective silanization of NVNDs. (A-F) 100nm and 40nm NVNDs were drop-cast onto a copper grid and imaged using TEM. (A) 100nm OH-NVNDs, inset show crystalline structure. (B) 100nm Si-NVNDs (C) 40nm OH-NVNDs. (D) 40nm Si-NVNDs. (E) HR-TEM of the nanodiamond edge in a 40 nm OH-NVND. (F) HR-TEM of the nanodiamond edge in a 40 nm Si-NVND. The NVND exhibits a shell approximately 5 nm thick (arrowheads). (G) Bar graph showing the percentage of nanodiamonds exhibiting a shell for 100nm Si-NVNDs vs. 100nm OH-NVNDs. (H) Bar graph showing the percentage of nanodiamonds exhibiting a shell for 40nm Si-NVNDs vs. 40nm OH-NVNDs. (I) An EDX spectrum obtained from 100nm OH-NVNDs. (J) An EDX spectrum obtained from 100nm Si-NVNDs. Scale bars: 2nm in inset in A; 50nm in A, B; 20nm in C, D, E, F.

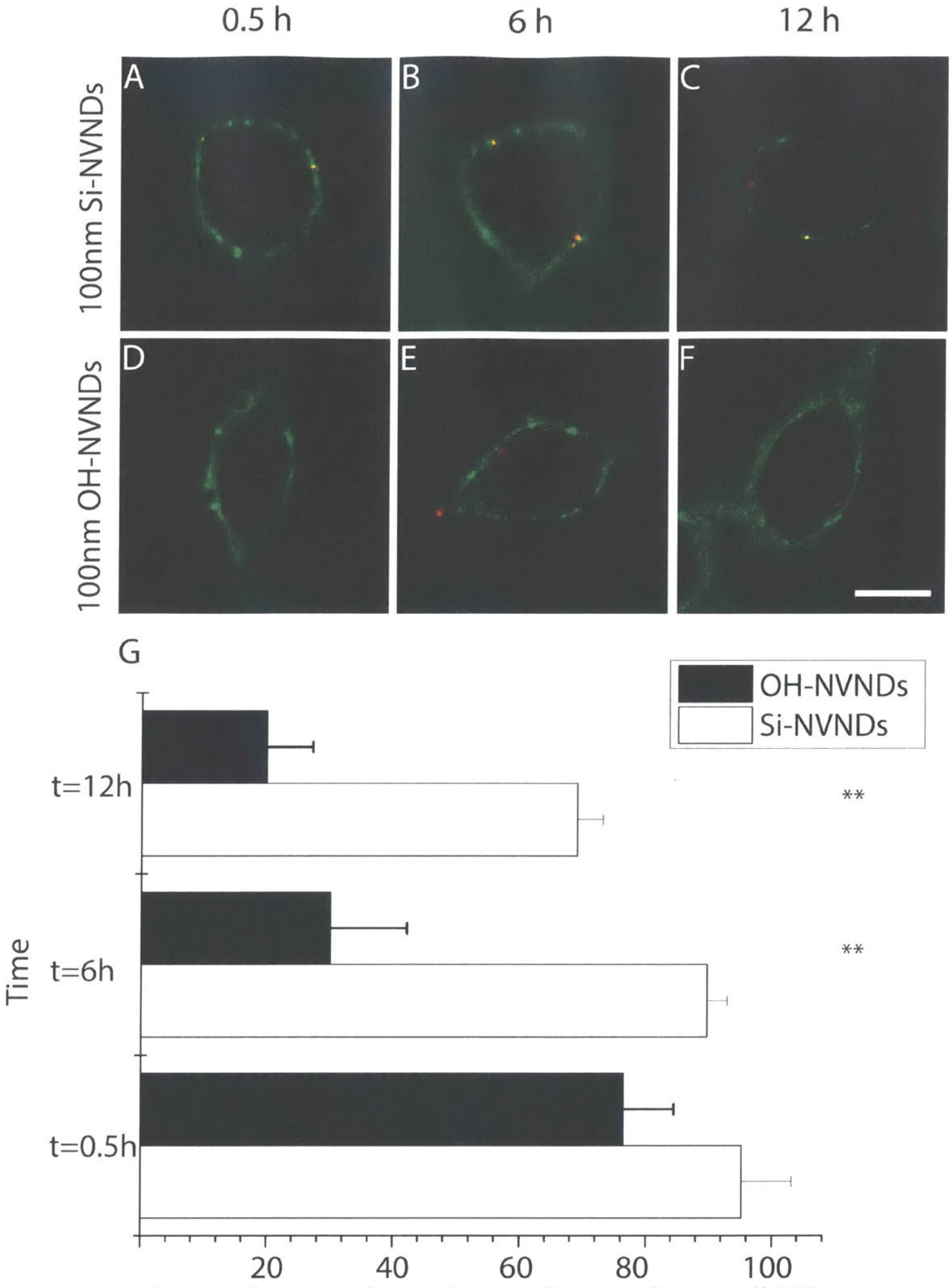

Figure 3. Si-NVNDs are retained on neural membranes for at least 6-12 hours. Cultured neurons were labeled with micellated 100nm Si-NVNDs (A-C, red) or with 100nm OH-NVNDs (D-F, red) and imaged using a confocal microscope. Neural membranes were labeled at 0.5 h (A, D), 6 h (B, E) and 12 h (C, F) of incubation using WGA-488 (green), then imaged. (G) Bar graph showing the

percentage of Si-NVNDs (white bars) vs. OH-NVNDs (black bars) found on neural membranes (n = 64, 45, and 13 OH-NVNDs from 6, 9, and 6 neurons from 2 cultures for 0.5 h, 6 h, and 12 h respectively; n = 84, 57, and 21 Si-NVNDs from 5, 5, and 6 neurons from 2 cultures for 0.5 h, 6 h, and 12 h respectively). Data are mean + standard error of the mean (s.e.m.). Scalebar = 10μm. For the 6h and 12h time points, the percentage of NDs which colocalized with the membrane significantly differed between Si-NVNDs and OH-NVNDs (** $p < 0.01$, Bonferroni corrected T-test; $p = 0.393584$, 0.0072 and 0.00517 for 0.5 h, 6 h and 12 h respectively).

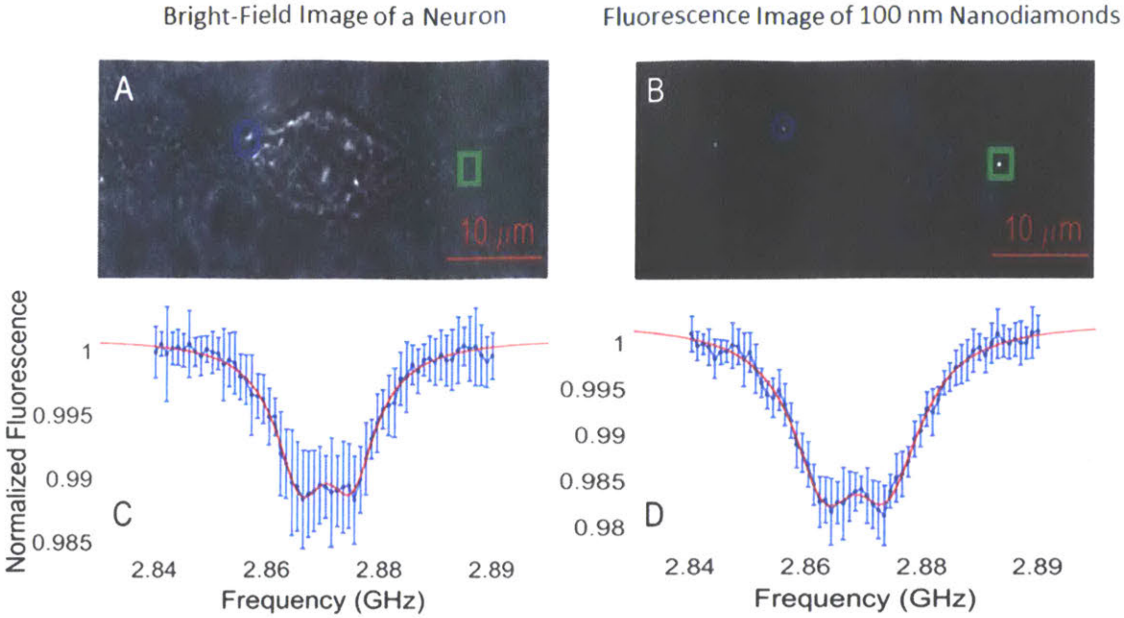

Figure 4. Electron spin resonance of putative single 100nm Si-NVNDs on neurons. (A) Brightfield image of a hippocampal neuron labeled with 100nm Si-NVNDs. (B) NDs on the neuron of A. Two representative Si-NVNDs were selected, depicted in a blue circle and a green box. (C-D) Optically detected magnetic resonance (ODMR) spectra for the NDs within the blue circle (left) and green box (right), respectively. Collected fluorescence from the NV was normalized to a non-resonant frequency (1 GHz). This experiment was repeated 5 times and averaged together to generate the data shown in (C-D).The red line is a curve fit of the ODMR spectrum to determine the NV's resonant frequencies[33]. The blue bars represent the standard error for this measurement.

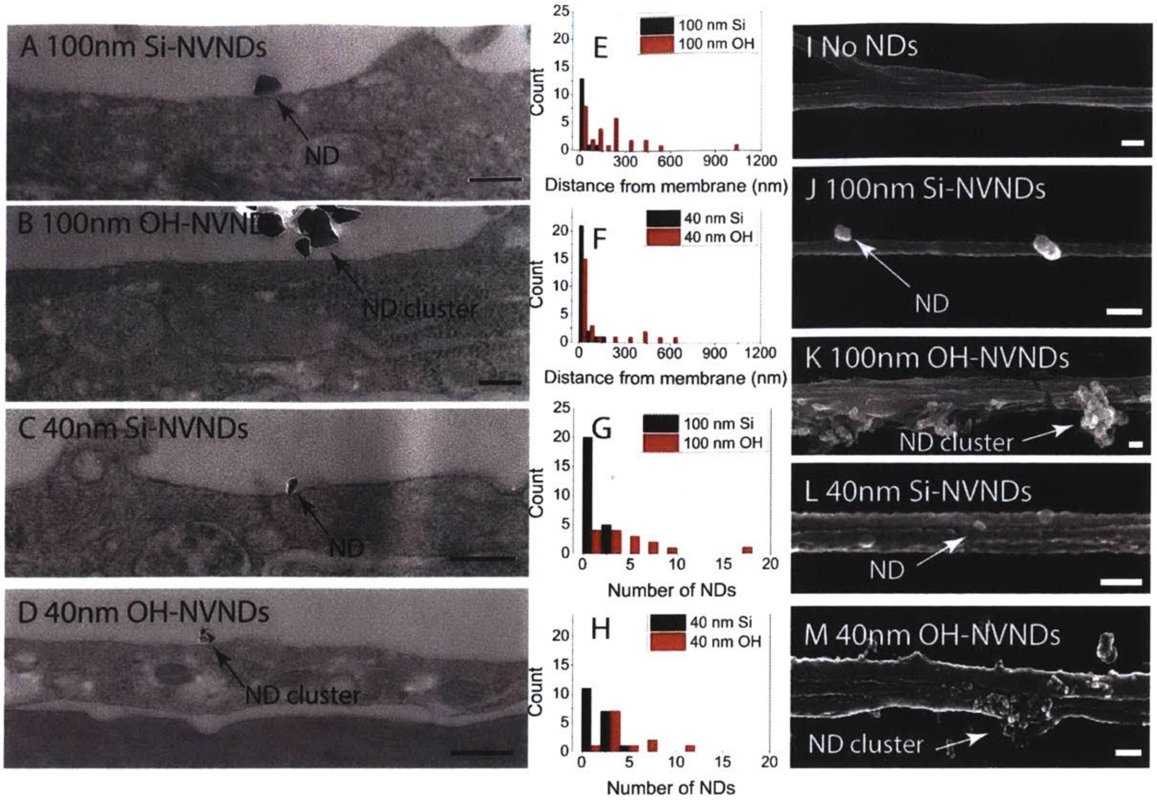

Figure 5. TEM and SEM imaging of NV-NDs on neurons. Cultured neurons were labeled with NVNDs and fixed immediately thereafter. Longitudinal sections were sliced and imaged using TEM (A-D). (A) A neuron labeled with 100nm Si-NVNDs. (B) A neuron labeled with 100nm OH-NVNDs. (C) A neuron labeled with 40nm Si-NVNDs. (D) A neuron labeled with 40nm OH-NVNDs. (E) Histogram showing the distance from the membrane for 100 nm Si-NVNDs (black) and 100 nm OH-NVNDs (red), based on TEM data (n=15 Si-NVNDs from 4 neurons from 2 cultures; n=28 OH-NVNDs from 3 neurons from 3 cultures). (F) Histogram showing the distance from the membrane for 40 nm Si-NVNDs (black) and 40 nm OH-NVNDs (red), based on TEM data (n=27 Si-NVNDs from 3 neurons from 2 cultures; n=20 OH-NVNDs from 3 neurons from 2 cultures). (G) Histogram showing the number of NDs in a cluster for 100 nm Si-NVNDs (black) or 100 nm OH-NVNDs (red), based on TEM data (n=32 Si-NVNDs in 25 clusters from 4 neurons from 2 cultures; n=120 OH-NVNDs in 16 clusters from 3 neurons from 3 cultures). (H) Histogram showing the number of NDs in a cluster for 100 nm Si-NVNDs (black) or 100 nm OH-NVNDs (red), based on TEM data (n=33 Si-NVNDs in 20 clusters from 3 neurons from 2 cultures; n=44 OH-NVNDs in 12 clusters from 3 neurons from 2 cultures). Data for Si-NVNDs and OH-NVNDs were compared in E, F, G and H via a Wilcoxon rank sum test; P = 2.7048e-05, 9.1622e-04, 9.3494e-05 and 0.004 for E, F, G and H respectively. In a different set of experiments, neurons were imaged using a scanning electron microscope (I-M). (I) An unlabeled neuron. (J) A neuron labeled with 100nm Si-NVNDs. (K) An neuron labeled with 100nm OH-NVNDs. (L) An neuron labeled with 40nm Si-NVNDS. (M) A neuron labeled with 40nm OH-NVNDs. Scale bars: 200nm in all micrographs.

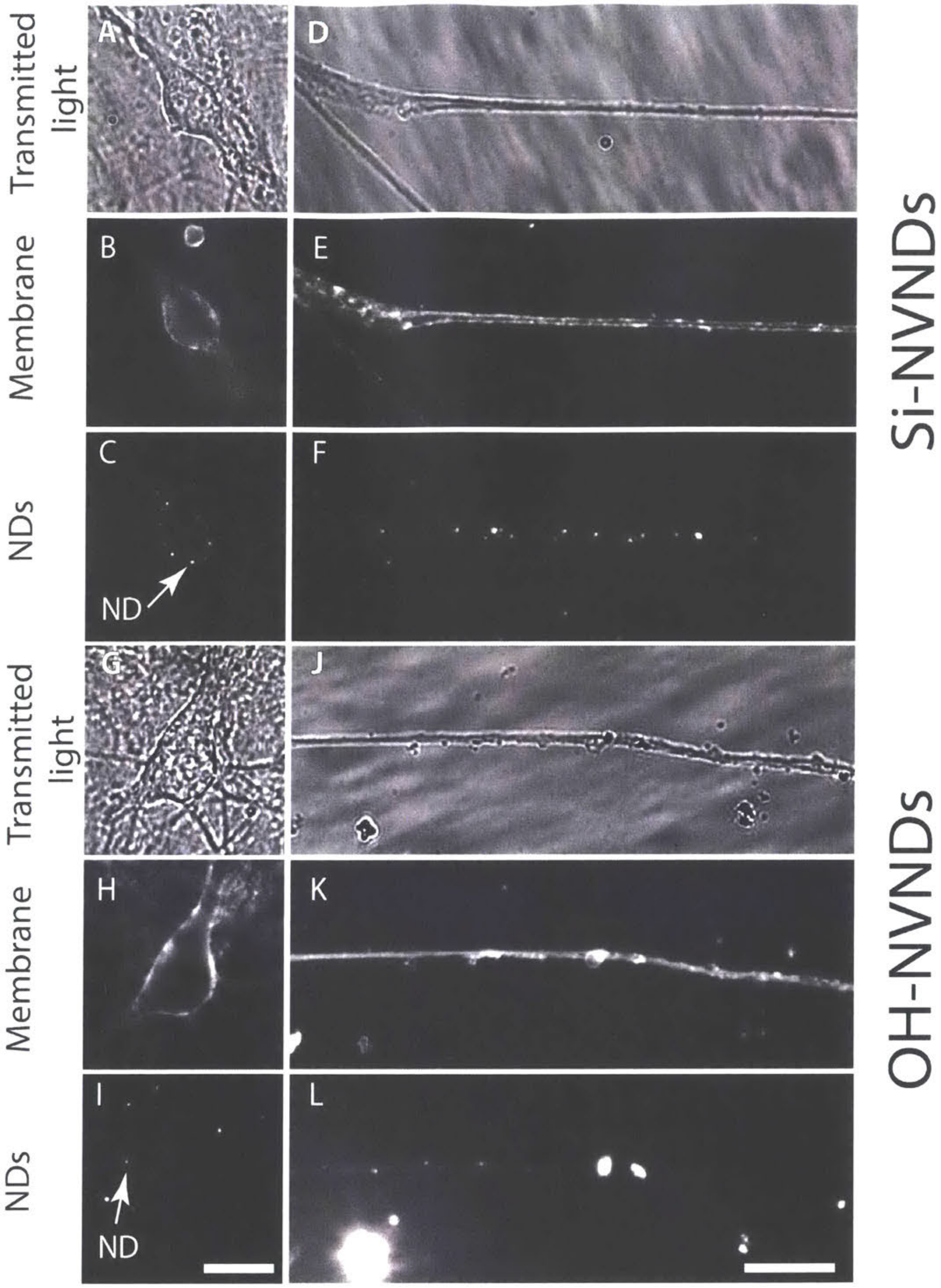

Figure 6. One-photon microscopy of NVND labeled cultured neurons. (A-F) Cultured neurons labeled with micellated 100nm Si-NVNDs and imaged after 0.5h. (A) Brightfield image of the cell body of a neuron. (B) Fluorescence image of the same neuron depicting cell membrane labeling with WGA-488. (C) Fluorescence image of the same neuron depicting cell membrane labeling with Si-NVNDs (D) Brightfield image of neurite (E) Fluorescence image of the neurite depicting membrane labeling the WGA-488 (F) Fluorescence image of the neurite depicting membrane labeling the Si-NVNDs (G-L) As in A-F, but for a neuron labeled with OH-NVNDs. Scale bars: 20µm.

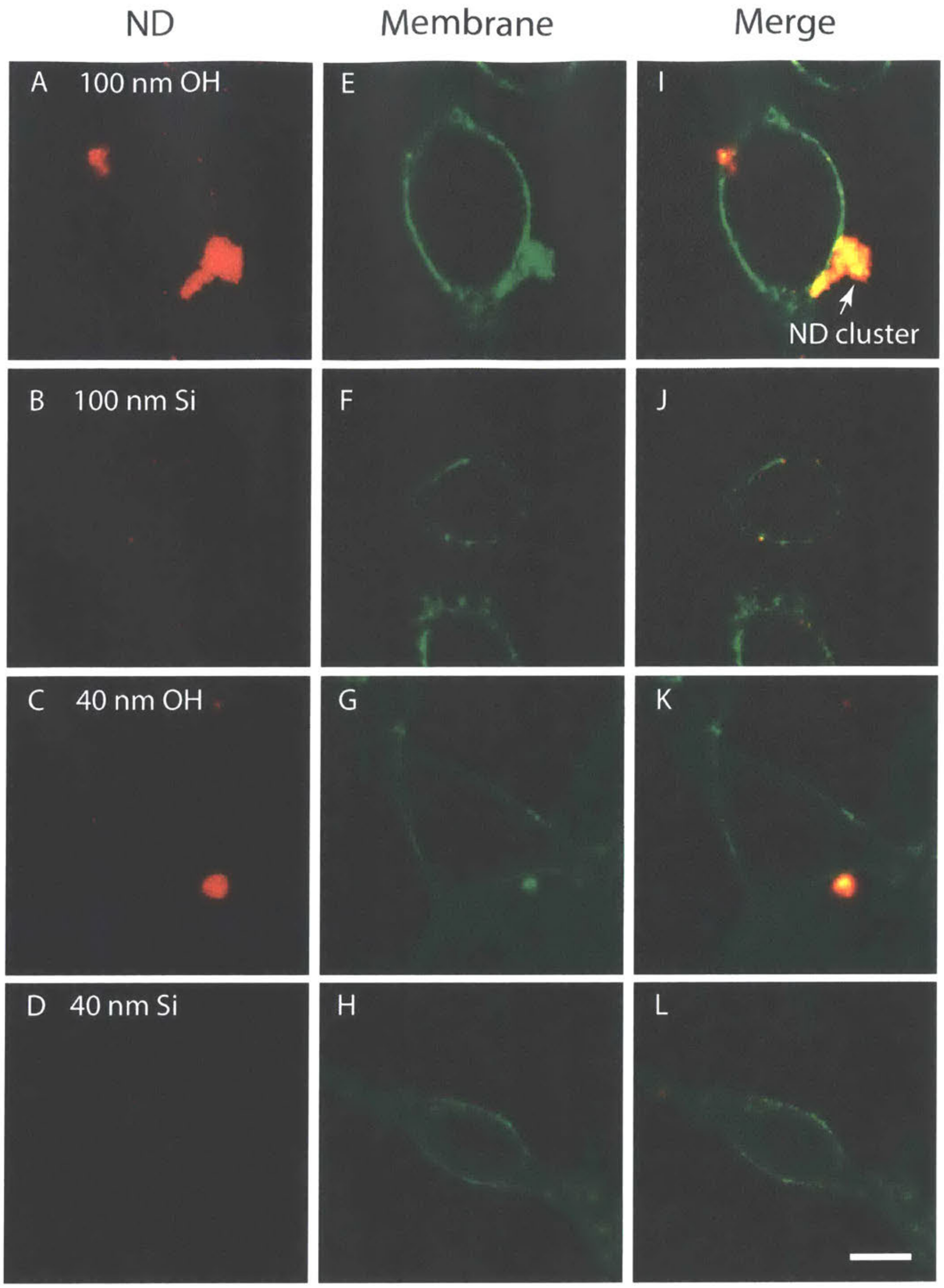

Figure 7. 2-photon imaging of NVND labeled cultured neurons. (A) A cell body of a cultured neuron labeled with 100nm OH-NVNDs and imaged after 0.5h . (B) A cell body of a cultured hippocampal neuron labeled with 100nm Si-NVNDs. (C) A cell body of a cultured hippocampal neuron labeled with 40nm Si-NVNDs. (D) A cell body of a cultured hippocampal neuron labeled with 40nm NVND. (E) The cell body from A imaged in the WGA-488 channel. (F) The cell body from B imaged in the WGA-488 channel. (G) The cell body from C imaged in the WGA-488 channel. (H) The cell body from D imaged in the WGA-488 channel. (I-L) Merged images, of A-D and E-H.

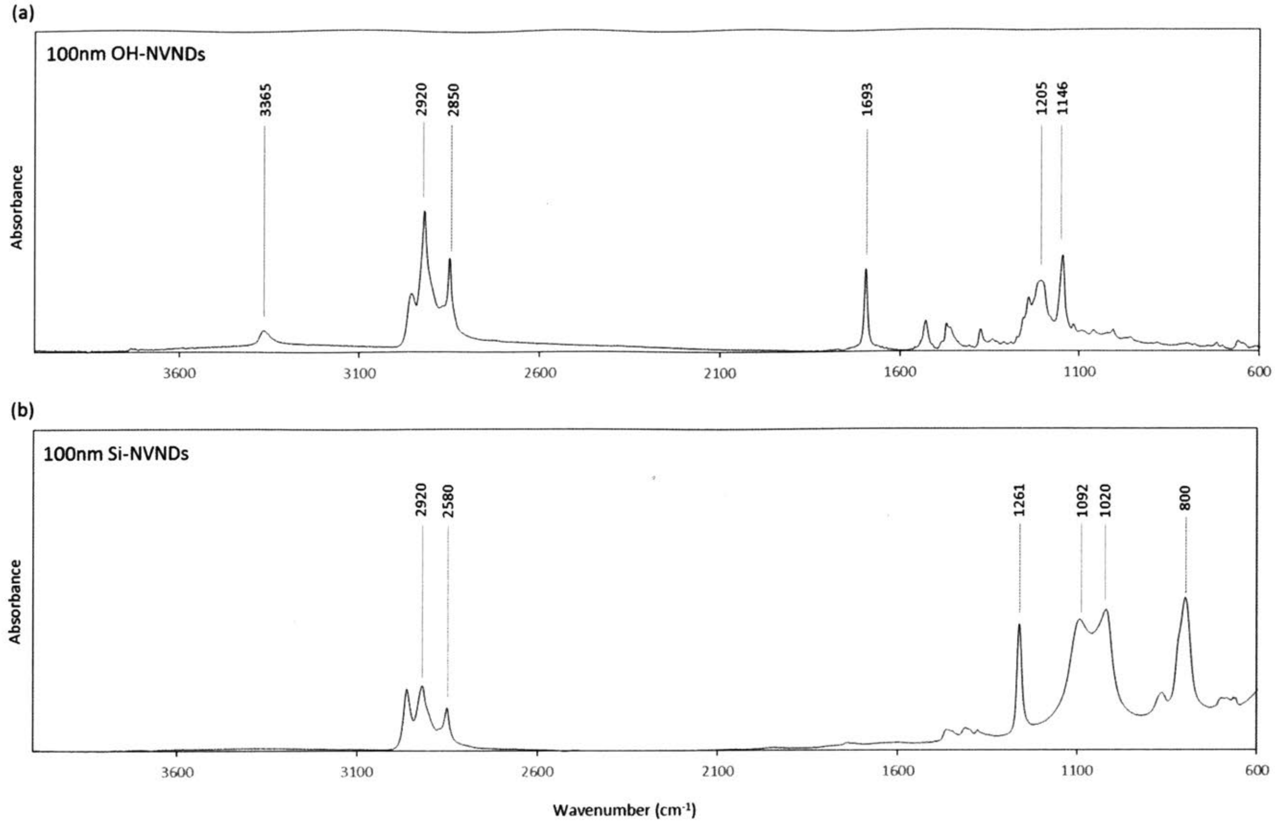

Figure S1. FTIR Spectroscopy of 100nm OH-NVNDs and Si-NVNDs. (A) FTIR spectrum for a KBr window containing 100nm OH-NVNDs. Peak identification: 3365 cm-1 O-H / hydroxyl; 1693 cm-1 C=O / carbonyl; 1693 cm-1 C-O / ether and alcohol; 2920, 2850 cm-1 C-H / alkane, alkene; 1205 cm-1 strained ring C=O. (B) FTIR spectrum for a KBr window containing 100nm Si-NVNDs. Peak identification: 2920, 2850 cm-1 C-H / alkane, alkene; 800 cm-1 Si-C; 1092,1020 cm-1 Si-O-Si; 1261 cm-1 CH3 bending.

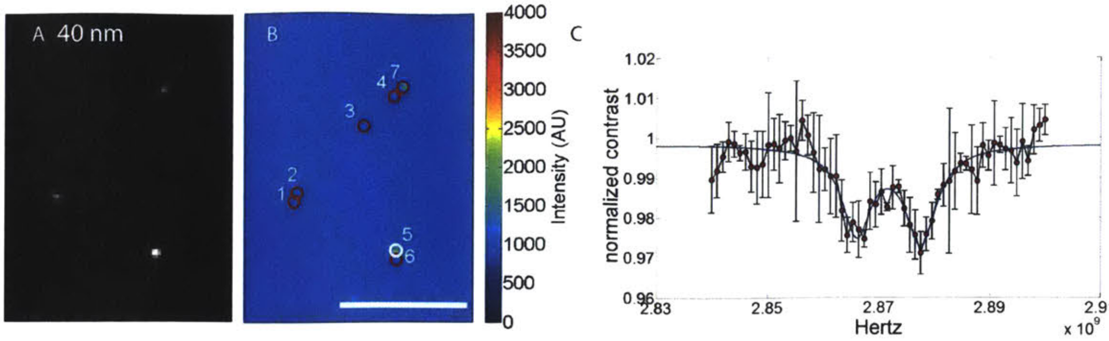

Figure S2. Electron spin resonance analysis of individual 40nm Si-NVNDs on neurons. (A) Fluorescent ND image. (B) Color coded intensity map of nanodiamonds; bright spots which presented ESR behavior are circled in red. (C) Optically detected ESR spectrum for the ND circled in white in (B). Red dots represent the fluorescence measured at a given frequency averaged 5 times. The blue curve is the curve fit of the data, with the error bars representing the standard error of this experiment. Scale bar: 10µm.

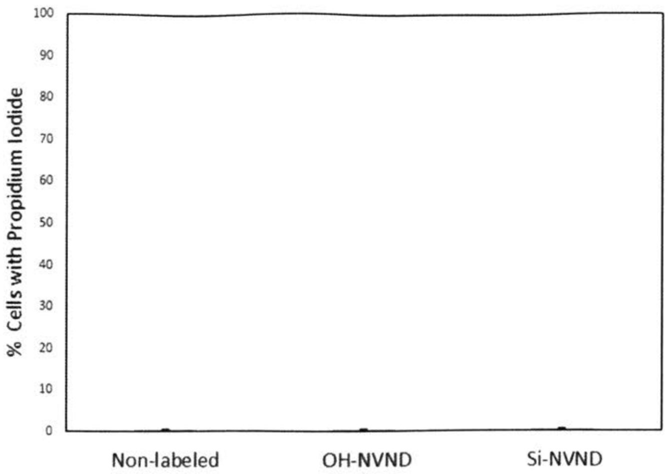

Figure S3. Propidium iodide staining of neurons labelled with 100nm Si-NVNDs and OH-NVNDs. Bar graph representing the percentage of neurons that took up propidium iodide (n=approximately 28,000 neurons from 3 regions of interest from 2 cultures for non-labeled neurons; n=approximately 18,000 neurons from 3 regions of interest from 2 cultures for OH-NVND-labeled neurons; n= approximately 18,000 neurons from 3 regions of interest from 2 cultures for Si-NVND-labeled neurons). No significant difference was found between groups; p= 0.676, one-way-ANOVA, see Supplementary Table 1 for exact *p* values and n values.

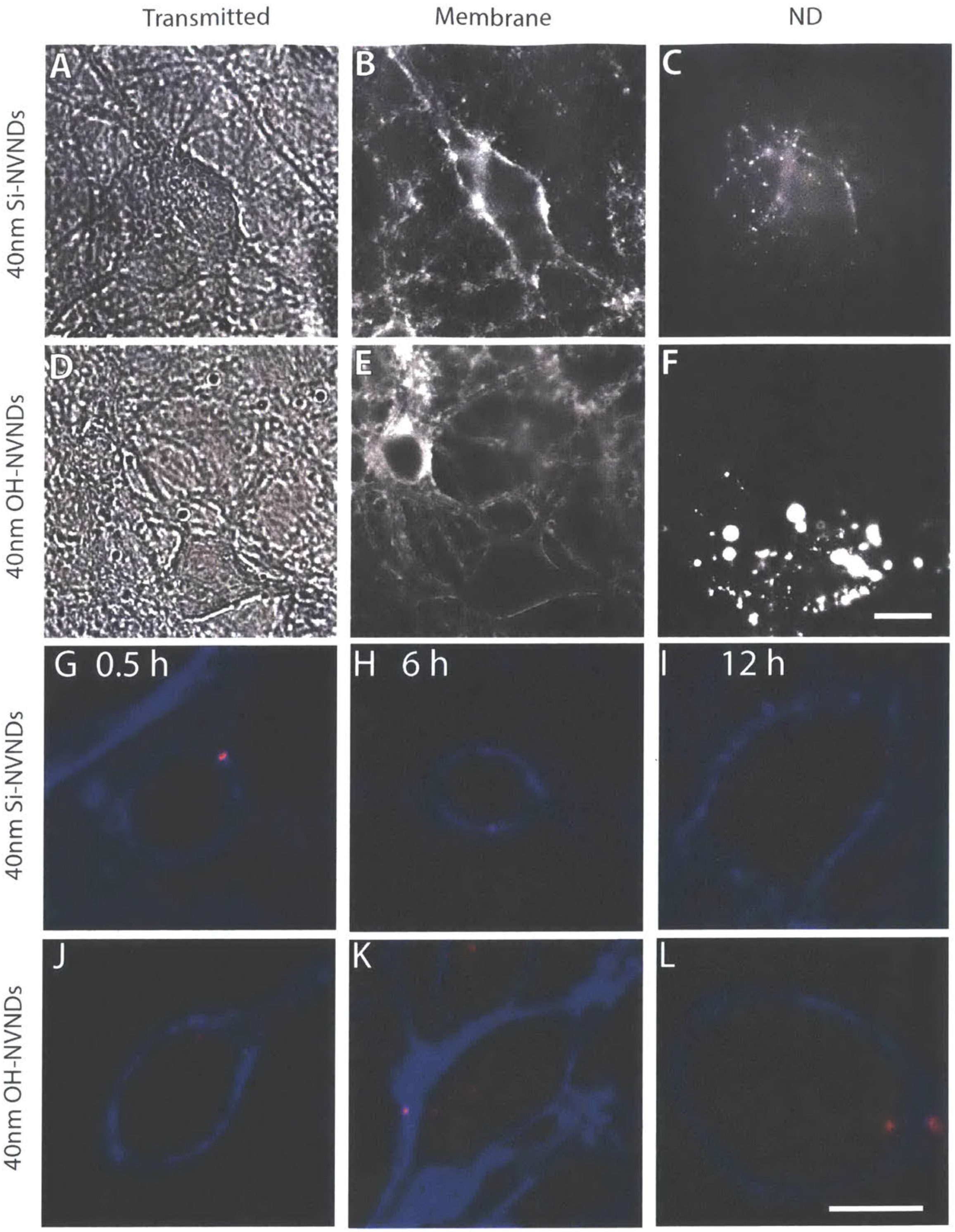

Figure S4. labeling of cultured neurons with 40 nm NVNVDs. Hippocampal neurons were labeled with 40nm Si-NDs (A-C) or 40nm OH-NDs (D-F) and imaged using a widefield scope 0.5h following incubation. Neurons were first found using transmitted light (A, D). Membranes were also labeled with WGA-488 (B, E). Imaging of NV-NDs (C, F) using 532nm laser excitation demonstrated that 40nm OH-NVNDs reside as aggregates on or outside neural membranes, while hydrophobic Si-

NVNDs reveal the contour of cells and have low size variation. (G-L) Cultured Neurons were labeled with NVNDs (red) for increasing periods of time, then labeled with the membrane dye WGA-405 (blue) and imaged with a confocal (shown are single slices of optical thickness 1μm). (G-I) Si-NVND nanodiamond labeling for 0.5 h, 6 h and 12h respectively. (J-H) OH-NVND labeling for 0.5 h, 6 h and 12h respectively. Scale bars: 10μm.

Supporting table 1: statistical test for Fig. S3

SUMMARY				
Groups	*Count*	*Sum*	*Average*	*Variance*
Non labeled	3	1.541847255	0.513949	0.009227
OH-NVND	3	1.393146389	0.464382	0.01745
Si-NVND	3	1.194291407	0.398097	0.046201

ANOVA						
Source of Variation	*SS*	*df*	*MS*	*F*	*P-value*	*F crit*
Between Groups	0.0202723	2	0.010136	0.417	0.676	5.143
Within Groups	0.1457571	6	0.024293			

References

1. Grinolds, M. S. et al. Nanoscale magnetic imaging of a single electron spin under ambient conditions. *Nat. Phys.* **9**, 215–219 (2013).
2. DeVience, S. J. et al. Nanoscale NMR spectroscopy and imaging of multiple nuclear species. *Nat. Nanotechnol.* **10**, 129–134 (2015).
3. Dolde, F. et al. Electric-field sensing using single diamond spins. *Nat. Phys.* **7**, 459–463 (2011).
4. Kucsko, G. et al. Nanometre-scale thermometry in a living cell. *Nature* **500**, 54–58 (2013).
5. Trusheim, M. E. & Englund, D. Wide-field strain imaging with preferentially aligned nitrogen-vacancy centers in polycrystalline diamond. *New J. Phys.* **18**, 123023 (2016).
6. Doherty, M. W. et al. Electronic properties and metrology applications of the diamond NV-center under pressure. *Phys. Rev. Lett.* **112**, 047601 (2014).
7. Pelliccione, M., Myers, B. A., Pascal, L. M. A., Das, A. & Bleszynski Jayich, A. C. Two-Dimensional Nanoscale Imaging of Gadolinium Spins via Scanning Probe Relaxometry with a Single Spin in Diamond. *Physical Review Applied* **2**, (2014).
8. Mochalin, V. N., Shenderova, O., Ho, D. & Gogotsi, Y. The properties and applications of nanodiamonds. *Nat. Nanotechnol.* **7**, 11–23 (2012).
9. Tetienne, J.-P. et al. The nature of domain walls in ultrathin ferromagnets revealed by scanning nanomagnetometry. *Nat. Commun.* **6**, 6733 (2015).
10. Degen, C. Nanoscale magnetometry: Microscopy with single spins. *Nat. Nanotechnol.* **3**, 643–644 (2008).
11. Maurer, P. C. et al. Far-field optical imaging and manipulation of individual spins with nanoscale resolution. *Nat. Phys.* **6**, 912–918 (2010).
12. Chen, E. H., Gaathon, O., Trusheim, M. E. & Englund, D. Wide-field multispectral super-resolution imaging using spin-dependent fluorescence in nanodiamonds. *Nano Lett.* **13**, 2073–2077 (2013).
13. McGuinness, L. P. et al. Quantum measurement and orientation tracking of fluorescent nanodiamonds inside living cells. *Nat. Nanotechnol.* **6**, 358–363 (2011).
14. Hui, Y. Y. et al. Two-photon fluorescence correlation spectroscopy of lipid-encapsulated fluorescent nanodiamonds in living cells. *Opt. Express* **18**, 5896–5905 (2010).
15. Karaveli, S. et al. Modulation of nitrogen vacancy charge state and fluorescence in nanodiamonds using electrochemical potential. *Proc. Natl. Acad. Sci. U. S. A.* **113**, 3938–3943 (2016).
16. Hui, Y. Y. et al. Wide-field imaging and flow cytometric analysis of cancer cells in blood by fluorescent nanodiamond labeling and time gating. *Sci. Rep.* **4**, 5574 (2014).
17. Neugart, F. et al. Dynamics of diamond nanoparticles in solution and cells. *Nano Lett.* **7**, 3588–3591 (2007).
18. Huang, Y.-A. et al. The effect of fluorescent nanodiamonds on neuronal survival and morphogenesis. *Sci. Rep.* **4**, 6919 (2014).
19. Wolcott, A. et al. Surface Structure of Aerobically Oxidized Diamond Nanocrystals. J. Phys. Chem. C *Nanomater. Interfaces* **118**, 26695–26702 (2014).
20. Krüger, A., Liang, Y., Jarre, G. & Stegk, J. Surface functionalisation of detonation diamond suitable for biological applications. *J. Mater. Chem.* **16**, 2322–2328 (2006).
21. Krueger, A., Stegk, J., Liang, Y., Lu, L. & Jarre, G. Biotinylated nanodiamond: simple and

efficient functionalization of detonation diamond. *Langmuir* **24**, 4200–4204 (2008).

22. Dubertret, B. In Vivo Imaging of Quantum Dots Encapsulated in Phospholipid Micelles. *Science* **298**, 1759–1762 (2002).
23. Wang, J., Wang, Y. & Liang, W. Delivery of drugs to cell membranes by encapsulation in PEG–PE micelles. *J. Control. Release* **160**, 637–651 (2012).
24. Wang, T. et al. Paclitaxel-loaded PEG-PE-based micellar nanopreparations targeted with tumor-specific landscape phage fusion protein enhance apoptosis and efficiently reduce tumors. *Mol. Cancer Ther.* **13**, 2864–2875 (2014).
25. Maysinger, D., Lovrić, J., Eisenberg, A. & Savić, R. Fate of micelles and quantum dots in cells. *Eur. J. Pharm. Biopharm.* **65**, 270–281 (2007).
26. Santhosh, P. B. et al. Influence of nanoparticle–membrane electrostatic interactions on membrane fluidity and bending elasticity. *Chem. Phys. Lipids* **178**, 52–62 (2014/2).
27. Park, S.-H., Oh, S.-G., Mun, J.-Y. & Han, S.-S. Effects of silver nanoparticles on the fluidity of bilayer in phospholipid liposome. *Colloids Surf. B Biointerfaces* **44**, 117–122 (2005).
28. Park, S.-H., Oh, S.-G., Mun, J.-Y. & Han, S.-S. Loading of gold nanoparticles inside the DPPC bilayers of liposome and their effects on membrane fluidities. *Colloids Surf. B Biointerfaces* **48**, 112–118 (2006).
29. Chaudhary, N. et al. Endocytic crosstalk: cavins, caveolins, and caveolae regulate clathrin-independent endocytosis. *PLoS Biol.* **12**, e1001832 (2014).
30. Elguindi, I., Redziniak, G., Metezeau, P., Meybeck, A. & Goldberg, M. E. Modulation of membrane receptor endocytosis by chemical effectors of membrane fluidity. *Biol. Cell* **54**, 199–205 (1985).
31. Fröhlich, E. The role of surface charge in cellular uptake and cytotoxicity of medical nanoparticles. *Int. J. Nanomedicine* **7**, 5577–5591 (2012).
32. Wee, T.-L. et al. Two-photon excited fluorescence of nitrogen-vacancy centers in proton-irradiated type Ib diamond. *J. Phys. Chem. A* **111**, 9379–9386 (2007).
33. Horowitz, V. R., Alemán, B. J., Christle, D. J., Cleland, A. N. & Awschalom, D. D. Electron spin resonance of nitrogen-vacancy centers in optically trapped nanodiamonds. *Proc. Natl. Acad. Sci. U. S. A.* **109**, 13493–13497 (2012).
34. Klapoetke, N. C. et al. Independent optical excitation of distinct neural populations. *Nat. Methods* **11**, 338–346 (2014).

APPENDIX

Estimation of the number of nanodiamonds needed to detect a neuron's action potential

We would like to determine the minimum number of NVs we would need to detect the action potential of a firing neuron. There are two approaches. First, using the electric-field dependence of the NV's spin ground state, it has been shown that an electric field change of ~200V/cm*Hz$^{-½}$ can be measured [1]. This sensitivity corresponds to ~6000 V/cm for a time interval of 1 ms. Assuming best-case conditions -- i.e., that the NV is in a nanometer-scale nanodiamond right in the electric field-maximum at the center of the cell's lipid bilayer (assumed to be 4 nm thick) -- the minimum detectable voltage would correspond to 2.4 mV. This is enough to detect the ~100 mV voltage change of the cell membrane. However, this approach has the technical challenge that the smallest nanodiamonds for which ODMR has been reported have a diameter of ~5 nm and poor spin properties. Thus, slightly smaller nanodiamonds with T_2 spin coherence of hundreds of μs would be required to reach the needed sensitivity. Work in this direction is in progress towards improvement in nanodiamond sensitivity [2,3].

A second approach for NV-based voltage sensing relies on the NV's charge duality: the NV's emission spectrum changes dramatically with changes of its internal change state from the negative charge state NV- to the neutral state NV0. Proof-of-concept experiments using NDs resting on an electrochemical interface have indicated that for a single NV center, a ~100 mV voltage swing can be detected for an averaging time of 100 ms, corresponding to ~1 V/ms[15]. This approach would therefore require ~100 NVs to resolve a 100 mV swing in 1 ms. This number of NVs may be accommodated in ~50 nanodiamonds of ~10 nm diameter, assuming 3 ppm NVs in diamond, or one large ND of ~40 nm radius. These are approximate numbers, and more work is needed to explore the relationship between ND size and voltage sensitivity on the cell membranes. We note that silicon vacancy centers, which also have SiV- and SiV0 charge states, have been reported in NDs as small as 1.6 nm [4].

References:

1. Dolde, F. *et al.* Electric-Field Sensing Using Single Diamond Spins. *Nat. Phys.* 7, 459–463 (2011).
2. Knowles, H. S., Kara, D. M., & Atatüre, M. Observing Bulk Diamond Spin Coherence in High-Purity Nanodiamonds. *Nat. Mater.* **13**, 21–25 (2014).
3. Trusheim, M. E. et al. Scalable Fabrication of High Purity Diamond Nanocrystals with Long-Spin-Coherence Nitrogen Vacancy Centers. *Nano Lett.* 14, 32–36 (2014).
4. Vlasov, I. I. *et al.* Molecular-Sized Fluorescent Nanodiamonds. *Nat. Nanotechnol.* **9**, 54–58 (2014).